

INSTABILITIES OF GRAVITY-CAPILLARY WATER WAVES

By

MARC PERLIN

A DISSERTATION PRESENTED TO THE GRADUATE SCHOOL
OF THE UNIVERSITY OF FLORIDA IN PARTIAL FULFILLMENT
OF THE REQUIREMENTS FOR THE DEGREE OF
DOCTOR OF PHILOSOPHY

UNIVERSITY OF FLORIDA

1989

ACKNOWLEDGMENTS

I must express my gratitude to Dr. J. L. Hammack for providing a truly state-of-the-art facility, a tremendous working environment and encouragement when need be. To the person who introduced me to the study of water waves and coastal/ocean engineering, Dr. R. G. Dean, I am eternally indebted. I thank my friend, colleague, and committee member, Dr. J. T. Kirby for his support, both analytically and in general. Dr. H. Segur provided much needed insight to the dynamics of water waves, both through Dr. Hammack and directly. And to Dr. U. H. Kurzweg, who served as a member of my committee and is responsible for helping me bring my mathematics up-to-par, I am thankful. I would also like to thank my long-time associates and former fellow students, Dr. W. R. Dally and Dr. D. L. Kriebel, for their friendship.

The above persons are responsible for helping me with the technical part of the dissertation and education, but the people who really suffered are my family. My wife, Terry, not only had to listen to my trials and tribulations, but had to do without me so much of the time. (Of course, some people would probably say that she was better off, but I dare say she doesn't feel that way.) Believe it or not, she often brought dinner to me to save me the trouble of going home during my qualifier studying days. There is no way to properly express my **gratitude** to her. My two children, Ian and Sarah, also suffered, but hardly realized it since they knew little else. And finally, to my parents, I am grateful. I thank them for giving me, in addition to all of the usual parental guidance and love, something so vital in life's survival, a near perfect work ethic.

TABLE OF CONTENTS

	<u>page</u>
ACKNOWLEDGMENTS	ii
LIST OF FIGURES	v
ABSTRACT	x
CHAPTERS	
1. GENERAL INTRODUCTION	1
2. INTRODUCTION TO GRAVITY-CAPILLARY INSTABILITIES: PART 1	3
3. THEORETICAL CONSIDERATIONS FOR PART 1	8
3.1 Review of the NLS Model	10
3.2 The Stationary, NLS Model	18
4. EXPERIMENTAL FACILITIES, PROCEDURES AND IMAGE ANALYSIS FOR PART 1	24
4.1 The Imaging and Computer Systems	28
4.2 Data Analysis Procedures	29
4.3 Lighting and Image Effects	33
5. RESULTS AND DISCUSSION OF PART 1	39
5.1 Evolution of Quasi-steady Wavefields	39
5.2 Experimental Results and Comparison with sNLS Theory	47
5.2.1 The 25 Hz Wavetrain	47
5.2.2 The 17 Hz Wavetrain	55
5.2.3 The 13.6 Hz Wavetrain	61

5.2.4	The 9.8 Hz Wavetrain, Wilton's Ripples	66
5.2.5	The 8 Hz Wavetrain	72
6.	SUMMARY AND CONCLUSIONS OF PART 1	78
7.	INTRODUCTION TO THREE-WAVE RESONANCE: PART 2	80
8.	RESONANT INTERACTION THEORY	83
9.	RIT AND RIPPLES	87
10.	EXPERIMENTAL FACILITIES FOR PART 2	94
11.	REVIEW OF PREVIOUS EXPERIMENTS ON RIPPLE TRIADS	97
11.1	The 25 Hz Wavetrain: Spatial Data	97
11.2	The 25 Hz Wavetrain: Temporal Data	100
11.3	Other Wavetrains with Frequencies Exceeding 19.6 Hz	103
12.	RESONANT TRIAD SELECTION	107
13.	EVOLUTION OF A RIPPLE WAVETRAIN IN THE PRESENCE OF RANDOM WAVES	115
14.	SUMMARY AND CONCLUSIONS OF PART 2	121
15.	GENERAL SUMMARY AND CONCLUSIONS	123
REFERENCES	125
BIOGRAPHICAL SKETCH	129

LIST OF FIGURES

<u>Figure</u>	<u>Description</u>	<u>Page</u>
3.1	The fluid domain and a definition sketch.	9
3.2	Parameter space of the nonlinear Schroedinger equation showing regions of stability (S) and instability (U) of a wavetrain to longitudinal modulations. Curve C_1 corresponds to zeros of λ ; curves C_4 and C_5 correspond to zeros of v ; Curves C_2 and C_3 correspond to singularities of v . The location of parameters (\bullet) for each experiment is also shown. (Hammack, private communication, 1989).	15
3.3	The dispersion relation of (3.30) calculated for a 25 Hz wavetrain with $a=0.04$ cm. The (p,q) coordinate system is shown along with a degenerate, side-band quartet. The dashed line is a circle, centered at $(0,0)$, with a radius equal to the parabolic vertex coordinate.	21
4.1	The experimental facility and coordinate system. An elevation view is shown in (a) and a plan view in (b).	25
4.2	A typical quiescent background image (taken prior to each experiment) with a frame superposed to depict the region used by the two-dimensional transform.	30
4.3	An overhead image of an 8 Hz experiment (GC0806).	30
4.4	Demonstration of the “criss-cross” effect caused by the numerical two-dimensional FFT. These contour maps of wavenumber spectra are for sine waves with: (a) $k=6.325$ and $\Xi=420$, (b) $k=6.325$ and $\Xi=450$, (c) $k=6.325$ and $\Xi=480$, and (d) $k=6.200$ and $\Xi=450$	34
4.5	Average intensity level, κ , versus inclination angle of light from vertical, Δ , for a quiescent water surface (shown by asterisks). Diamonds represent the plane projection light intensity of the light source versus angle.	36

<u>Figure</u>	<u>Description</u>	<u>Page</u>
5.1	Two seconds of a time series from experiment GC2504.	40
5.2	Demonstration of the quasi-steadiness of the 25 Hz wavefield of experiment GC2504. These contour maps of wavenumber spectra represent the wavefield (a) 1/25 sec, (b) 1/5 sec, (c) 1/2 sec, and (d) 1 sec after the contour map shown in figure 5.9.	41
5.3	A time series of a 24 Hz wavetrain from wavemaker startup.	43
5.4	A time-sequence of contour maps of wavenumber spectra for a 24 Hz wavetrain approaching quasi-steadiness: (a) 3 sec, (b) 9 sec, (c) 21 sec, (d) 33 sec, (e) 45 sec, (f) 46 sec, (g) 47 sec, and (h) 57 sec (theoretical (---) prediction of the sNLS eq.) into the experiment.	44
5.5	Overhead images of experiments (a) GC2502, (b) GC2503, and (c) GC2504.	49
5.6	The amplitude-frequency spectra for experiments (a) GC2502, (b) GC2503, and (c) GC2504.	50
5.7	Contour map of the amplitude-wavenumber spectrum (see inset for a perspective view) for the 25 Hz wavetrain of experiment GC2502. Dispersion relation (---) of the sNLS equation; the region of spreading (— — —) and the most unstable sidebands (X) as predicted by the linear stability analysis.	51
5.8	Contour map of the amplitude-wavenumber spectrum (see inset for a perspective view) for the 25 Hz wavetrain of experiment GC2503. Dispersion relation (---) of the sNLS equation; the region of spreading (— — —) and the most unstable sidebands (X) as predicted by the linear stability analysis.	52
5.9	Contour map of the amplitude-wavenumber spectrum (see inset for a perspective view) for the 25 Hz wavetrain of experiment GC2504. Dispersion relation (---) of the sNLS equation; the region of spreading (— — —) and the most unstable sidebands (X) as predicted by the linear stability analysis.	53

<u>Figure</u>	<u>Description</u>	<u>Page</u>
5.10	The amplitude-frequency spectra for experiments (a) GC1702, (b) GC1704, and (c) GC1706.	56
5.11	Contour map of the amplitude-wavenumber spectrum (see inset for a perspective view) for the 17 Hz wavetrain of experiment GC1702. Dispersion relation (---) of the sNLS equation; the region of spreading (— —) and the most unstable sidebands (X) as predicted by the linear stability analysis.	57
5.12	Contour map of the amplitude-wavenumber spectrum (see inset for a perspective view) for the 17 Hz wavetrain of experiment GC1704. Dispersion relation (---) of the sNLS equation; the region of spreading (— —) and the most unstable sidebands (X) as predicted by the linear stability analysis.	58
5.13	Contour map of the amplitude-wavenumber spectrum (see inset for a perspective view) for the 17 Hz wavetrain of experiment GC1706. Dispersion relation (---) of the sNLS equation; the region of spreading (— —) and the most unstable sidebands (X) as predicted by the linear stability analysis.	59
5.14	The amplitude-frequency spectra for experiments (a) GC13601, (b) GC13605, and (c) GC13606.	62
5.15	Contour map of the amplitude-wavenumber spectrum (see inset for a perspective view) for the 13.6 Hz wavetrain of experiment GC13601. Dispersion relation (---) of the sNLS equation; the region of spreading (— —) and the most unstable sidebands (X) as predicted by the linear stability analysis.	63
5.16	Contour map of the amplitude-wavenumber spectrum (see inset for a perspective view) for the 13.6 Hz wavetrain of experiment GC13605. Dispersion relation (---) of the sNLS equation; the region of spreading (— —) and the most unstable sidebands (X) as predicted by the linear stability analysis.	64

<u>Figure</u>	<u>Description</u>	<u>Page</u>
5.17	Contour map of the amplitude-wavenumber spectrum (see inset for a perspective view) for the 13.6 Hz wavetrain of experiment GC13606. Dispersion relation (---) of the sNLS equation; the region of spreading (— —) and the most unstable sidebands (X) as predicted by the linear stability analysis.	65
5.18	The amplitude-frequency spectra for experiments (a) GC9801, (b) GC9802, (c) GC9804, and (d) GC9810.	67
5.19	Contour map of the amplitude-wavenumber spectrum (see inset for a perspective view) for the 9.8 Hz wavetrain of experiment GC9801.	68
5.20	Contour map of the amplitude-wavenumber spectrum (see inset for a perspective view) for the 9.8 Hz wavetrain of experiment GC9802.	69
5.21	Contour map of the amplitude-wavenumber spectrum (see inset for a perspective view) for the 9.8 Hz wavetrain of experiment GC9804.	70
5.22	Contour map of the amplitude-wavenumber spectrum (see inset for a perspective view) for the 9.8 Hz wavetrain of experiment GC9810.	71
5.23	The amplitude-frequency spectra for experiments (a) GC0802, (b) GC0804, and (c) GC0806.	73
5.24	Contour map of the amplitude-wavenumber spectrum (see inset for a perspective view) for the 8 Hz wavetrain of experiment GC0802.	74
5.25	Contour map of the amplitude-wavenumber spectrum (see inset for a perspective view) for the 8 Hz wavetrain of experiment GC0804.	75
5.26	Contour map of the amplitude-wavenumber spectrum (see inset for a perspective view) for the 8 Hz wavetrain of experiment GC0806. Dispersion relation (---) of the sNLS equation for a 24 Hz wavetrain.	76
9.1	Graphical solution of the kinematic resonance conditions (after Simmons 1969) for collinear triads of a 25 Hz test wave. (Henderson and Hammack, 1987).	89

<u>Figure</u>	<u>Description</u>	<u>Page</u>
9.2	Theoretical interaction coefficients for ripple triads. (a) γ_2 vs. f_2 for a series of test waves. (b) Interaction coefficients and initial growth rate for a 25 Hz test wave— γ_1 ; — γ_2 ; - - γ_3 ; —, 100λ with $\Theta = \pi/2$, $a_1 = 0.02$ mm · (Henderson and Hammack, 1987).	92
11.1	Overhead view showing spatial evolution of a 25 Hz wavetrain with increasing k_5 -values of (a) 0.04, (b) 0.23, (c) 0.29, (d) 0.46, (e) 0.67 and (f) 1.08. (Henderson and Hammack, 1987).	99
11.2	Temporal wave profiles and corresponding periodograms for the 25 Hz wavetrains of figures 11.1 (b), (c), (d) and (e), respectively. (Henderson and Hammack, 1987).	101
11.3	Periodograms for 8 wavetrains. Generation parameters and results are presented in Table 11.1. (Henderson and Hammack, 1987).	104
12.1	Amplitude spectra of computer generated command signals for a 25 Hz sine wave with an amplitude of 1.2 v. (a) DEC MicroPDP-11 (b) DEC VAXstation II.	109
12.2	Amplitude spectral evolution for a 25 Hz wavetrain seeded with a 57 Hz wavetrain with 1/10 of its amplitude at the wavemaker.	113
13.1	Average amplitude spectra at $x = 7$ cm for (a) natural background noise in the wave tank and (b) random waves generated by the wavemaker.	118
13.2	Average amplitude spectra showing the transfer of energy by non-linear interactions between a 25 Hz test wave and random waves (white noise) generated with a S/N = 10.	119

Abstract of Dissertation Presented to the Graduate School
of the University of Florida in Partial Fulfillment of the
Requirements for the Degree of Doctor of Philosophy

INSTABILITIES OF GRAVITY-CAPILLARY WATER WAVES

By

MARC PERLIN

August 1989

Chairman: Joseph L. Hammack, Jr.

Major Department: Aerospace Engineering, Mechanics, and
Engineering Science

In Part 1 of this study, gravity-capillary waves, generated mechanically on clean, deep water in a wide channel, are shown to be spatially unstable due to a degenerate four-wave interaction. This instability occurs for wavetrains with frequencies greater than 9.8 Hz, and manifests itself as quasi-steady in time but spatially disordered. Experimental measurements are made using a high-speed imaging system which allows the wavenumber spectrum of the water surface to be calculated. Wavetrains with small to moderate amplitudes and frequencies greater than 9.8 Hz show directional spreading of energy during propagation. This transfer of energy is found to be modeled accurately by solutions of a stationary, nonlinear Schroedinger (NLS) equation involving two (surface) space coordinates. Experimental wavetrains with cyclic frequencies of 25, 17, 13.6, 9.8 and 8 Hz are investigated. The 9.8 Hz wavetrain (Wilton's ripples) is unstable due to second harmonic resonance; however, it exhibits some directional spreading of energy as well. The 8

Hz wavetrain is stable until a detuned, third harmonic resonance occurs, and then the third harmonic (24 Hz) becomes spatially unstable. Reasonable agreement between quantities predicted by a linear stability analysis (i.e., the region of spreading and the most unstable spatial sidebands) of the stationary, NLS equation and the measured data is shown for all the wavetrains with frequencies greater than 9.8 Hz.

The second part of the study concentrates on experimental waves with frequencies greater than 19.6 Hz where a continuum of resonant three-wave interactions are theoretically admissible. Rather than the entire continuum being excited, temporal data show that a dominant resonant triad(s) evolves due to the presence of exceedingly small background waves at distinct frequencies. If, in addition to a primary wavetrain, a broad-banded frequency spectrum of background waves is generated, the entire continuum of admissible triads is excited in a manner consistent with resonant interaction theory for a single triad.

CHAPTER 1

GENERAL INTRODUCTION

For over a hundred years, water waves have been studied by observation in nature, experiments, mathematical analyses, and, more recently, by numerical techniques. Original interest appears to have been motivated by the study of the tides. More recently, interest has broadened to include the entire spectrum of ocean surface waves which includes many length scales. Waves for which surface tension and gravitation are important driving forces are known as gravity-capillary (G-C) waves or simply ripples. These waves have typical frequencies in the range of 5 through 50 Hertz (Hz) and wavelengths of about 5 through 0.5 cm. In the last few years, remote sensing of the ocean surface to obtain information about larger-scale gravity waves has actually focussed attention on these smaller-scale waves. They seem to play a very important role in the manner in which the high-frequency radar waves are scattered, apparently because of the proximity of their respective wavelengths. Herein, we will investigate two different instabilities of G-C water waves.

Previous research has demonstrated that plane, G-C waves generated in a laboratory are fraught with instabilities which occur rapidly, even for wavetrains of sensible (low to moderate wave steepnesses) amplitudes. These initially one-dimensional surface patterns quickly evolve into two-dimensional surfaces. These instabilities are investigated both experimentally and analytically by two distinct approaches: a degenerate, four-wave interaction and a resonant three-wave interac-

tion. In the first analysis, Part 1, it is shown that the stationary, nonlinear Schroedinger equation governs the spatial disordering of the wavetrain. Thus, a mechanism for the directional spreading of energy is established. This analysis encompasses Chapters 2 through 6.

In Part 2, Chapters 7 through 14, the resonant three-wave (triad) equations are presented and reviewed. Experimental evidence of the selection mechanism for triads is presented. It is shown that one or more resonant triads can be excited by a high frequency seed wave of exceedingly small amplitude. The evolution of a ripple wavetrain in the presence of random waves is also addressed. It is shown that if no seed waves are present, the entire continuum of admissible triads is excited in a manner consistent with resonant interaction theory for a single triad.

Since ripple dynamics are similar in many respects to other nonlinear dynamical systems, this work should be of interest to persons in these related areas. In fact, several of the governing equations derived in the context of G-C waves, such as the three-wave resonance equations and the nonlinear Schroedinger equation, are nearly identical to those in other areas of waves in dispersive media; the differences arise in the coefficients, only. These areas include optics, rigid-body mechanics, hydrodynamic stability, and plasma physics.

The second part of this study is essentially a reprint of a research paper by Hammack, Perlin, and Henderson (to appear, 1989), which was presented by Professor Hammack during a series of lectures at the International School of Physics "Enrico Fermi," Course CIX. This research was conducted prior to installation of the imaging system that is used extensively in the study of Part 1.

CHAPTER 2

INTRODUCTION TO GRAVITY-CAPILLARY INSTABILITIES: PART 1

Waves on the oceans' surface have stimulated the curiosity of observers for many years. Contemporary scientific interests in ocean waves appears to have begun with the study and prediction of tides. Airy (1845) was the first to analyze tides using the equations of motion derived from Newtonian mechanics. Since the seminal work of Airy, water waves have been studied intensely using observations, experiments, mathematical analyses, and, more recently, numerical techniques. Interests have broadened to include the entire spectrum of the oceans' surface waves, especially those generated by wind. When wind blows over a water surface, waves are generated whose primary restoring forces are gravitation for the longer waves and surface tension for the shorter waves. When both restoring forces are important, the waves are termed gravity-capillary (G-C) waves, or simply ripples. These are the waves of interest in this study.

Ripples are omnipresent on the ocean surface. In addition to wind generation, they result from breaking gravity waves, rain, and other disturbances which have length-scales of about 1 cm. Kelvin (1871) first examined infinitesimal G-C waves theoretically, and obtained their "dispersion" relation for deep water (i.e. water depth much greater than 1 cm). This relation between the radian frequency, ω and the wavenumber magnitude, k for a wavetrain of infinitesimal amplitude was given by Kelvin as

$$\omega^2 = gk + Tk^3 \quad (2.1)$$

where g represents the acceleration of gravity and T is the kinematic surface tension. According to (2.1), the cyclic wave frequency, $f = \omega/2\pi$, at which gravity and surface tension effects are equal on a clean surface, $T = 73 \text{ cm}^3/\text{sec}^2$ ($T=73 \text{ dyn/cm}$ per mass density, ρ), is 13.6 Hz. The corresponding wavelength, $2\pi/k$, is about 1.7 cm. Rayleigh (1890) investigated ripples on clean and greasy surfaces both experimentally and analytically, and used (2.1) to determine the surface tension, T from measured values of ω and k . Faraday (1883) studied ripples, or "crispations" as he termed them, by vibrating a glass plate vertically which was covered with a layer of water. This vibration generated standing waves on the water surface whose crests were orthogonal; the excited waves had a period which was twice that of the vibration. In these studies, an implicit assumption was made that the wavetrains are stable.

Unfortunately, small-amplitude G-C wavetrains are unstable, i.e. they do not propagate without significant distortions. The first example of a ripple instability was found by Harrison (1909) and explained by Wilton (1915). Wilton showed that a wavetrain of 9.8 Hz (on clean, deep water) is unstable to its second, or 19.6 Hz, harmonic. In fact, there exists a countable set of these "internal resonances" for G-C waves, where each wave is unstable to one of its higher harmonics. One example of importance herein is an 8.38 Hz wavetrain which is unstable to its third harmonic (25.14 Hz).

In addition to internal resonances, small-amplitude trains of water waves are subject to a variety of instabilities that arise from interactions with small, background perturbations. Perhaps, the best-known instability of this type is that which results from longitudinal perturbations in the amplitudes of plane gravity waves.

The existence of this instability was first recognized by Benjamin and Feir (1967), Whitham (1967), and Lighthill (1965), and is known as the Benjamin-Feir (B-F) instability. A more detailed analysis of the Benjamin-Feir instability was presented by Benney and Newell (1967), Zakharov (1968) and Hasimoto and Ono (1972), who derived the nonlinear Schroedinger (NLS) equation for the evolution of an unstable one-dimensional (plane) wavetrain. This equation plays an especially important role in this study, and has the form (e.g. Ablowitz and Segur, 1979)

$$i A_t + A_{xx} + |A|^2 A = 0. \quad (2.2)$$

In (2.2), A represents a suitably normalized complex-amplitude "envelope" of the wavetrain, t is the time, and $+x$ is the direction of propagation. The NLS equation can be solved exactly, for arbitrary initial data, using the methods of "Inverse Scattering Theory" as long as the envelope decays to zero at infinity. This solution shows that the Benjamin-Feir instability leads to very ordered "soliton" behavior and recurrence.

Typically, plane G-C wavetrains theoretically manifest the Benjamin-Feir instability. Also, G-C waves are subject to other instabilities when the perturbations occur obliquely to the direction of propagation. These instabilities result from three-wave, four-wave, etc., resonances which are described by the fundamental ideas of resonant interactions formulated by Phillips (1960). Resonant triads are the first to occur on clean, deep water when the frequency of a G-C wavetrain is greater than 19.6 Hz. McGoldrick (1965) showed that standing G-C waves may display three-wave resonances (resonant triads). Simmons (1969) presented a more general derivation for propagating waves which included spatial variations. (In fact, Wilton's ripples are a degenerate three-wave resonance.) Experiments on three-wave resonance have been presented by McGoldrick (1970), Bannerjee and

Korpel (1982), and Henderson and Hammack (1987). Ma (1982) investigated the bifurcation from two-dimensional G-C waves into three-dimensional waves. Chen and Saffman (1985) investigated the three-dimensional stability and bifurcation of capillary and gravity waves. Zhang and Melville (1986 and 1987) have numerically studied three-dimensional instabilities of two-dimensional, G-C waves. Aside from the interactions due to the NLS equation, waves with frequencies of less than 19.6 Hz exhibit resonant four-wave interactions; they do not admit resonant triads. While resonant quartets have been studied in considerable detail for gravity waves, there has been very little attention given to four-wave interactions for G-C waves. (In fact, the Benjamin-Feir instability of gravity waves can be viewed as a degenerate four-wave resonance.) Yet, there is clear experimental evidence that these waves are indeed unstable (Henderson and Lee (1986) and Henderson, 1986). When a wavetrain with a frequency less than 19.6 Hz is generated mechanically in a wide channel, a spatially disordered wavefield occurs. Modulations are present in both surface directions; however, frequency spectra show that the energy present is concentrated at the input wave and superharmonic frequencies only.

The objective of the first part of this study is to examine this instability, both experimentally and analytically. Experimental measurements of G-C wavetrains are made using a high-speed imaging system. These spatial data are used to calculate the wavenumber spectrum. Wavetrains are generated with small to moderate amplitudes; all wavetrains with frequencies greater than 9.8 Hz show that the input energy spreads directionally during wave propagation. This transfer of energy is modeled accurately by solutions of a NLS equation similar to (2.2), in which the independent variables (t, x) are replaced by the surface coordinates (x, y). This instability occurs for all wavetrains on clean, deep water with frequencies greater than 9.8 Hz.

An outline of Part 1 of this dissertation is as follows. Chapter 3 presents theoretical considerations including an outline of the derivation of the two space dimensions plus time (2+1) NLS equation, and the most unstable sidebands, spatial growth rates, and the limiting angles of the directional spreading which can occur according to a linear stability analysis. Chapter 4 describes the experimental facilities and procedures, with an emphasis on imaging techniques and the interpretation of wavenumber spectra. Chapter 5 presents the experimental results for wavetrains with frequencies of 25, 17, 13.6, 9.8 and 8 Hz and a comparison with the prediction of the stationary, nonlinear Schroedinger equation. Finally, Chapter 6 summarizes the results and conclusions of this study.

CHAPTER 3

THEORETICAL CONSIDERATIONS FOR PART 1

Consider the fluid domain shown in figure 3.1 which consists of a water layer with uniform, quiescent depth h , that is bounded below by a rigid impermeable boundary and bounded above by a free surface with a tension, T . A Cartesian coordinate system is located such that the x and y axes lie in the quiescent water surface and the z axis is vertically upward, parallel to a downward gravitational force per unit mass, g . Vertical deformations of the water surface from the quiescent position are denoted by $\zeta(x,y,t)$. It is well known (e.g. Lamb, 1932) that the inviscid, irrotational, incompressible motions of this fluid layer can be formulated in terms of a velocity potential, $\phi(x,y,z,t)$ as

$$\nabla^2 \phi = 0, \quad -h < z < \zeta(x,y,t) \quad (3.1)$$

with boundary conditions

$$\phi_z = 0, \quad z = -h \quad (3.2a)$$

$$\zeta_t + \phi_x \zeta_x + \phi_y \zeta_y = \phi_z, \quad z = \zeta \quad (3.2b)$$

$$g\zeta + \phi_t + \frac{1}{2}|\nabla\phi|^2 = T \frac{\zeta_{xx}(1 + \zeta_y^2) + \zeta_{yy}(1 + \zeta_x^2) - 2\zeta_{xy}\zeta_x\zeta_y}{(1 + \zeta_x^2 + \zeta_y^2)^{3/2}}, \quad z = \zeta \quad (3.2c)$$

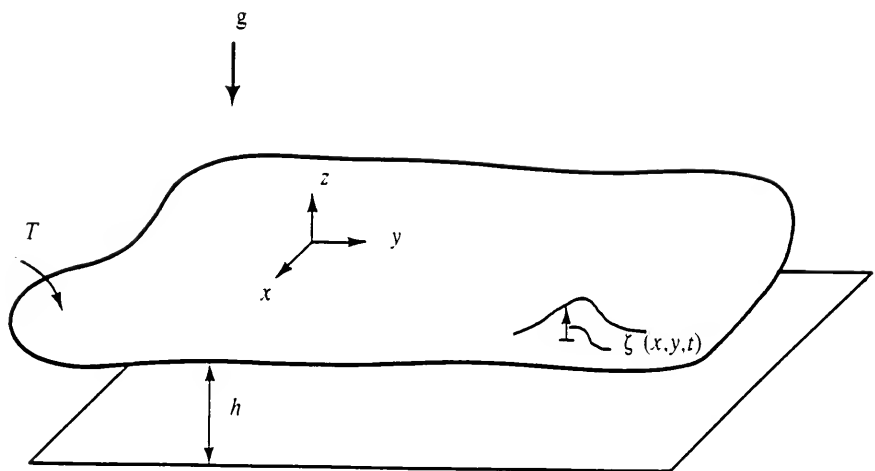


Figure 3.1 The fluid domain and a definition sketch.

Equations (3.1) and (3.2) are analytically intractable. Therefore, approximations are used. Herein, the approximation of interest is an evolution equation for the envelope of a modulated wavetrain on water of finite depth, the nonlinear Schroedinger equation.

3.1 Review of the NLS Model

The characteristic length scales of the water wave problem of (3.1) and (3.2) are the reciprocal wavevector magnitude, k^{-1} , the wave amplitude, a , and the water depth, h . The important dimensionless parameters determined from these scales are the wave steepness, ka , and the relative water depth, kh . Herein, we represent the two-dimensional wave vector by $\mathbf{k} = (l, m)$ and use k_0 to represent the wavenumber of the plane wave input during experiments.

In order to derive the general NLS equation (following Ablowitz and Segur, 1979), it is necessary to make the following assumptions; (1) small amplitude waves ($\epsilon \equiv ka \ll 1$), (2) slowly varying modulations ($\delta l/k \ll 1$), (3) almost one-dimensional waves ($|m|/k \ll 1$), and (4) a balance of these effects. To avoid shallow water, we require $(kh)^2 \gg \epsilon$. If we now expand the dependent variables, ϕ and ζ , of (3.1) and (3.2), in terms of a power series in the small parameter, ϵ , and employ a Taylor series to represent functions in terms of their behavior at the known reference position, $z=0$, we obtain an infinite set of linear equations ordered in powers of ϵ to replace (3.1) and (3.2). The first order, linear, homogeneous problem has the solution

$$\phi = \epsilon \left[A \frac{\cosh k(z+h)}{\cosh kh} \exp(i(kx - \omega t)) + cc \right] \quad (3.3)$$

with the dispersion relation

$$\omega^2 = (gk + Tk^3) \tanh kh. \quad (3.4)$$

(Herein, "cc" denotes the complex conjugate.)

In order to allow slow modulations of the wavetrain at second and higher orders (i.e. a non-uniform wavetrain which is narrow-banded), the method of multiple scales is used to expand independent variables (x, y, t). In addition, ϕ and ζ are expanded such that the amplitude and mean motion (which arises at second order for a uniform wavetrain) are allowed to vary slowly. Slow scales are introduced as follows,

$$x_1 = \epsilon x, \quad y_1 = \epsilon y, \quad t_1 = \epsilon t, \quad t_2 = \epsilon^2 t \quad (3.5)$$

and the expansions of ϕ and ζ are

$$\begin{aligned} \phi &= \epsilon \left(\dot{\Phi}(x_1, y_1, t_1, t_2) + \frac{\cosh k(z+h)}{\cosh kh} [\dot{A}(x_1, y_1, t_1, t_2) \exp(i(kx - \omega t)) + cc] \right) + O(\epsilon^2) \\ \zeta &= \epsilon \left(\frac{i\omega}{g + Tk^2} \dot{A} \exp(i(kx - \omega t)) + cc \right) + O(\epsilon^2) \end{aligned} \quad (3.6)$$

where $\dot{\Phi}$ represents the mean motion. At $O(\epsilon^2)$, the removal of secular terms produces an evolution equation which requires that the wave envelope travel with its group velocity ($C_g = d\omega/dk$).

$$\dot{A}_{t_1} + C_g \dot{A}_{x_1} = 0. \quad (3.7)$$

An additional equation for the mean motion is obtained (see Ablowitz and Segur, 1979).

To obtain the NLS equation, the expansion is carried to the next order, $O(\epsilon^3)$. When secularity is removed, and the results are cast into dimensionless form using the following scaling

$$\begin{aligned}\xi &= \epsilon k(x - C_g t), & \eta &= \epsilon k y, & \tau &= \epsilon^2(gk)^{1/2} t \\ \dot{A} &= k^2(gk)^{-1/2} \dot{A}, & \dot{\Phi} &= k^2(gk)^{-1/2} \dot{\Phi},\end{aligned}\tag{3.8}$$

the evolution equations are

$$i \dot{A}_\tau + \lambda \dot{A}_{\xi\xi} + \mu \dot{A}_{\eta\eta} = \chi |\dot{A}|^2 \dot{A} + \chi_1 \dot{A} \Phi_\xi \tag{3.9a}$$

$$\alpha \Phi_{\xi\xi} + \Phi_{\eta\eta} = -\beta (|\dot{A}|^2)_\xi \tag{3.9b}$$

where

$$\sigma = \tanh kh, \quad \hat{T} = k^2 T/g \tag{3.10a}$$

$$\omega^2 = gk\sigma(1 + \hat{T}), \quad \omega_0^2 = gk, \quad \lambda = k^2 \left(\frac{d^2\omega}{dk^2} \right) / 2\omega_0 \tag{3.10b}$$

$$\mu = k^2 \left(\frac{\partial^2 \omega}{\partial m^2} \right) / 2\omega_0 = \frac{kC_g}{2\omega_0} \tag{3.10c}$$

$$\begin{aligned}\chi = \left(\frac{\omega_0}{4\omega} \right) &\left\{ \frac{(1 - \sigma^2)(9 - \sigma^2) + \hat{T}(3 - \sigma^2)(7 - \sigma^2)}{\sigma^2 - \hat{T}(3 - \sigma^2)} \right\} + \\ &\left(\frac{\omega_0}{4\omega} \right) \left\{ 8\sigma^2 - 2(1 - \sigma^2)^2(1 + \hat{T}) - \frac{3\sigma^2 \hat{T}}{1 + \hat{T}} \right\} \end{aligned}\tag{3.10d}$$

$$\chi_1 = 1 + \frac{kC_g}{2\omega} (1 - \sigma^2)(1 + \hat{T}) \tag{3.10e}$$

$$\alpha = (gh - C_g^2) / gh \tag{3.10f}$$

$$\beta = \left(\frac{\omega}{\omega_0 kh} \right) \left\{ \frac{kC_g}{\omega} (1 - \sigma^2) + \frac{2}{1 + \hat{T}} \right\} \tag{3.10g}$$

$$\nu = \chi - \chi_1 \beta / \alpha \tag{3.10h}$$

Equations (3.9a) and (3.9b) are the NLS equation in two space dimensions and time, i.e. (2+1), coupled with a long-wave equation for the mean motion. The NLS equation in two spatial dimensions for gravity waves was derived by Zakharov (1968), Benney and Roskes (1969), and Davey and Stewartson (1974). Djordjevic and Redekopp (1977) and Ablowitz and Segur (1979) derived the equations in the form (3.9), which includes surface tension. The coefficients of (3.9) given in (3.10) are calculated using the wavevector $\mathbf{k} = (l_0, m_0 = 0)$ of the underlying wavetrain. Misprints in Djordjevic and Redekopp (1977) and Ablowitz and Segur (1979) have been corrected in (3.9) and (3.10).

Equation (3.9) does not appear to be analytically tractable (Ablowitz and Segur, 1979); however, a variety of approximations are. For example, neglecting transverse variations, i.e. $\partial/\partial\eta = 0$, (3.9b) can be integrated, and thus (3.9) yields

$$i \dot{A}_\tau + \lambda \dot{A}_{\xi\xi} = \nu |\dot{A}|^2 \dot{A} \quad (3.11)$$

$$\dot{\Phi}_\xi = -\beta/\alpha |\dot{A}|^2. \quad (3.12)$$

Equation (3.11) is the NLS equation in one space and one time dimension (1+1), and it describes the evolution of a wavetrain whose envelope is modulated in the longitudinal direction. This equation was derived by Benney and Newell (1967) and Hasimoto and Ono (1972). Zakharov and Shabat (1972), found a scattering problem that allowed (3.11) to be solved exactly using Inverse Scattering Theory. They showed that initial data, which vanishes sufficiently fast as $|\xi| \rightarrow \infty$, evolves into a finite number of envelope solitons and a continuous spectrum of oscillatory waves. The solution of (3.11) depends critically on the signs of the coefficients of the equations. The critical dividing lines are established by the sign of the quantity,

$(\lambda\nu)$. When $\lambda\nu < 0$, the region is unstable (this represents all three unstable regions and is known as the Benjamin-Feir (B-F) instability); conversely, when $\lambda\nu > 0$, the region is stable. A map of parameter space showing where sign changes occur and regions of stability (S) and instability (U) is presented in figure 3.2. A similar figure was used by Djordjevic and Redekopp (1977), Ablowitz and Segur (1979), and Henderson and Lee (1986). For large kh , λ changes sign at approximately 6.4 Hz (or $\dot{T} = 0.1547$) or across curve C_1 . Along curve C_2 , ν has a singularity which corresponds to second harmonic resonance known as Wilton Ripples. The curve, C_3 , across which α and ν change sign and ν is singular, signifies that a long wave-short wave resonance has occurred. (This case has been investigated by Djordjevic and Redekopp, 1977). The parameter locations for the experiments presented herein, are also shown in figure 3.2; they occur in three separate regions. The 8 Hz experiments are in a stable region, while the 9.8 Hz wavetrains, located on curve, C_2 , correspond to Wilton ripples. The remaining experimental wavetrains are in a B-F unstable region.

We present an outline of the stability analysis of the NLS equation which follows that of Hasimoto and Ono (1972). Transforming (3.11) to a dimensional equation using $\tau = \epsilon^2(gk)^{1/2}\dot{\tau}$, $\xi = \epsilon k \dot{\xi}$, and $\dot{A} = k^2(gk)^{-1/2} \hat{A}$, yields

$$i \dot{A}_\tau + \lambda \dot{A}_{\dot{\xi}\dot{\xi}} = \nu |\dot{A}|^2 \dot{A} \quad (3.13)$$

where $\nu = \nu k^4(gk)^{-1/2}$ and $\lambda = \lambda k^{-2}(gk)^{1/2}$. First, we seek a nonlinear plane wave solution of the NLS equation which has an oscillatory envelope of the form

$$\dot{A}(\dot{\tau}, \dot{\xi}) = \dot{A}_0 e^{i(\Omega\dot{\tau} - K\dot{\xi})} \quad (3.14)$$

where \dot{A}_0 is a constant (possibly complex) amplitude, Ω is the modulation fre-

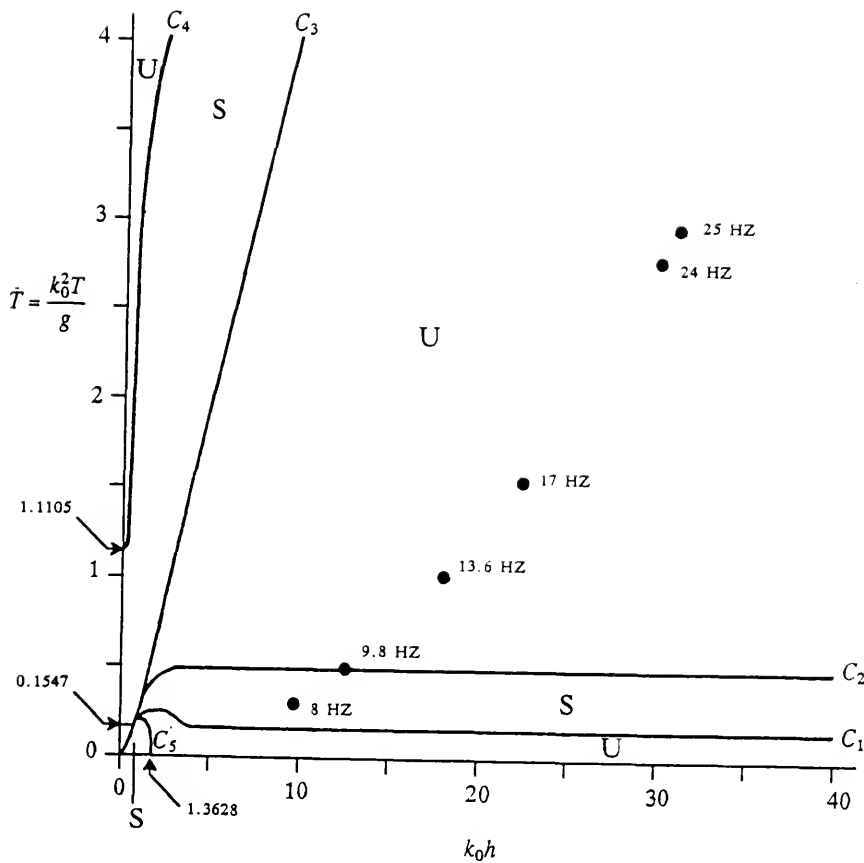


Figure 3.2 Parameter space of the nonlinear Schrödinger equation showing regions of stability (S) and instability (U) of a wavetrain to longitudinal modulations. Curve C_1 corresponds to zeros of λ ; curves C_4 and C_5 correspond to zeros of v ; Curves C_2 and C_3 correspond to singularities of v . The location of parameters (●) for each experiment is also shown. (Hammack, private communication, 1989).

quency, and K is the modulation wavenumber. Substituting (3.14) into (3.13) yields the dispersion relation for the wave envelope

$$\Omega = -\dot{\lambda} K^2 - \dot{v} |\dot{A}_0|^2. \quad (3.15)$$

If we set $K=0$ and $\dot{A}_0 = -i(g + Tk^2)a_0/2\omega$, where a_0 represents the physical wave amplitude, then (3.15) gives the dispersion relation for a uniform wavetrain with a nonlinear correction to its linear frequency. For gravity waves ($T=0$), this wavetrain represents the well-known Stokes solution with the third order frequency correction ($\dot{\omega} = \omega [1 + (1/2) k^2 a_0^2]$).

To determine whether a wavetrain is stable, we introduce a perturbation of the form

$$\dot{A}(\dot{\tau}, \dot{\xi}) = (\dot{A}_0 + \dot{\epsilon} B) e^{i(\Omega\dot{\tau} + \dot{\epsilon} b)} \quad (3.16)$$

and determine its time evolution. In (3.16), $B = B(\dot{\tau}, \dot{\xi})$ is a pure imaginary perturbation of the complex amplitude, $b = b(\dot{\tau}, \dot{\xi})$ is a real perturbation of wave phase, and $\dot{\epsilon} \ll 1$ is a small ordering parameter. Substitution of (3.16) into (3.13), and retaining terms through first order, yields two equations. The zeroth order equation is satisfied identically. The first order equation, for which the real and imaginary parts must be satisfied separately, gives

$$-i B_{\dot{\tau}} + \dot{\lambda} |\dot{A}_0| b_{\dot{\xi}\dot{\xi}} = 0 \quad (3.17a)$$

$$i \dot{\lambda} B_{\dot{\xi}\dot{\xi}} - i 2 \dot{v} |\dot{A}_0|^2 B + |\dot{A}_0| b_{\dot{\tau}} = 0. \quad (3.17b)$$

Equations (3.17a) and (3.17b) are a coupled set of linear differential equations with constant coefficients; hence, we assume solutions of the form

$$B(\dot{\tau}, \dot{\xi}) = B_0 e^{i(\dot{K}\dot{\xi} - W\dot{\tau})} + cc \quad (3.18a)$$

$$b(\dot{\tau}, \dot{\xi}) = b_0 e^{i(\dot{K}\dot{\xi} - W\dot{\tau})} + cc \quad (3.18b)$$

where B_0 and b_0 are taken to be real constants and \dot{K} and W are the perturbation wavenumber and frequency. When W is pure imaginary and positive, the perturbation will grow at an exponential rate, $|W|$. Substitution of (3.18) into (3.17) yields

$$-WB_0 - \lambda |\dot{A}_0| \dot{K}^2 b_0 = 0 \quad (3.19a)$$

$$(2\dot{\nu} |\dot{A}_0|^2 + \lambda \dot{K}^2) B_0 + W |\dot{A}_0| b_0 = 0. \quad (3.19b)$$

The determinant of (3.19) must vanish for nontrivial solutions. This condition leads to a dispersion relation for the perturbation wavenumber and frequency, namely

$$W^2 = \dot{\lambda}^2 \dot{K}^2 (\dot{K}^2 + (2\dot{\nu} |\dot{A}_0|^2)/\dot{\lambda}^2) \quad (3.20)$$

When $\dot{\lambda}\dot{\nu}$ is positive, W is real and the perturbations do not grow. However, when $\dot{\lambda}\dot{\nu}$ is negative, W can be imaginary and positive so that the perturbation grows, i.e. the wavetrain is unstable. Instability occurs when

$$\dot{K} < (-2\dot{\nu}/\dot{\lambda})^{1/2} |\dot{A}_0|. \quad (3.21)$$

Also, we define the limiting wavenumber as $\dot{K}_{\max} = (-2\dot{\nu}/\dot{\lambda})^{1/2} |\dot{A}_0|$. Therefore, as shown by Hasimoto and Ono (1972), gravity waves ($\dot{T} = 0$) in the regime where $\dot{\lambda}\dot{\nu}$ is negative ($kh > 1.3628$) and (3.21) is valid, are unstable. For the modu-

lation wavenumbers which satisfy (3.21) and for which $\dot{\lambda}\dot{\nu}$ is negative, the growth rate is

$$|W| = (-2\dot{\lambda}\dot{\nu} |\dot{A}_0|^2 \dot{K}^2 - \dot{\lambda}^2 \dot{K}^4)^{1/2}. \quad (3.22)$$

Finally, the most unstable sideband, \dot{K}_m , and its growth rate, $|W|_m$ occur where the derivative of (3.22) with respect to \dot{K} vanishes. This calculation yields

$$\dot{K}_m = (-\dot{\nu}/\dot{\lambda})^{1/2} |\dot{A}_0| \quad (3.23)$$

$$|W|_m = -\dot{\nu} |\dot{A}_0|^2. \quad (3.24)$$

Obviously, the maximum unstable wavenumber, the maximum growth rate, and the most unstable sidebands are functions of the wavetrain amplitude. (Also, note that $\dot{K}_{\max} = \sqrt{2} \dot{K}_m$).

3.2 The Stationary, NLS Model

The motivation for the following model is based on experimental measurements in which the envelopes appear to be steady. Also, the transverse modulational wavenumbers are larger than the longitudinal values. If the latter of these two observations is assumed, the terms in (3.9), which contain derivatives in ξ , are negligible at leading order. These equations decouple, and (3.9a) becomes

$$i \dot{A}_t + \mu \dot{A}_{\eta\eta} = \chi |\dot{A}|^2 \dot{A}. \quad (3.25)$$

Transforming (3.25) to laboratory coordinates and dimensional form, using the transformation

$$\begin{aligned} x &= \epsilon^{-1}k^{-1}\xi + \epsilon^{-2}C_g(gk)^{-1/2}\tau \quad , \quad y = \epsilon^{-1}k^{-1}\eta \quad , \\ t &= \epsilon^{-2}(gk)^{-1/2}\tau \quad , \quad \dot{A} = k^2(gk)^{-1/2}\dot{A} \end{aligned} \quad (3.26)$$

we obtain

$$i(\dot{A}_t + C_g \dot{A}_x) + (\mu k^{-2}(gk)^{1/2}) \dot{A}_{yy} = (\chi k^4(gk)^{-1/2}) |\dot{A}|^2 \dot{A} \quad (3.27)$$

Experimental results show that our wavefields are quasi-steady (herein, quasi-steady describes a process which is steady (has no temporal dependence) over many periods of the underlying wave); therefore, the time derivative term in (3.27) is negligible. These approximations result in a stationary NLS (sNLS) equation with the form

$$i\dot{A}_x + \mu \dot{A}_{yy} = \chi |\dot{A}|^2 \dot{A} \quad (3.28)$$

where $\mu = \mu k^{-2}(gk)^{1/2}C_g^{-1}$ and $\chi = \chi k^4(gk)^{-1/2}C_g^{-1}$. Equation (3.28) has the same form as (3.13); however, the independent variables $(\dot{\tau}, \dot{\xi})$ have been replaced by (x, y) , and the coefficients, (λ, ν) , have been replaced by (μ, χ) . Since the equations are analogous, we may glean our results directly from the stability analysis in Section 3.1.

If we assume oscillatory modulations in space of the form

$$\dot{A}(x, y) = \dot{A}_0 e^{i(p_x x + q_y y)} \quad (3.29)$$

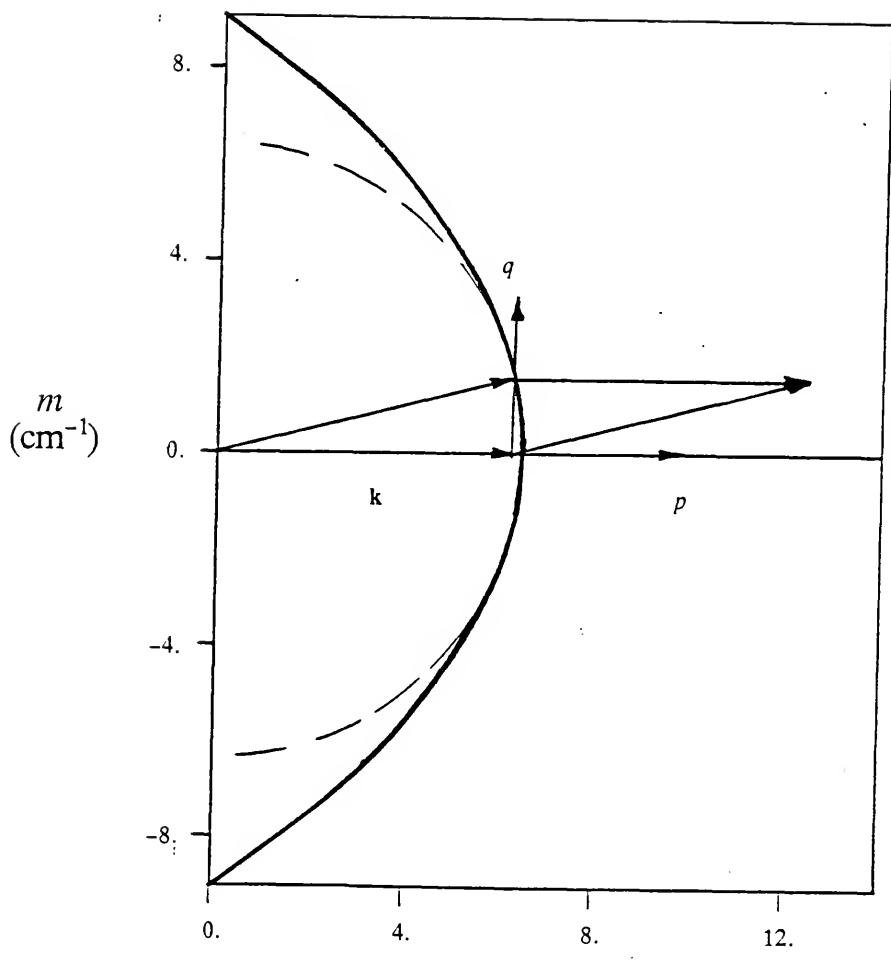
we obtain the dispersion relation for the wave envelope, analogous to (3.15) as

$$\mu q^2 + p = -\chi |\dot{A}_0|^2 . \quad (3.30)$$

Figure 3.3 shows this dispersion relation, which is a parabola in the wavenumber plane, for the 25 Hz experiment presented in figure 5.1. The shape of the parabola is nearly circular in the vicinity of the input wavevector as shown by the dashed, circular arc in figure 3.3. This approximation is reasonably accurate to angles of $\pm 30^\circ$. Since the magnitudes of the wavenumbers along this portion of the curve are nearly constant, the frequencies calculated from (3.4) are nearly equal. Therefore, although many waves propagating in different directions may be present, frequency spectra will only show energy at one frequency.

Any coordinate along the parabola in figure 3.3 represents a wavevector, which forms a degenerate quartet (four-wave resonance) with the input wavevector; one quartet is shown in figure 3.3. (Note that the input wavevector does not lie on the parabola.) If the transverse wavevector, q , is zero, a degenerate, collinear quartet is present. In the derivation of the NLS equation one assumes weak, two dimensionality, and so equation (3.30) should only be valid for small values of p and q .

For the sNLS equation, (3.28), we present analogous results to the linear stability analysis of Hasimoto and Ono (1972) presented in Section 3.1. Rather than determining the most unstable wavenumber, the maximum wavenumber of the instability, and the temporal growth rate, the analysis now predicts the most unstable wavenumber in the y direction, the maximum wavenumber of the instability in the y direction, and the spatial growth rate in the x direction. We will use perturbation wavenumbers, P and Q , for the x and y directions, respectively. According to



$$l \text{ (cm}^{-1}\text{)}$$

Figure 3.3 The dispersion relation of (3.30) calculated for a 25 Hz wavetrain with $a=0.04$ cm. The (p,q) coordinate system is shown along with a degenerate, side-band quartet. The dashed line is a circle, centered at $(0,0)$, with a radius equal to the parabolic vertex coordinate.

the linear stability analysis, P must be imaginary and positive for perturbations to grow in space, and therefore, it restricts the admissible wavenumbers in the y direction. We set $q=0$ so the wavetrain represents a nonlinear plane, G-C wavetrain in space (with $\dot{A}_0 = [-i(g + Tk^2)/(2\omega)] a_0$ for a real, physical wave amplitude, a_0 , and a slightly different wavenumber than for the linear wavetrain), and then seek instabilities which grow in space. The following inequality (and the maximum sideband value) must be valid in order that the perturbation grow and an instability result

$$Q < (-2 \dot{\chi}/\mu)^{1/2} |\dot{A}_0| \equiv Q_{\max}. \quad (3.31)$$

The most unstable sideband and maximum spatial growth rate are

$$Q_m = (-\dot{\chi}/\mu)^{1/2} |\dot{A}_0| \quad \text{and} \quad |P|_m = -\dot{\chi} |\dot{A}_0|^2. \quad (3.32)$$

Herein, $\pm Q_{\max}$ will be shown in figures to indicate the allowable spreading of wave energy according to this linear stability analysis. The angle associated with this spreading is termed θ . As noted by Yuen and Lake (1982), the fact that the instability of the waves can only occur in a fairly narrow band (about the input k), preserves the assumption of a narrow-banded spectra used to derive the evolution equations.

For gravity waves, the analogous equation to (3.28) has a different sign for the nonlinear term (ie. χ changes sign and has a positive value). This form of the NLS equation cannot be unstable. Thus, the instability we present is uniquely applicable to G-C waves.

While three-dimensional instabilities of G-C waves have been studied previously, e.g. by Zhang and Melville (1986 and 1987) and Chen and Saffman (1985),

the stationary, spatial instability described above appears to have been overlooked. This is a consequence of examining instabilities by positing perturbations whose temporal behavior is used to define stable and unstable regimes.

In our experiments, amplitudes vary significantly in space due to viscous damping (and also due to the instability we are investigating); however, we will use only one measured amplitude, a_0 as a representative value. Since the unstable sidebands depend on a_0 and growth rates depend on a_0^2 , some discrepancies between theoretical and experimental results are anticipated. To predict an amplitude at a specific location using a value from another location requires a viscous model. Henderson and Lee (1986) have shown that an immobile-surface model is appropriate when the facilities and procedures used herein are employed. According to this model, the amplitude envelope decays as

$$A(x) = A_0 \exp(-\delta x) \quad (3.33)$$

$$\text{where } \delta = \left(\Gamma + \frac{k_0(\nu \cdot \omega/2)^{1/2} \cosh^2 k_0 h}{C_g \sinh 2k_0 h} \right) ,$$

$$\Gamma = \left(\frac{\nu \cdot \omega}{2} \right)^{1/2} \left(\frac{1}{2h} \right) \left(\frac{2k_0 h}{\sinh 2k_0 h} + \frac{h}{b} \right) C_g^{-1} \quad (3.34)$$

b is the channel width, and $\nu \cdot$ is the kinematic viscosity of water. Hence, the e-folding distance for viscous damping is 1/8. In addition to damping, viscosity causes wavelengths to decrease slightly from those predicted by the inviscid dispersion relation.

CHAPTER 4

EXPERIMENTAL FACILITIES, PROCEDURES AND IMAGE ANALYSIS FOR PART 1

The experimental facility was specifically designed and constructed to study gravity-capillary (G-C) waves. It consists of six systems: (1) the wave tank, (2) the wave generator and its electronics, (3) the water supply and filtering system, (4) the wave gauge and its attendant electronics, (5) the computer system, and (6) the high-speed imaging system. Systems (1) through (4) have been discussed in detail by Henderson and Hammack (1987), and they are described briefly herein. The computer and high-speed imaging systems have been recently integrated into the laboratory. These two systems provide unique measurements of spatial wave data which is of special importance to the results reported herein. Hence, they are described in detail. Data analysis techniques are also discussed with an emphasis on the spatial data obtained by the imaging system.

The wave tank, shown schematically in figure 4.1, is 91 cm wide, 183 cm long and 15 cm deep. It consists of tempered glass sidewalls and bottom in an aluminum frame with aluminum end walls. A sheet of white plexiglass is located beneath the glass bottom. (This sheet is required for imaging purposes.) Temporary wave guides made of (wetted) aluminum are set adjacent to the wavemaker paddle to create a wave channel 30.5 cm wide within the 91 cm width of the basin. The tank is supported by a steel frame which rests on vibration-isolation pads. The entire inside of the tank is cleaned before and after experiments with ethyl alcohol.

(a)

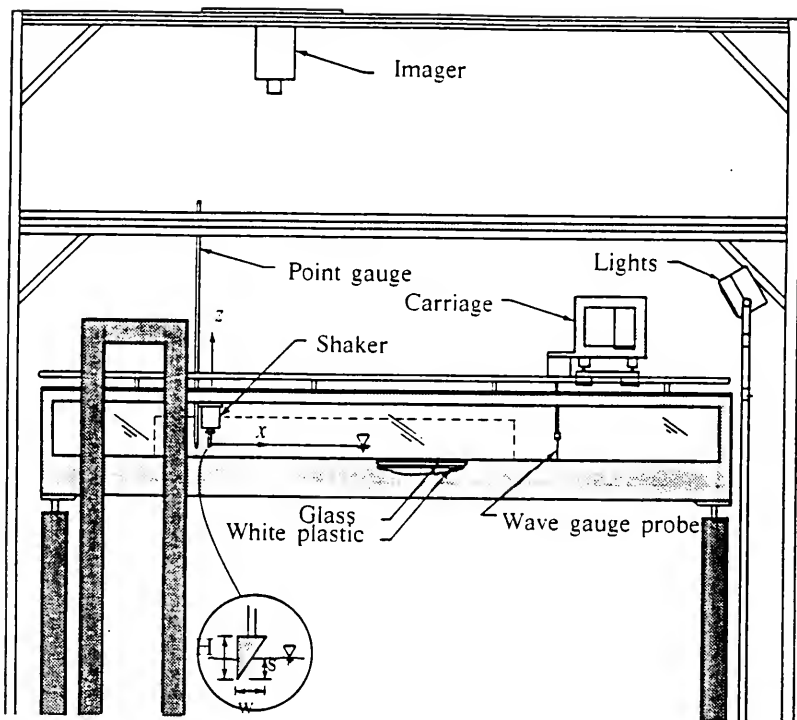


Figure 4.1 The experimental facility and coordinate system. An elevation view is shown in (a) and a plan view in (b).

(b)

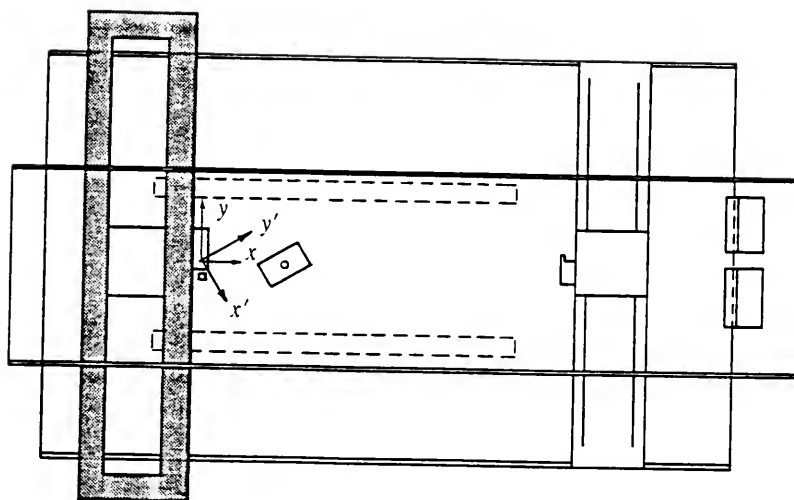


Figure 4.1-continued

The wavemaker paddle is supported by an electrodynamic shaker connected to another steel frame which straddles the wave tank and rests on vibration-isolation pads as shown in figure 4.1. The paddle is an aluminum right-angled wedge with a length of 30.4 cm, a height (H) of 0.90 cm, and a width (w) of 0.44 cm. In figure 4.1 an enlarged view of the paddle is shown, including its position with respect to the water surface. It should be emphasized that the paddle submergence, s , must be duplicated among experiments in order to obtain repeatable results. Herein, all experiments have a depth of paddle submergence of 0.24 cm. An eddy-current displacement transducer monitors the vertical motion of the paddle and provides a position-feedback signal to a servo-controller. The controller compares the programmed displacement signal with the feedback signal, and corrects wavemaker motion to strictly follow the desired motion. The maximum displacement of the wavemaker is 6 mm (which corresponds to a 6-volt command signal); however for the experiments reported herein, displacements never exceed 3 mm. For the experiments reported in Part 1, all wavemaker input signals are sinusoidal.

The water supply system contains 80 gallons of water stored in two closed polyethylene containers that are connected to the wave basin by PVC piping and valves. The Sybron filtration system consists of a 0.2 micron particle filter, a carbon-absorption filter, and an organics removal filter. The water is gravity-fed into the wave tank, and pumped very slowly through the filtration system at the conclusion of an experiment.

A capacitance-type wave gauge is used to record the water surface elevation as a function of time at a fixed location, (x_0, y_0) , in the basin. The water-penetrating probe is a sealed glass tube enclosing a conductor and has diameter of 1.17 mm. Unlike the probe used by H-H, the dynamic response of this gauge is essentially constant until about 30 Hz. The wave gauge is calibrated dynamically by oscillating

it vertically with a known frequency and amplitude, and then comparing this amplitude to the voltage of the output signal. (See H-H for details of the calibration procedure.)

4.1 The Imaging and Computer Systems

The computer system used in these experiments is a DEC VAXstation II. This 32-bit system contains an analog-output system (AAV11-DA), with up to 4 channels of output, and an analog input system (ADV11-DA) with up to 16 channels of input. Two real-time clocks (KWF11-C) are used in conjunction with the digital-to-analog output and the analog-to-digital input. Data acquisition and analysis, as well as command signals to the wave generator, are performed by the computer system via the command language of Signal Technology's Interactive Laboratory System (ILS) software. A command procedure of ILS instructions, once initiated, automatically acquires time series data and analyzes it in near real-time. Numerical and graphical programs from the DEC VAXlab software are also used. A 71 mega-byte (RD53) system disk and a 456 mega-byte (RA81) storage disk are used for data acquisition and processing. In addition to the wave gauge data, the command and feedback signals of the wavemaker are also recorded simultaneously and analyzed. The computer is interfaced to the imaging system through an RS-232 connection which allows transfer of control commands and data between the two systems.

The high-speed video imaging system is a Kodak Ektapro 1000, computer-based device, capable of processing data from two imagers at framing rates up to 1000 Hz. Each frame can be divided into as many as 6 pictures to produce up to 6000 pictures per second. Each image is formed from a 240 (horizontal) by 192 (vertical) pixel-array with a resolution of 256 gray levels (intensity) per pixel. Images are recorded on one-half inch instrument tape and, during playback, are then

digitized by the processor at a rate of 30 frames per second. Both imagers are used in the experimental program (though not necessarily concurrently); one imager is located directly above the water surface and the other is located at the end of the tank to give an oblique view of the wavefield. A 25 mm TV lens, with an f/stop as low as 0.95, is used with the overhead imager, while an 11-66 mm zoom lens is used with the other imager.

Using Kodak's command language, digitized images can be downloaded through the RS-232 connector from the Ektapro 1000's computer memory to the VAXstation II system. Since it is desirable to maintain the array size as a multiple of "2" in order to be compatible for numerical analysis, a 128 x 128 pixel array is transferred. Figure 4.2 shows a typical overhead image of the quiescent water surface when viewed on the system monitor. A rectangular border has been marked to delineate the area of the image which is transferred and processed in the analyses. Note that this sampling area is oriented at an angle of about 45° to the channel axis (also see figure 4.1). The reason for this orientation will be discussed in the next section. The channel sidewalls are also visible in figure 4.2. Figure 4.3 shows a typical overhead image from an experiment in which an 8 Hz wavetrain has been generated. The dominant light and dark bands transverse to the channel axis represent the crests and troughs, respectively, of the 8 Hz wavetrain. (Even the 24 Hz superharmonic of the 8 Hz wavetrain is visible in figure 4.3!) More details concerning the interpretation of these overhead images will be presented shortly.

4.2 Data Analysis Procedures

Wave gauge data are digitized and analyzed by the computer in near real-time. These data are analyzed to produce amplitude-frequency spectra (amplitude periodograms). The time series of water surface elevation, $\zeta(x_0, y_0)$, are low-pass

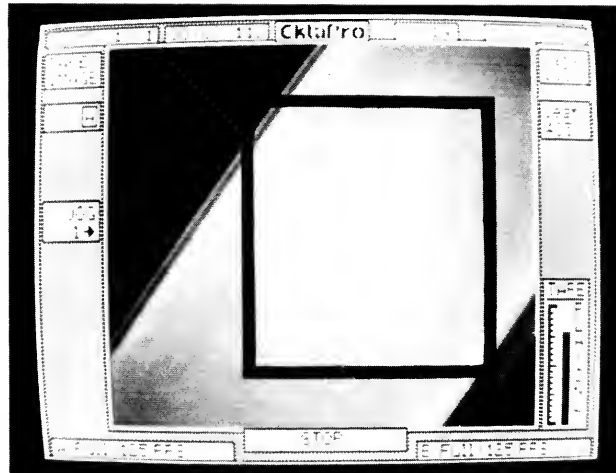


Figure 4.2 A typical quiescent background image (taken prior to each experiment) with a frame superposed to depict the region used by the two-dimensional transform.

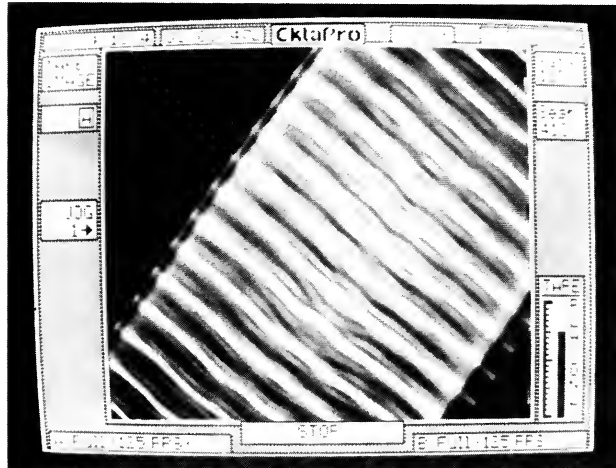


Figure 4.3 An overhead image of an 8 Hz experiment (GC0806).

analog (Butterworth) filtered with a cutoff frequency of 100 Hz, digitized at a rate of 250 Hz, amplified by 20 decibels, high-pass analog filtered at a cutoff frequency of 1 Hz, and then amplified by another 20 decibels. (A 20 decibel amplification corresponds to a factor of 10.) The duration of the time series is 65.532 seconds, or equivalently, 16,384 samples. The temporal resolution is 0.004 sec, and the resolution in the amplitude-frequency spectra is 0.0153 Hz. Thus, the Nyquist (folding) frequency is 125 Hz. Therefore, analog filtering at 100 Hz removes any corruption due to aliasing of the amplitude-frequency spectra. The command signal to the wavemaker is provided by analog output from a 2500 Hz digital signal. The command and feedback signals of the wavemaker system are also digitized and analyzed to provide a check on the experimental input. Note that all frequency spectra herein are presented in terms of decibel wave amplitudes, instead of cm-wave amplitudes. The decibel amplitude is $20 \log_{10}$ (amplitude signal). The frequency spectra are computed by using fast Fourier transforms (FFT) of the time series.

The overhead images, such as the one shown in figure 4.3, are analyzed using a two-dimensional FFT to obtain the amplitude-wavenumber spectrum of the wavefield. An array of 27×27 (16,384) samples is used by the transform. Prior to the analysis of the wavefield image, an image of the quiescent water surface, obtained prior to each experiment (e.g. see figure 4.2), is subtracted from the wavefield data. This removes any variation in background lighting and/or inhomogeneities in the response of the imager sensors. Second, a mean-value of the gray-levels for the wavefield image is subtracted from each pixel value. Of a possible 256 gray-levels available per pixel, experiments, herein, used as many as 225 gray-levels. The resolution of the images is 0.174 cm which gives a wavenumber resolution of 0.284 rad/cm. The folding (Nyquist) wavenumber is 18.055 rad/cm,

or equivalently, a free wave with a frequency of 106.5 Hz. Although no method for analog filtering of the image is available, it is believed that no significant wave activity is present at, or beyond, this frequency in our experiments. The image resolution (0.174 cm for the experiments, herein) was determined by viewing a linear scale located in the plane of the quiescent water surface. Then, the imager's reticle was used to determine the number of pixels along a known distance on the scale. This procedure was then repeated in a direction perpendicular to the first orientation to insure that both axes of the imager gave identical resolutions. The framing rate of the imager for the experiments presented herein is 125 Hz.

As already shown in figures 4.2 and 4.3, the imaged area of the water surface was oriented at an angle of about 45° to the axis of the channel. This orientation is advantageous due to the manner in which the FFT algorithm computes the amplitudes corresponding to a given wavenumber. The algorithm only associates amplitudes with the $(+l,+m)$ quadrant of the wavenumber plane. Hence, it "folds" amplitudes for wavevectors oriented in the $-m$ direction (i.e. waves propagating such that they have a component wavenumber in the $-y$ direction, across the channel) into the $+m$ -direction. Similarly, it folds amplitudes in the $-l$ direction. Hence, orienting the image at an angle of about 45° allows us to distinguish wave directions up to $\pm 45^\circ$ from the $+x$ -channel axis. Since the waves in these experiments are concentrated within an angle of $\pm 45^\circ$ to the channel axis, the folding does not contaminate the computed spectra in a significant manner.

One problem with numerical calculations, such as the use of FFT's, is the "smearing" of information which results from representing continuous functions with discrete functions. In the calculation of the wavenumber spectra, amplitudes are smeared to adjacent wavevectors. In order to determine how this discretization affects wavenumber spectra, an analytical sinusoidal wavetrain was digitized and

used as direct input to the two-dimensional FFT. This effect is shown in figure 4.4 where computed spectral contour maps in the wavenumber plane are presented. The first three maps have been calculated with an input wavenumber of 6.325 (25 Hz) and input angles with respect to the abscissa, Ξ , of 420, 450 and 480. Note that the smearing for the 420 wavevector is mostly in the abscissa direction while the smearing for the wavevector oriented at 480 is mostly in the ordinate direction. The "criss-cross" effect is present in the case of a 450 wavevector, although smaller, and, in fact, this contour map very much resembles the 17 Hz, small-amplitude case (see figure 5.7). The fourth map in the figure is also a 450 wavevector, however its input wavenumber magnitude is now 6.20. By simply changing the wavenumber so that it falls near the midpoint of adjacent wavenumber "bins", the "criss-cross" effect has been significantly increased, both in extent and breadth. It is noted that this effect would be reduced by decreasing the discretization interval between image gray-levels (i.e. a larger number of known gray-levels for the same physical area). This "criss-cross" effect will appear in many of the contour maps. It is important to remember the numerical smearing (caused by the transform) when interpreting the contour maps of wavenumber space, since the spreading of wave amplitude caused by the physics of water waves is the main focus of Part 1.

4.3 Lighting and Image Effects

The major factor affecting images of the ripple surface is lighting. The images are very sensitive to the manner in which the surface is illuminated. Various lighting techniques were tried; however, the rear lighting is believed to be superior and, consequently, is used (note the position of the lights in figure 4.1). Two mechanically coupled, 600 watt halogen lights, in reflector housings, provide the lighting. The lights are centered on the wave channel. If the lighting is too direct, the imager

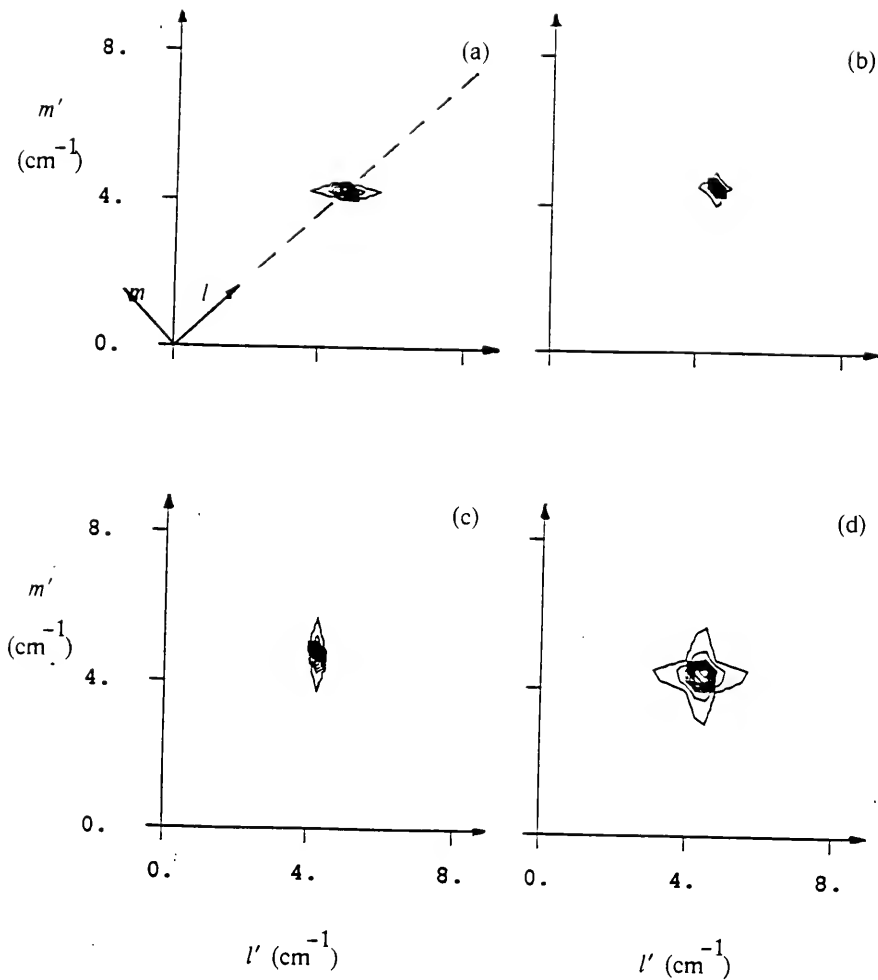


Figure 4.4 Demonstration of the “criss-cross” effect caused by the numerical two-dimensional FFT. These contour maps of wavenumber spectra are for sine waves with: (a) $k=6.325$ and $\Xi=420$, (b) $k=6.325$ and $\Xi=450$, (c) $k=6.325$ and $\Xi=480$, and (d) $k=6.200$ and $\Xi=450$.

is "overpowered" (i.e. the gray-level values reach 255). Too little light results in the opposite effect. Also, duplicate experiments, with varied lighting gave slightly different results. It is believed that the dominant wavenumber properties of the surface are being measured.

An explanation of the genesis of the image is now presented. Again, reference is made to figure 4.1: the bottom of the tank is shown to be tempered glass underlaid with a white, plastic sheet. The plastic sheet is used to help diffuse light. It is conjectured that light which penetrates the water surface and the glass bottom, is diffused by the plastic sheet; then, as it passes back through the water surface, it is refracted (i.e. water wave crests focus light while troughs reduce light intensity). Thus, an image has bright bands along wave crests and dark bands along troughs (see figure 4.3). Occasionally, images have extremely small, bright spots present, believed to be specular reflection. If the white plastic sheet is removed, the video image is essentially destroyed.

In order to demonstrate that the image is a consequence of diffuse rather than specular light, a simple, rather crude experiment was conducted. Using the overhead imager, and a quiescent water surface, the angle of the halogen lights, with respect to the vertical, was measured. An image of the water surface was recorded, transferred to the computer, and an average gray-level was computed. The angle of incident light was then changed and the process was repeated. The data from this experiment are represented by the asterisks in figure 4.5. The angle of the light source, Δ , as measured from the vertical is shown versus the average image intensity, κ . A significant reduction of light intensity from the maximum value measured is noted. (If the water surface was specular, the water surface would always appear black except when the light was originating from the imager direction.) Next, a light-intensity meter was used to measure the intensity of light versus de-

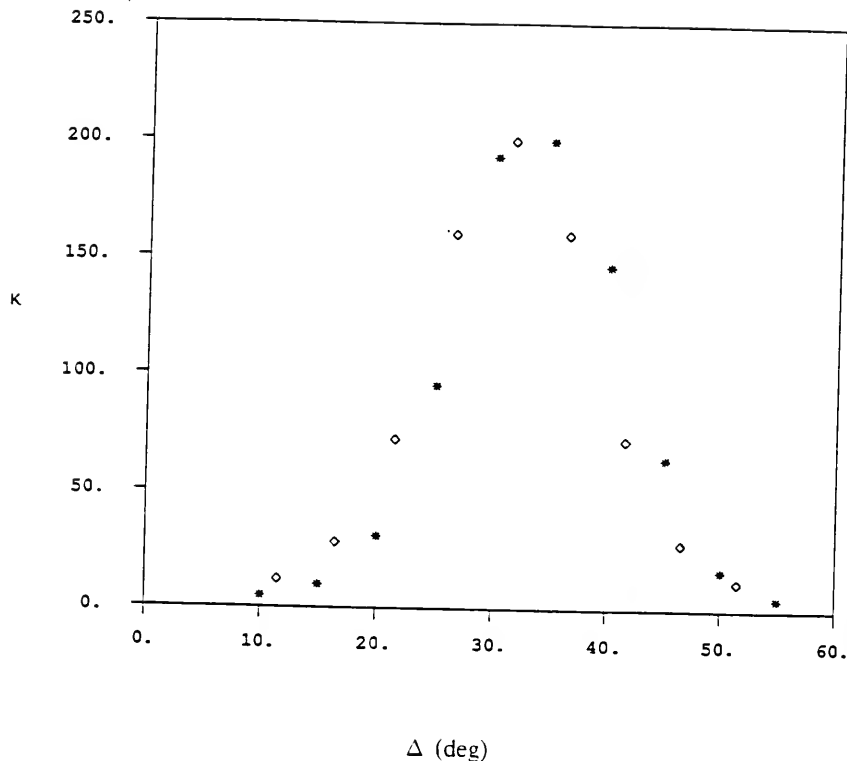


Figure 4.5 Average intensity level, κ , versus inclination angle of light from vertical, Δ , for a quiescent water surface (shown by asterisks). Diamonds represent the plane projection light intensity of the light source versus angle.

vation angle along the vertical centerline of a plane projection. The maximum intensity levels measured using the light meter were then normalized by the maximum average intensity obtained from the video images. These values are represented by the diamonds in figure 4.5. It is clear that the "surface" is diffuse reflective because the two curves are similar. The white plastic sheet is apparently responsible for the surface appearing to be diffuse. The intensity level differences between the two measurements is due to the difference between projecting light onto a perpendicular surface and onto an inclined surface and is consistent.

The following tests were performed in order to gain additional insight into the nature of the data obtained from the imaging system, as well as the interpretation of their wavenumber spectra. First, simple square-wave, planform patterns were drawn with black ink on white paper, placed in the wave tank, imaged and transformed. These patterns have known Fourier transforms which could then be compared with the results from the imaging. Reasonable agreement was found. Second, various known wavefields in terms of sea-surface elevation were generated numerically by superposing sinusoidal waves with different (known) wavevectors. For each wavefield, the maximum sea level was given a gray-level intensity of 255 and the minimum sea level a value of 0; intermediate water levels were assigned corresponding gray-levels by interpolation. This water surface to gray-level correspondence was used to generate an image on paper, and then the video system was used to image and transform it. A comparison between the known, input wavevectors and the wavenumber plane as calculated from the transformed image showed that the system was functioning well.

Finally, as with most remote sensing techniques, a question arises as to what is actually being measured, in this case, by the imaging and computing systems (i.e. amplitude, amplitude squared, or some other quantity). Verification that we are, in

fact, measuring amplitude is as follows. For low values of $k_0 s$, that is, wavenumber magnitude times paddle stroke, when the energy is nearly all confined to the input wavenumber vector, if the stroke is doubled, say, the amplitude of the peak concentrated at that wavenumber also approximately doubles. This is true as long as the energy is concentrated at the input wavenumber vector and it verifies qualitatively that we are measuring the amplitude (or the wave steepness, ka) and not another quantity.

CHAPTER 5

RESULTS AND DISCUSSION OF PART 1

The results of the experimental program are presented and discussed in this chapter. The first section gives experimental evidence as to the quasi-steadiness of the wavefield, and a time-series of wavenumber contour maps during temporal evolution preceding quasi-steadiness. In the second section, we present the experimental results and compare them to the sNLS theoretical predictions. A complete list of these experiments and important parameters are shown in Table 5.1.

5.1 Evolution of Quasi-steady Wavefields

In order to show that the wavefield is quasi-steady, figure 5.1 presents 2 seconds (-50 waves) of a typical time series for a moderate amplitude, 25 Hz experiment. (See Table 5.1, experiment GC2504, for the important parameters.) Modulations of the wavetrain are present; however, the frequency spectrum of this experiment's time series (see figure 5.6(c)), clearly shows that identifiable peaks exist only for the 25-Hz input wavetrain and its super harmonics. This wavetrain had the largest stroke of the 25 Hz experiments presented and, therefore, it is not expected to be well-represented by the theory. In fact, figure 5.5(c) shows a photograph of the image as seen on the video monitor, and one can see 180° phase shifts present in the wavefield. In spite of this strongly, nonlinear wavefield, the four contour maps of wavenumber spectra presented in figure 5.2 are remarkably similar. These spectra were calculated from images 1/25, 1/5, 1/2 and 1 second, respectively, after the spectrum of figure 5.9. Very little difference exists between the contour

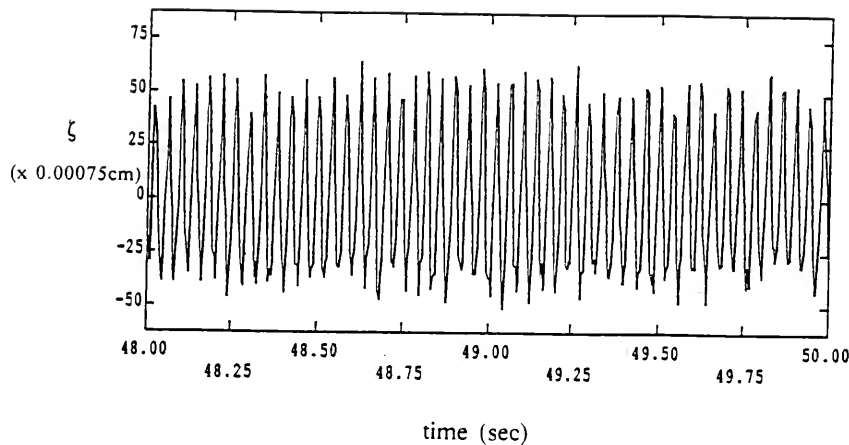


Figure 5.1 Two seconds of a time series from experiment GC2504.

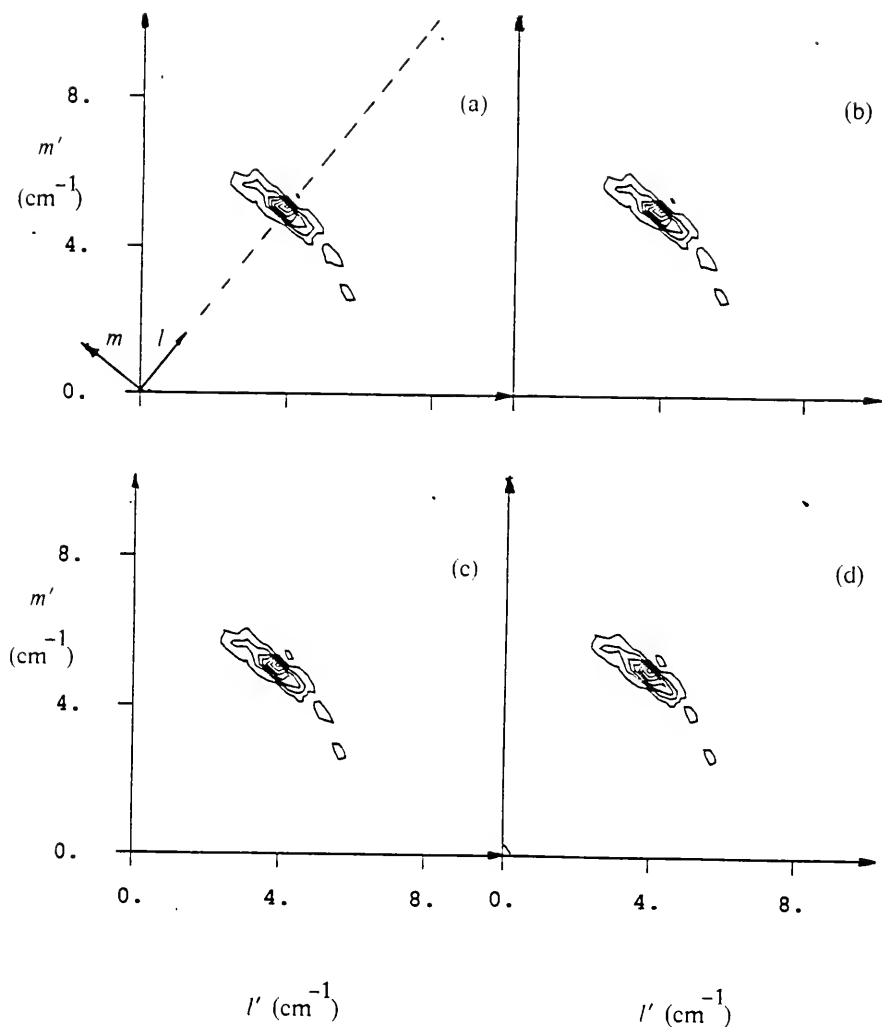


Figure 5.2 Demonstration of the quasi-steadiness of the 25 Hz wavefield of experiment GC2504. These contour maps of wavenumber spectra represent the wavefield (a) 1/25 sec, (b) 1/5 sec, (c) 1/2 sec, and (d) 1 sec after the contour map shown in figure 5.9.

maps. It is reasonable, then to state that the experiment is quasi-steady. We have thus shown that our experiments are not modulated in a "regular" fashion. However, modulations, in time, do exist but do not have a unique frequency at which energy appears in the frequency spectrum. Hence, the modulations appear in a random manner, and are partially attributed to "noise" in the experimental facility (e.g. air currents).

We now further define what is meant by quasi-steady. The time series for a 24 Hz wavetrain which precedes a quasi-steady wavefield is shown in figure 5.3. The length of this time series is 65.532 sec. Digitization of the wave gauge data began simultaneously with the start of the wavemaker. A time-sequence (3, 9, 21, 33, 45, 46, 47, and 57 sec) of contour maps of wavenumber spectra are presented in figure 5.4. Clearly, the wavenumber spectra are evolving as is evidenced by the large changes in the contours. Figures 5.4(c) and 5.4(d) show that numerical smearing of the data is present (i.e. the "criss-cross" effect). The evolution has reached a quasi-steady state at approximately 45 sec into the experiment. One second (-24 waves) has elapsed between recording of the images used to produce figures 5.4(e) and 5.4(f), yet the contour maps are very similar. A comparison of figures 5.4(f) and 5.4(g) shows little change, also. The wavefield imaged to produce figure 5.4(h) shows that slight evolution was still occurring, but on a longer time-scale.

5.2 Experimental Results and Comparison with sNLS Theory

In order to show that the sNLS equation predicts the directional spreading of amplitude for G-C waves of frequencies greater than 9.8 Hz, and that its prediction of stability for frequencies less than 9.8 Hz (but greater than 6.4 Hz) for deep, clean water is correct, five sets of experiments are presented. Paddle-driven wavetrains with frequencies of 25, 17, 13.6, 9.8, and 8 Hz are presented for three,

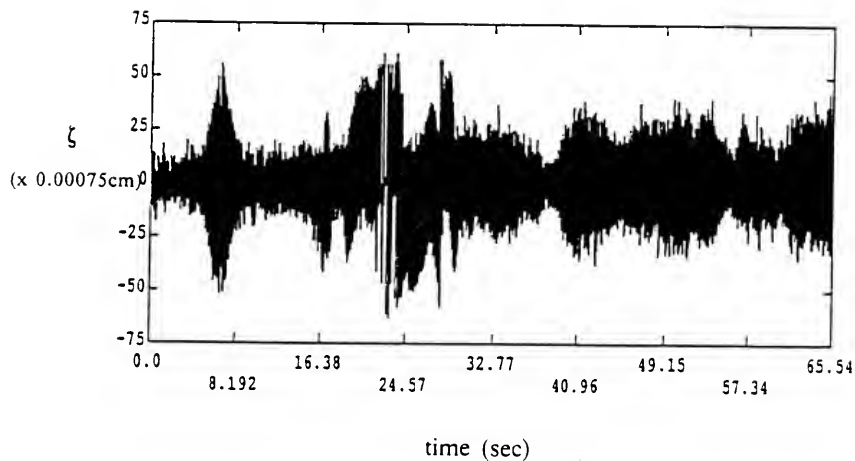


Figure 5.3 A time series of a 24 Hz wavetrain from wavemaker startup.

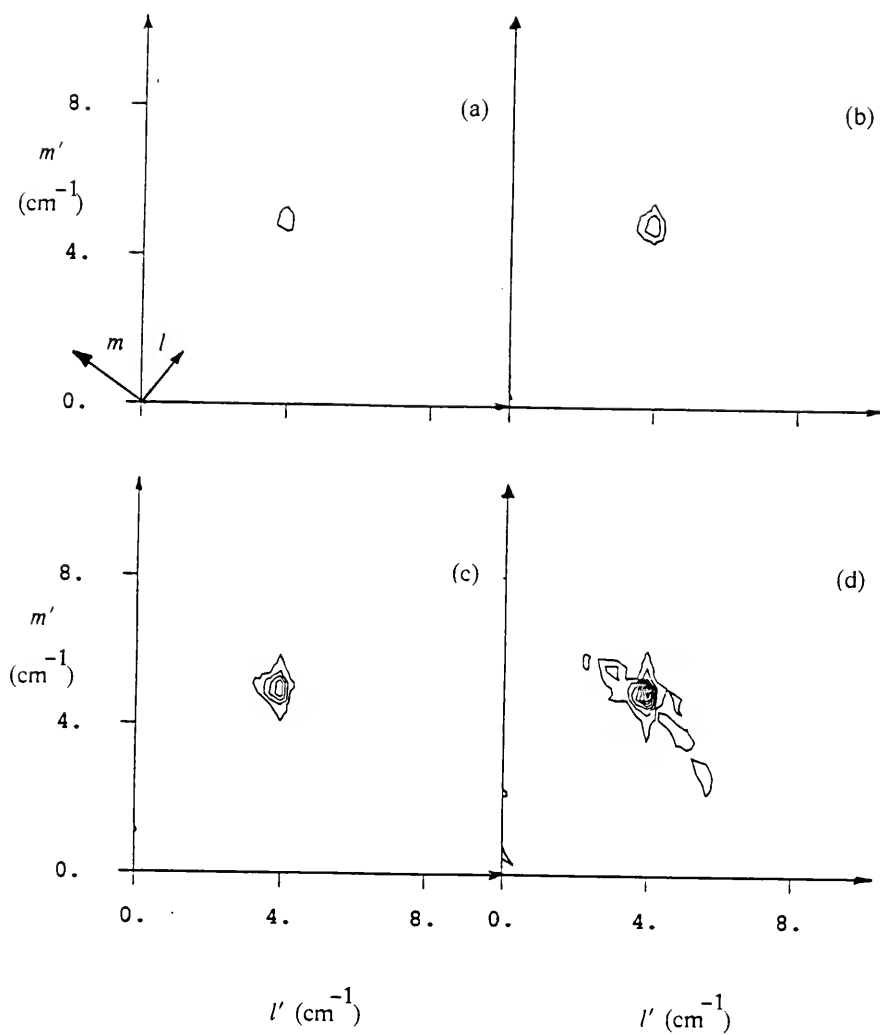


Figure 5.4 A time-sequence of contour maps of wavenumber spectra for a 24 Hz wavetrain approaching quasi-steadiness: (a) 3 sec, (b) 9 sec, (c) 21 sec, (d) 33 sec, (e) 45 sec, (f) 46 sec, (g) 47 sec, and (h) 57 sec (theoretical (--) prediction of the sNLS eq.) into the experiment.

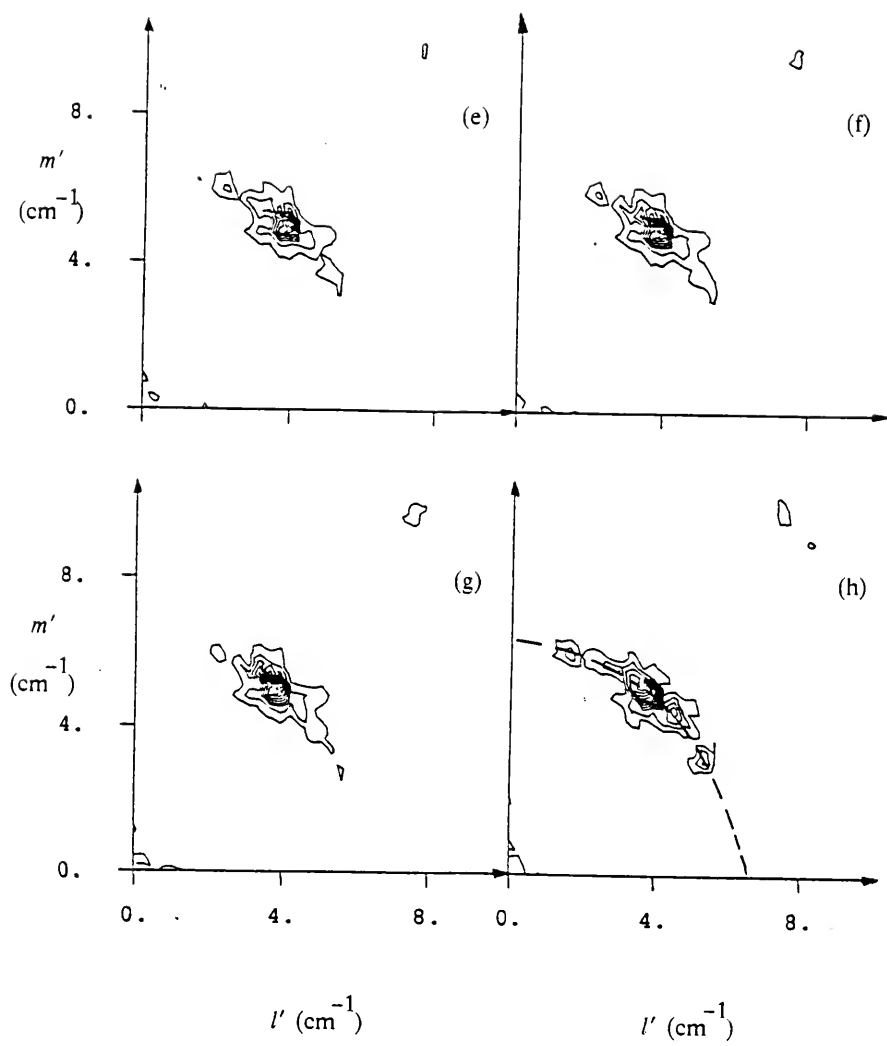


Figure 5.4--continued

Table 5.1. Summary of experiments

All experiments used the following:

Paddle immersion = 0.24 mm, Surface tension = 73 dyn/cm.

Channel width = 30.5 cm, water depth = 4.92 cm, and $y = -4.7$ cm.

Exper.	Input freq. (Hz)	$k_0 s$	x	$k_0 a$	$\dot{\mu}$	$-\dot{\chi}$ $(\frac{\text{sec}^2}{\text{cm}^5})$	$\frac{2\pi}{Q_m}$ (cm)	$\pm \dot{\theta}$ (°)	$(P _m)^{-1}$ (cm)	δ^{-1} (cm)
GC2502	25	0.13	23	0.08	0.079	0.119	31.7	2.5	333.3	11.0
GC2503	25	0.19	23	0.16	0.079	0.119	16.5	4.9	90.9	11.0
GC2504	25	0.25	23	0.18	0.079	0.119	14.2	5.6	66.7	11.0
GC1702	17	0.09	23	0.11	0.110	0.105	22.8	4.9	125.0	15.4
GC1704	17	0.18	23	0.11	0.110	0.105	22.0	5.1	111.1	15.4
GC1706	17	0.27	23	0.34	0.110	0.105	7.3	14.9	12.3	15.4
GC13601	13.6	0.04	37	0.04	0.135	0.125	56.6	2.4	500.0	19.0
GC13605	13.6	0.18	37	0.09	0.135	0.125	24.6	5.6	111.1	19.0
GC13606	13.6	0.22	37	0.14	0.135	0.125	14.9	9.2	41.7	19.0
GC9801	9.8	0.03	23	0.03						27.3
GC9802	9.8	0.05	23	0.04						27.3
GC9804	9.8	0.10	23	0.07						27.3
GC9810	9.8	0.26	23	0.26						27.3
GC0802	8	0.04	23	0.05						36.2
GC0804	8	0.08	23	0.11						36.2
GC0806	8	0.12	23	0.16						36.2

small to moderate amplitude experiments. For the interesting case of Wilton's ripples, 9.8 Hz, we present a fourth, additional experiment. The 25, 17, 9.8, and 8 Hz experiments were conducted with the imager positioned such that the first recorded gray-level was 23 cm from the wave generator (see Table 5.1). Recall that the imager axis was oriented about 45° from the primary wavevector (see figure 4.1). In the 13.6 Hz experiment, the imager was located such that the first imaged pixel used in the spatial transform was 37 cm downstream. This was done because the wavetrain extended farther downstream, evolving spatially more slowly. The wave-gauge frequency spectra were all recorded at the same location as the first gray-level used from the image (see Table 5.1). For each frequency presented, all wavenumber spectra are normalized by the largest amplitude obtained by the two-dimensional FFT of all the cases for that particular frequency. In other words, all 25 Hz experiments, for example, are contoured using the same maximum-amplitude value chosen from among the three, 25 Hz experiments.

5.2.1 The 25 Hz Wavetrain

Resonant three-wave (triad) interactions are studied in Part 2. Therein, it is shown that in the absence of "seed" waves, no distinct triad interactions occur. The 25 Hz wave is in the admissible triad regime; however, no seed waves of sufficient amplitude to initiate triad growth are present in the experiments reported in Part 1. And yet, the water surface is still spatially disordered as is shown in the three photographs of figure 5.5. Note that as wavemaker stroke is increased, the wavefield becomes increasingly more disordered. The three amplitude-frequency spectra which were computed from experiments GC2502, GC2503 and GC2504 (shown in figure 5.5) are presented in figure 5.6. The corresponding contour maps of the wavenumber spectra, and an inset perspective view of the wavenumber spectra, are presented in figures 5.7 through 5.9. As mentioned previously, note the

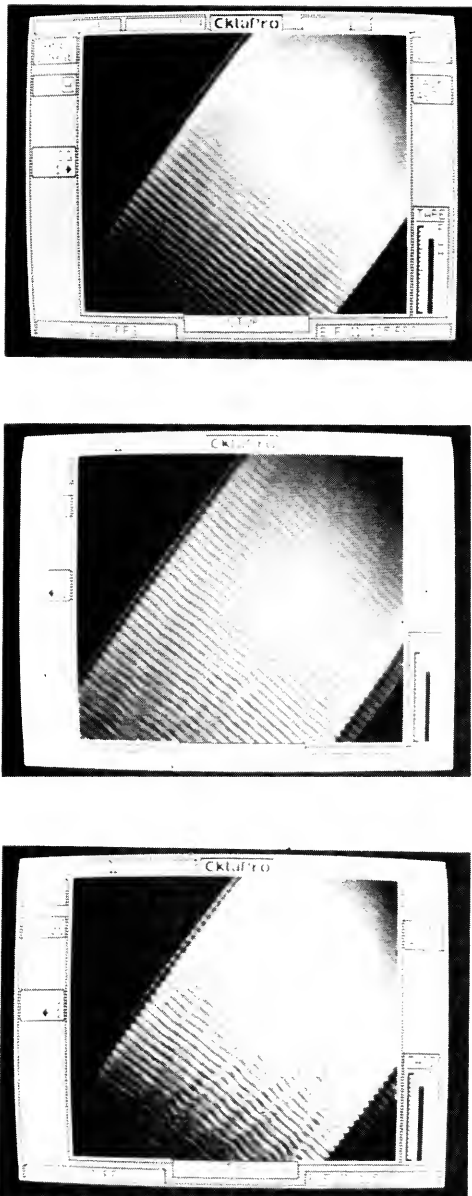


Figure 5.5 Overhead images of experiments (a) GC2502, (b) GC2503, and (c) GC2504.

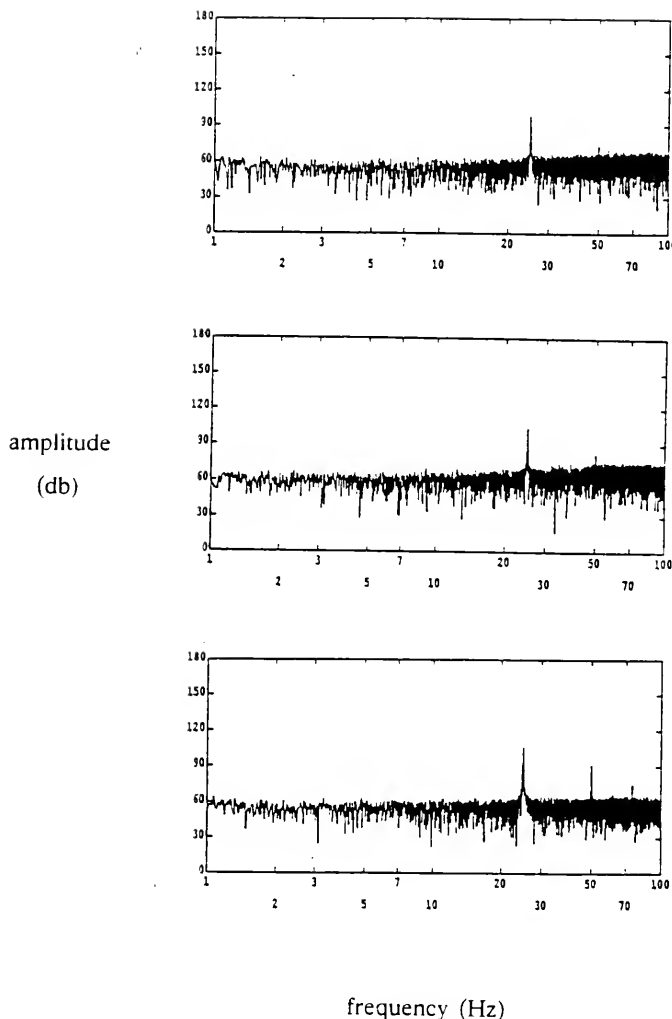


Figure 5.6 The amplitude-frequency spectra for experiments (a) GC2502, (b) GC2503, and (c) GC2504.

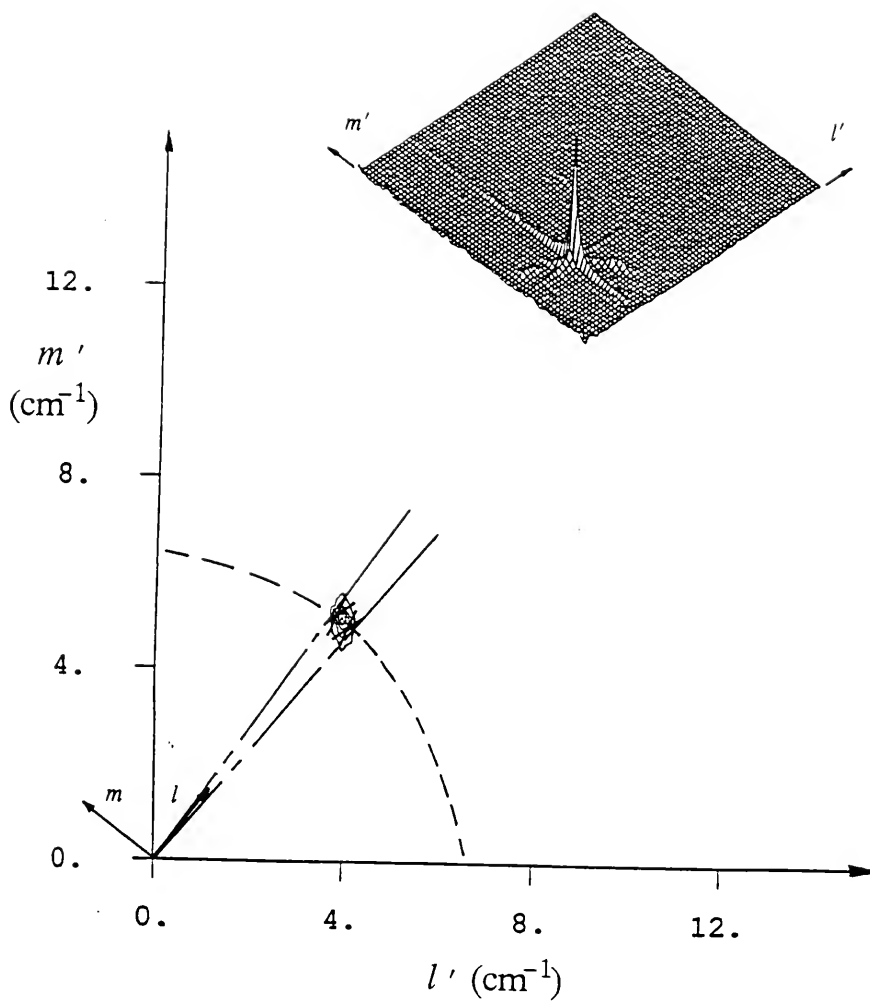


Figure 5.7 Contour map of the amplitude-wavenumber spectrum (see inset for a perspective view) for the 25 Hz wavetrain of experiment GC2502. Dispersion relation (---) of the sNLS equation; the region of spreading (— · —) and the most unstable sidebands (X) as predicted by the linear stability analysis.

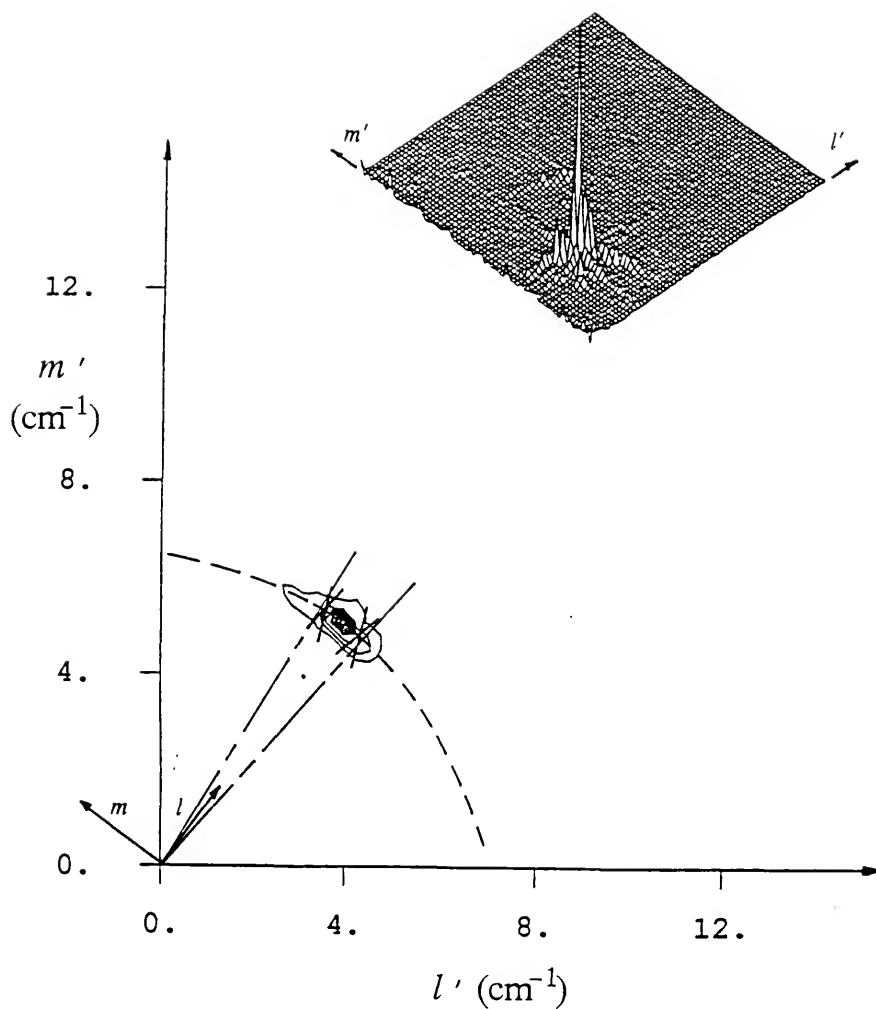


Figure 5.8 Contour map of the amplitude-wavenumber spectrum (see inset for a perspective view) for the 25 Hz wavetrain of experiment GC2503. Dispersion relation (---) of the sNLS equation; the region of spreading (—) and the most unstable sidebands (X) as predicted by the linear stability analysis.

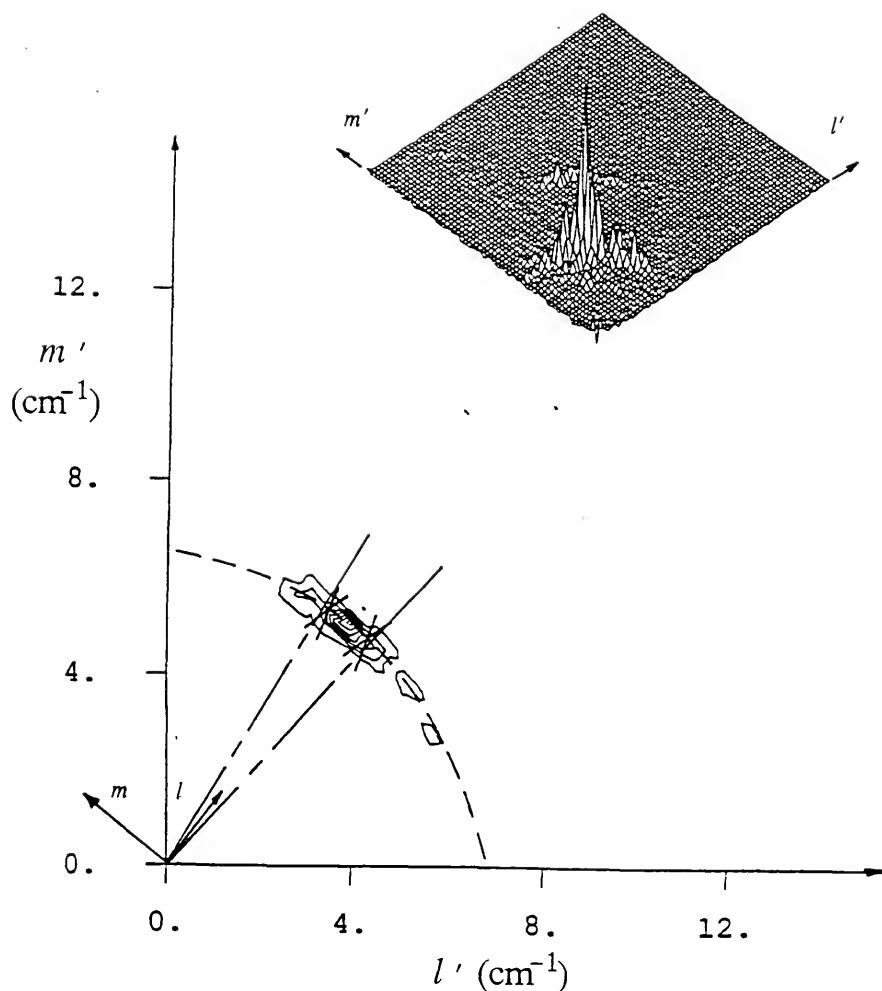


Figure 5.9 Contour map of the amplitude-wavenumber spectrum (see inset for a perspective view) for the 25 Hz wavetrain of experiment GC2504. Dispersion relation (---) of the sNLS equation; the region of spreading (—) and the most unstable sidebands (X) as predicted by the linear stability analysis.

rotation of the coordinate system. Superposed on the contour maps of the wavenumber spectra are the dispersion relations of the sNLS equation as predicted by (3.30). The maximum angle of directional spreading, as predicted by the linear stability analysis, is depicted by radial lines. Also, the most unstable sidebands, represented by X's, are shown. The values of the most unstable sidebands, along with a complete summary of the experiments, are presented in Table 5.1.

In figure 5.7, the numerical smearing of the “spike” at the input wavevector is present. In accordance with figure 4.4(c), where the angle, Ξ , is greater than 450, the smearing here is along the m' -axis. Although little directional spreading of amplitude can be seen in the contour map along the dispersion relation, it is clearly visible in the perspective view. Also visible in the inset view is the second spatial harmonic; however, an insufficient number of contours has been used to identify it, and so it is not visible in the contour map. This is consistent with the amplitude-frequency spectrum of figure 5.6(a) which has a very small, but discernible peak at 50 Hz. In all of the contour maps presented, herein, 10 contours were used based on the largest peak from each of the sets of different frequency experiments.

As mentioned previously, as spreading of wave amplitude occurs, the numerical smearing which causes the “criss-cross” appears to diminish as is seen in figures 5.8 and 5.9. As the wavemaker stroke is increased, so is the directional spreading. However, the spreading of amplitude to adjacent wavevectors is not monotonic nor smooth, but rather occurs as local extrema. In figures 5.8 and 5.9, it is seen that the most unstable sidebands are in the vicinity of the local extrema. Note that the second-harmonic wave amplitudes have also spread directionally. These “forced” waves (i.e. waves that do not satisfy the linear dispersion relation, (3.4), are termed forced, while waves that do satisfy the linear dispersion relation

are called “free”) travel with the primary waves and are thus forced to spread directionally.

An inspection of the three frequency spectra of figure 5.6, reveals that the width of the peak present at 25 Hz is increasing as wavemaker nonlinearity ($k_0 s$) is increased. This effect is due to the presence of free waves (sidebands) at slightly different wavenumber magnitudes than the input wave which are necessarily of slightly different frequencies. Recall that in figure 3.2, the dispersion relation of the sNLS equation and the circle (representing waves of constant wavenumber magnitude) are not perfectly matched, so that very slight frequency differences are expected. This phenomenon is essentially a *spatial*, Benjamin-Feir sideband. Rather than causing modulations of a one-dimensional wavetrain, the spatial instability causes directional spreading of energy of a two-dimensional wavetrain. In the first two frequency spectra of figure 5.6, two harmonics are distinct, while in the third spectrum, the third harmonic is now visible. In all of the amplitude-frequency spectra of figure 5.6, the superharmonics have significantly less amplitude than the primary wave. The amplitudes are ordered corresponding to the $O(\epsilon^n)$ at which they occur (i.e. the third harmonic has less amplitude than the second harmonic, etc.).

The directional spreading, as predicted by the dispersion relation, (3.30), of linear oscillations of the sNLS equation, have been superposed on the contour maps. Clearly, the energy spreading is occurring along these curves. The directional spreading seems to have occurred along the dispersion relation even when there were 1800 phase shifts present in the wavefield as in experiment GC2504. The most unstable sideband predictions are in reasonable agreement with local extrema along the curve. It is also evident that the maximum directional spreading as predicted by the linear analysis is somewhat underpredicting the total spreading

occurring in the experiments. In the perspective inset of figure 5.9, the directionally-spread disturbance has nearly traversed the entire quadrant; the disturbance lies along the dispersion curve. There is also spreading of the wavevectors transverse to the dispersion parabola.

5.2.2 The 17 Hz Wavetrain

The 17 Hz wavetrain lies below the 19.6 Hz parametric boundary for admissible triads, and therefore, none are expected to occur in a significant manner. In figures 5.10 (a) through (c), we present the amplitude-frequency spectra for experiments GC1702 through GC1706, respectively. As occurred with the 25 Hz experiments, the widening of the peak at 17 Hz has increased with increased wavemaker stroke. As with the previous set of experiments, this is attributed to the presence of wavevector sidebands which are free waves and thus of slightly different frequencies. Some identifiable, low-frequency energy was present in the first two spectra at between 2 Hz and 3 Hz, but for the GC1706 experiment, it has shifted to between 3 Hz and 4 Hz. These amplitude-peaks were never as large as the second harmonic. (Recall that the frequency spectra have log-scales.) In the GC1702 experiment, aside from the primary wave, only the second harmonic (34 Hz) is identifiable. Three harmonics are distinct in the GC1704 frequency spectrum, and, at least, four harmonics are discernible in figure 5.10(c).

In figures 5.11, 5.12, and 5.13, the wavenumber spectra are presented for the 17 Hz experiments. Here, the relative sizes of the second harmonics (as compared to the primary waves) were larger than in the 25 Hz experiments. The maximum amplitude peak occurs in experiment GC1704 which has a smaller wavemaker motion than experiment GC1706. Presumably, this is due to the significant amount of directional spreading occurring in the GC1706 (largest stroke) experiment. There were also more low-wavenumber amplitudes present in the 17 Hz experi-

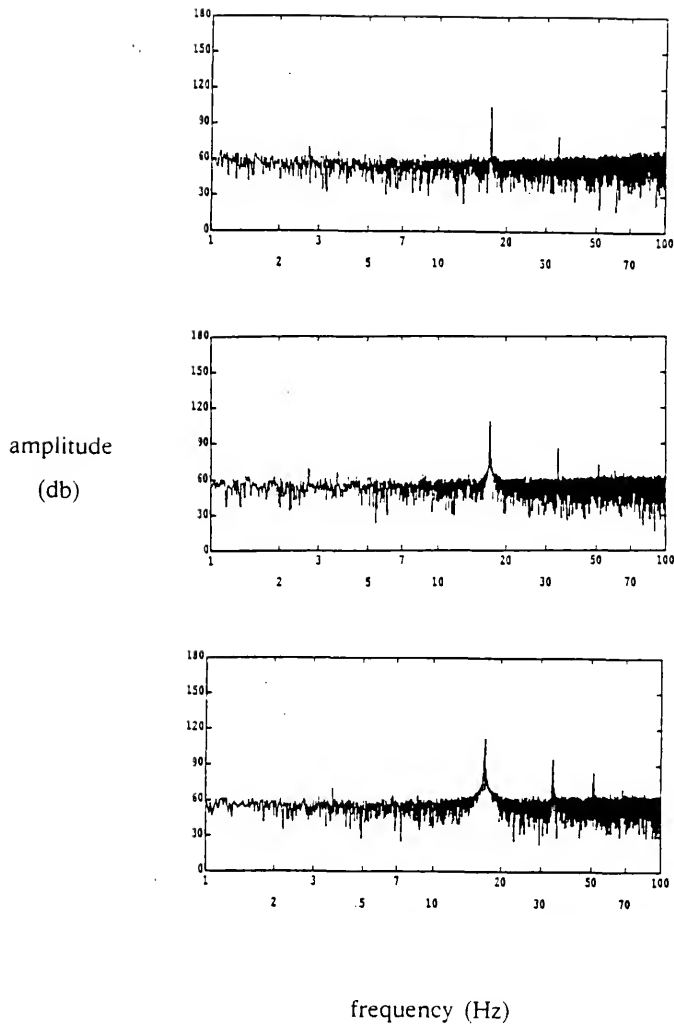


Figure 5.10 The amplitude-frequency spectra for experiments (a) GC1702, (b) GC1704, and (c) GC1706.

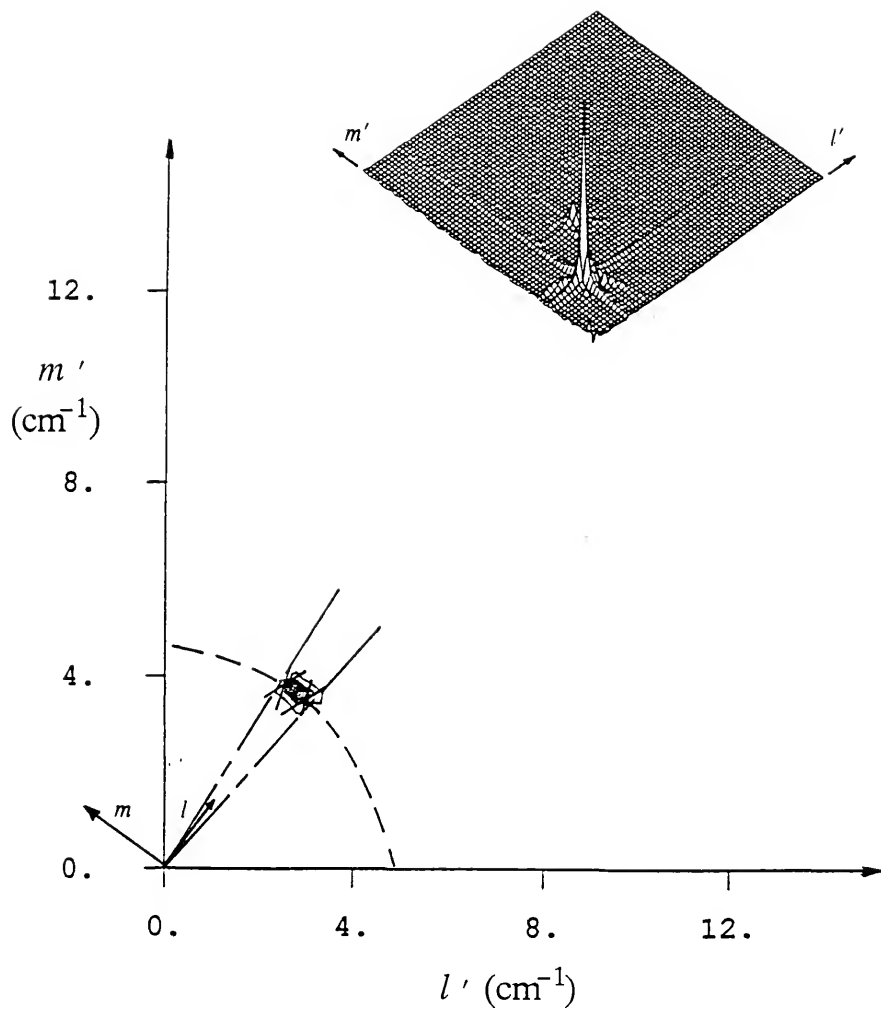


Figure 5.11 Contour map of the amplitude-wavenumber spectrum (see inset for a perspective view) for the 17 Hz wavetrain of experiment GC1702. Dispersion relation (---) of the sNLS equation; the region of spreading (— —) and the most unstable sidebands (X) as predicted by the linear stability analysis.

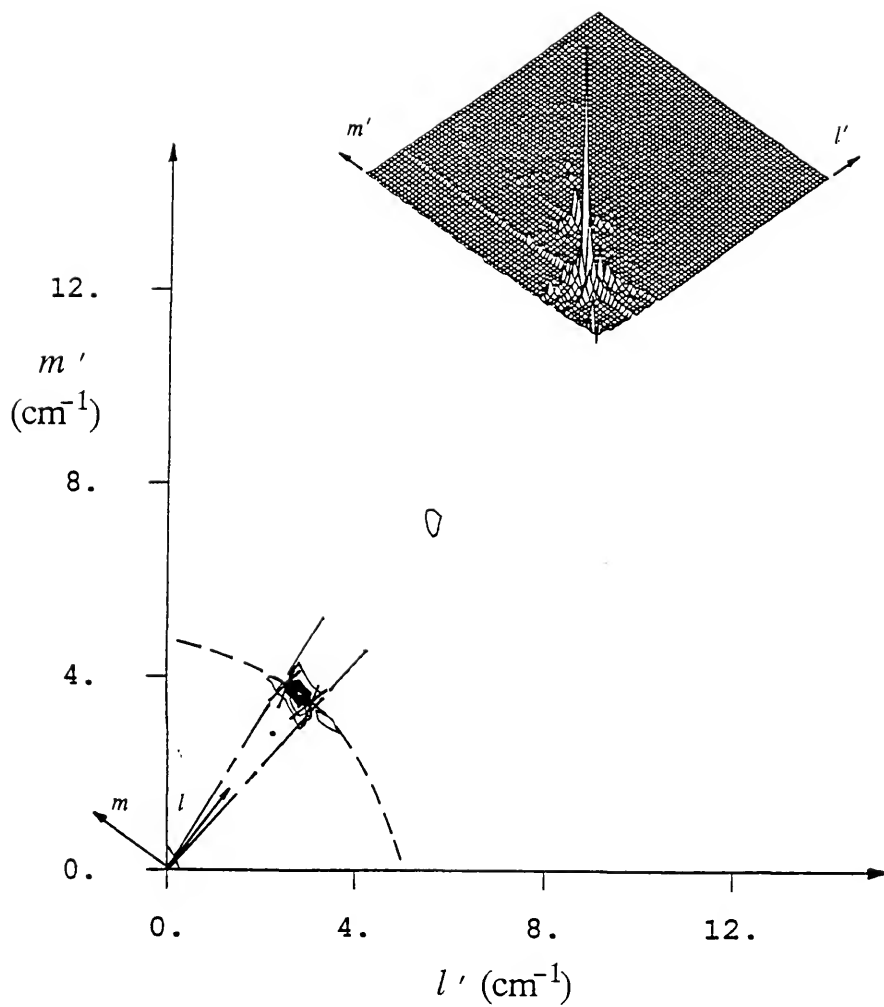


Figure 5.12 Contour map of the amplitude-wavenumber spectrum (see inset for a perspective view) for the 17 Hz wavetrain of experiment GC1704. Dispersion relation (---) of the sNLS equation; the region of spreading (— — —) and the most unstable sidebands (X) as predicted by the linear stability analysis.

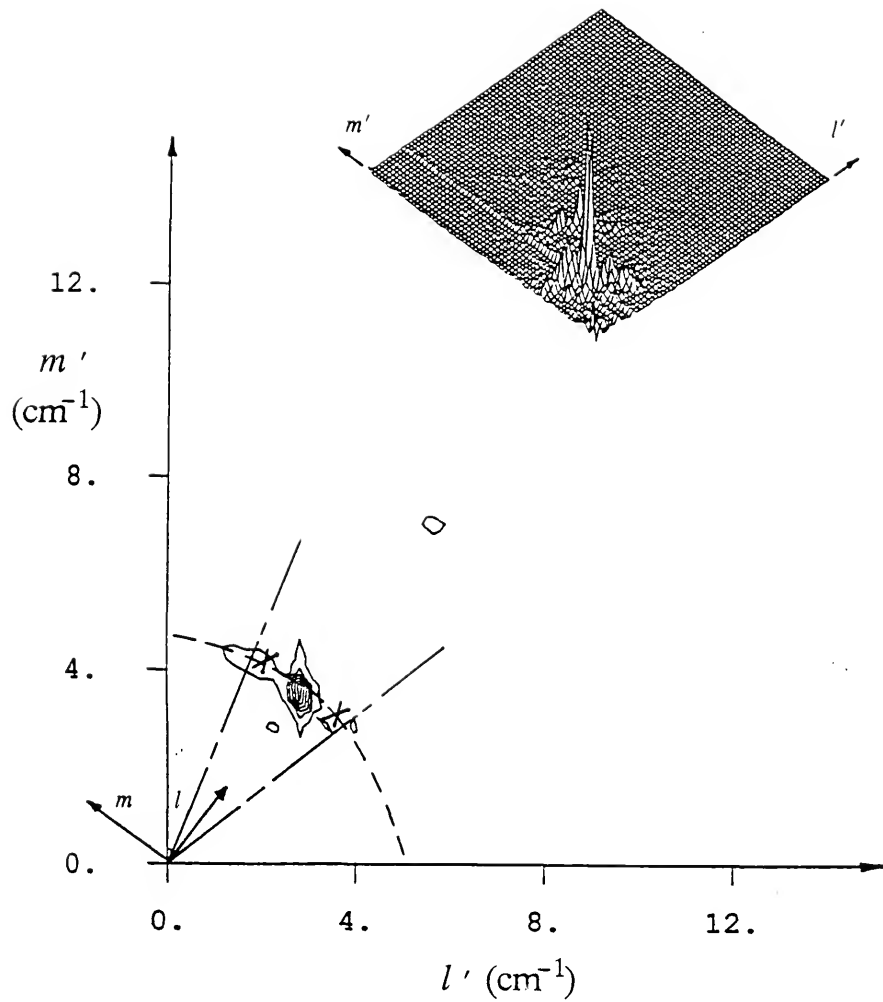


Figure 5.13 Contour map of the amplitude-wavenumber spectrum (see inset for a perspective view) for the 17 Hz wavetrain of experiment GC1706. Dispersion relation (---) of the sNLS equation; the region of spreading (— —) and the most unstable sidebands (X) as predicted by the linear stability analysis.

ments than there were in the 25 Hz experiments. Some of the low-wavenumber amplitudes were due to viscous effects as discussed in Chapter 3. Again, the amplitude-wavenumber contour maps show that the most unstable sidebands are predicted reasonably well, and, that the directional spectra spread in accord with the prediction of the sNLS equation. As with the 25 Hz experiments, these wavetrains' second harmonics were directionally spread. The numerical smearing of the large-amplitude peaks is also visible. Also, notice the asymmetry in the contour map of the wavenumber spectrum of figure 5.13. In the perspective view, it is seen that the wavenumbers, along the dispersion curve clockwise from the I -axis, are present; however, they have less amplitude than those in the counter-clockwise direction. Possibly, this is due to lighting effects.

Upon comparison of figures 5.10(c) and 5.13, we see that there are some contradictions. The local extremum shown in figure 5.13, which has a wavenumber magnitude of about $k = 3.6$ (less than the input wavevector), but has an identical direction, has a free-wave frequency of 13.3 Hz. It is not identifiable in the frequency spectrum. However, there is energy present at 3.7 Hz in the frequency spectrum which corresponds to a free-wave wavenumber of 0.54. There is no energy in the wavenumber spectrum at about 0.5. We assume that the waves appearing in either of the two measurement techniques which do not correspond to free-waves are thus forced-waves (or possibly spurious noise).

5.2.3 The 13.6 Hz Wavetrain

At approximately 13.6 Hz, the phase velocity and the group velocity of G-C waves are equal. Although this does not represent a frequency for which anything significant occurs as relates to the NLS equation (see figure 3.2), it is a unique frequency as regards ripples and so it is investigated. (Benney, 1976 investigated

the non-collinear case where phase velocity equals the projection of the group velocity in the context of resonant interaction theory.)

Experimental results for GC13601, GC13605 and GC13606 are shown in figures 5.14(a) through 5.14(c), 5.15, 5.16, and 5.17. The results are very similar to the 25 Hz and 17 Hz experiments with the exception that there is almost no identifiable second-harmonic amplitude in the frequency spectrum, nor in the wavenumber spectrum for the GC13601 experiment. In fact, this is the first perspective view of the wavenumber spectrum in which almost no directional energy spreading is present. (Experiment GC13601 had the smallest value of $k_0 s$ of the wavetrains for which the sNLS equation is valid.) For the 13.6 Hz experiments, the most unstable sidebands and the maximum spreading of the energy as predicted by the linear stability analysis are in reasonable agreement. Note that in the wavenumber perspective views of figures 5.16 and 5.17, the sidebands grow considerably. In fact, their magnitude, in figure 5.17 is about one-third that of the primary wavevector. The “criss-cross” effect is present, also. Recall that these spectra were computed from images taken 37 cm downstream as opposed to the other experiments which were recorded at 23 cm. This apparent slower spatial development is consistent with the 25 and 17 Hz cases, which we expect should occur more quickly in space (and do); and the 9.8 Hz wavetrain, which we know will occur more quickly because its evolution (resonance) occurs at second order.

5.2.4 The 9.8 Hz Wavetrain, Wilton's Ripples

As shown in figure 3.2, 9.8 Hz lies on a boundary in parameter space of the NLS equation. For frequencies greater than 9.8 Hz, the NLS equation predicts an unstable region (for sufficiently deep water). Wavetrains, with a frequency less than 9.8 Hz, and greater than about 6.4 Hz, are stable as regards the NLS equation. Wilton's ripples (a 9.8 Hz wavetrain for deep-water with a surface tension

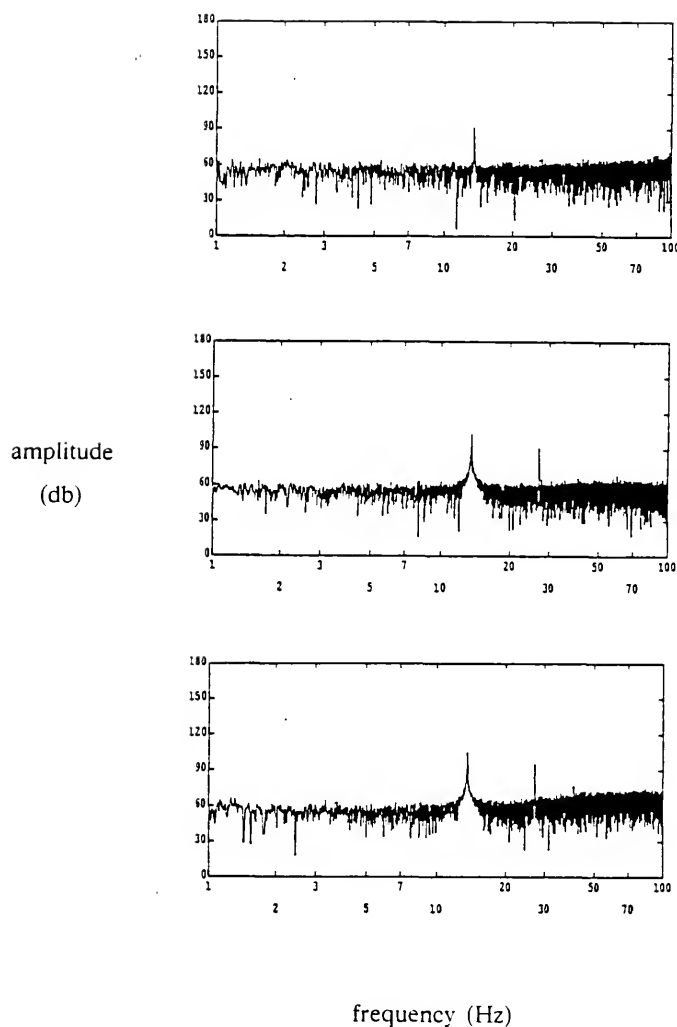


Figure 5.14 The amplitude-frequency spectra for experiments (a) GC13601, (b) GC13605, and (c) GC13606.

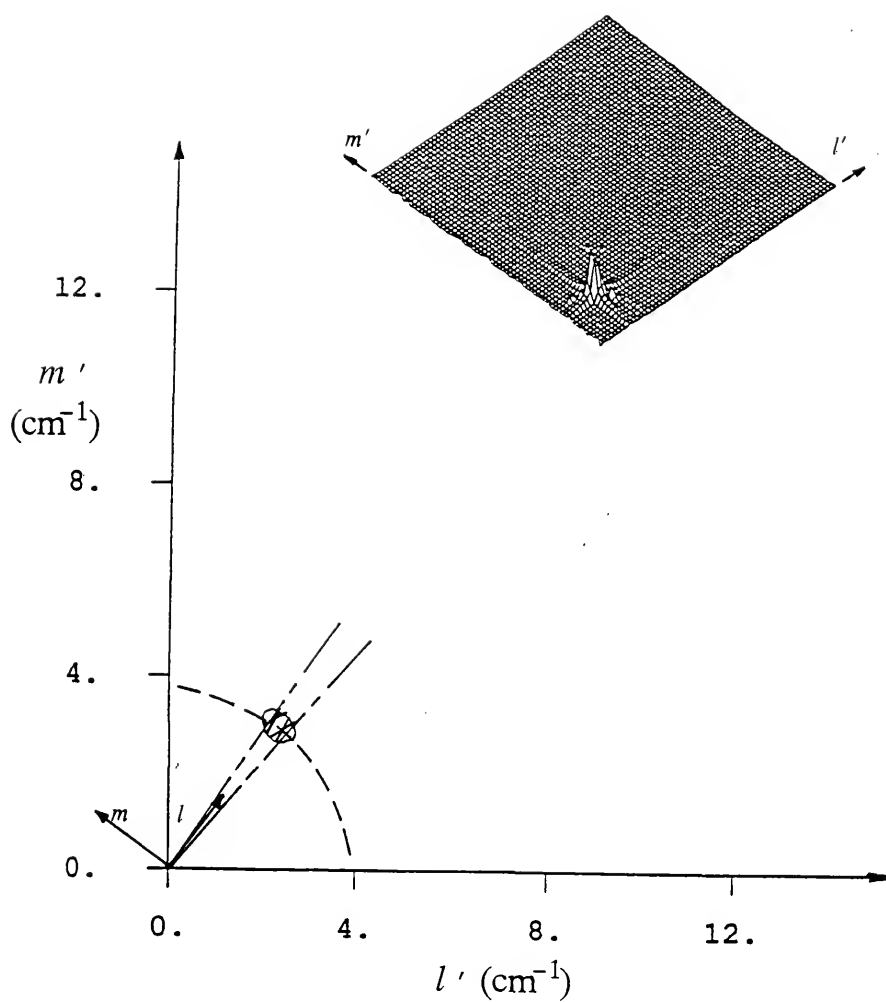


Figure 5.15 Contour map of the amplitude-wavenumber spectrum (see inset for a perspective view) for the 13.6 Hz wavetrain of experiment GC13601. Dispersion relation (---) of the sNLS equation; the region of spreading (—) and the most unstable sidebands (X) as predicted by the linear stability analysis.

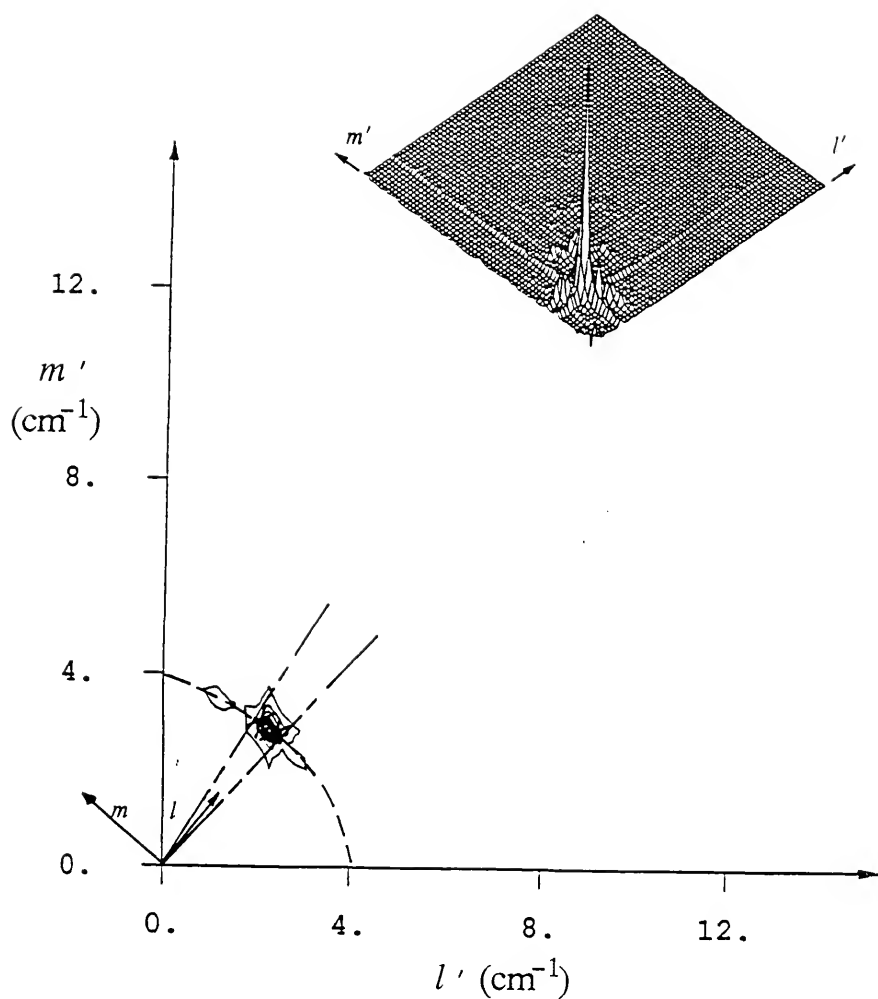


Figure 5.16 Contour map of the amplitude-wavenumber spectrum (see inset for a perspective view) for the 13.6 Hz wavetrain of experiment GC13605. Dispersion relation (---) of the sNLS equation; the region of spreading (— — —) and the most unstable sidebands (X) as predicted by the linear stability analysis.

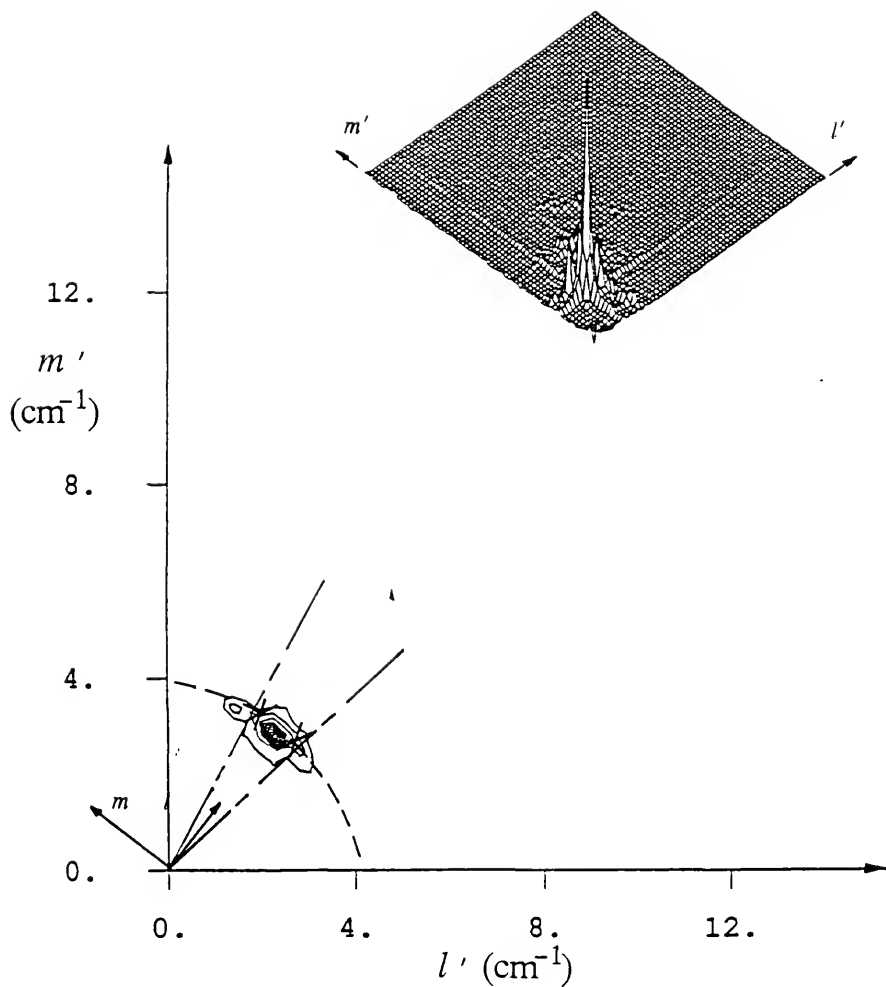


Figure 5.17 Contour map of the amplitude-wavenumber spectrum (see inset for a perspective view) for the 13.6 Hz wavetrain of experiment GC13606. Dispersion relation (---) of the sNLS equation; the region of spreading (—) and the most unstable sidebands (X) as predicted by the linear stability analysis.

coefficient of 73 dyn/cm), is a degenerate, three-wave (internal) resonance which occurs at second order. In addition, the second harmonic (19.6 Hz) represents a parametric boundary in ripple dynamics. It is the low-frequency boundary at which resonant interaction theory no longer admits triads. Therefore, Wilton's ripples are a very unstable wavetrain. The parabolic-shaped, directional spreading as predicted by the sNLS equation is no longer applicable. It is expected that second harmonic (19.6 Hz) resonance will dominate the evolution.

Four experiments were conducted for Wilton's ripples, and the amplitude-frequency spectra are presented in figure 5.18. The second harmonic was present in all of the spectra, and adjacent frequencies were also excited as the energy spread directionally. As in the previous experiments, the width of the peak at 9.8 Hz (in the frequency spectra) increased as wavemaker stroke was increased. For Wilton's ripples, this phenomenon also occurred for the 19.6 Hz second harmonic. In the GC9810 experiment shown in figure 5.18(d), at least 6 harmonics are identifiable. Also in figure 5.18(d), background waves, which were "flat" in the other spectra, are seen to have been excited, but at a significantly less energetic level.

In figures 5.19 through 5.22, we present the contour maps and perspective views of the wavenumber spectra. First, note that parabolic-shaped spreading does not occur (although significant spreading does occur in experiment GC9810). In figure 5.20, notice the magnitude of the second harmonic in the perspective view. It is already approaching the size of the input wave. This is in disagreement with the frequency spectrum for this experiment, figure 5.18(b), which shows an increase in amplitude of the second harmonic, but not to this extent. In fact, none of the frequency spectra show that the magnitude of the 19.6 Hz waves grow to the size of the 9.8 Hz waves. Remember, however, that the frequency spectra are from point measurements at 23 cm, while the spatial information covers an area about

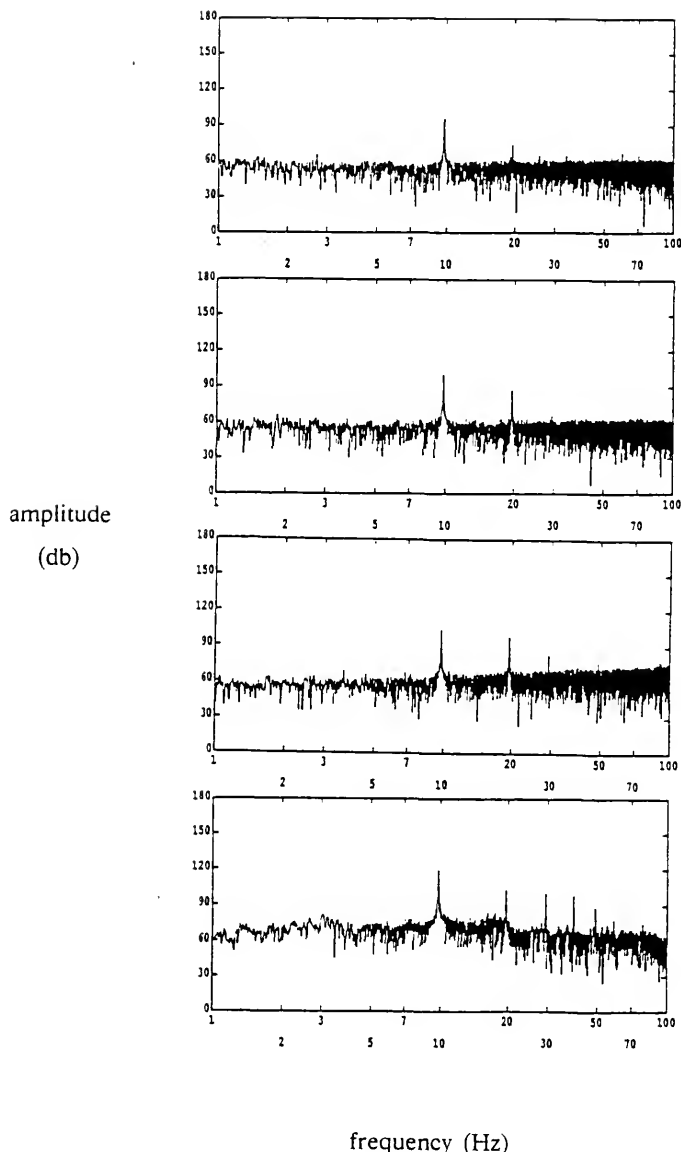


Figure 5.18 The amplitude-frequency spectra for experiments (a) GC9801, (b) GC9802, (c) GC9804, and (d) GC9810.

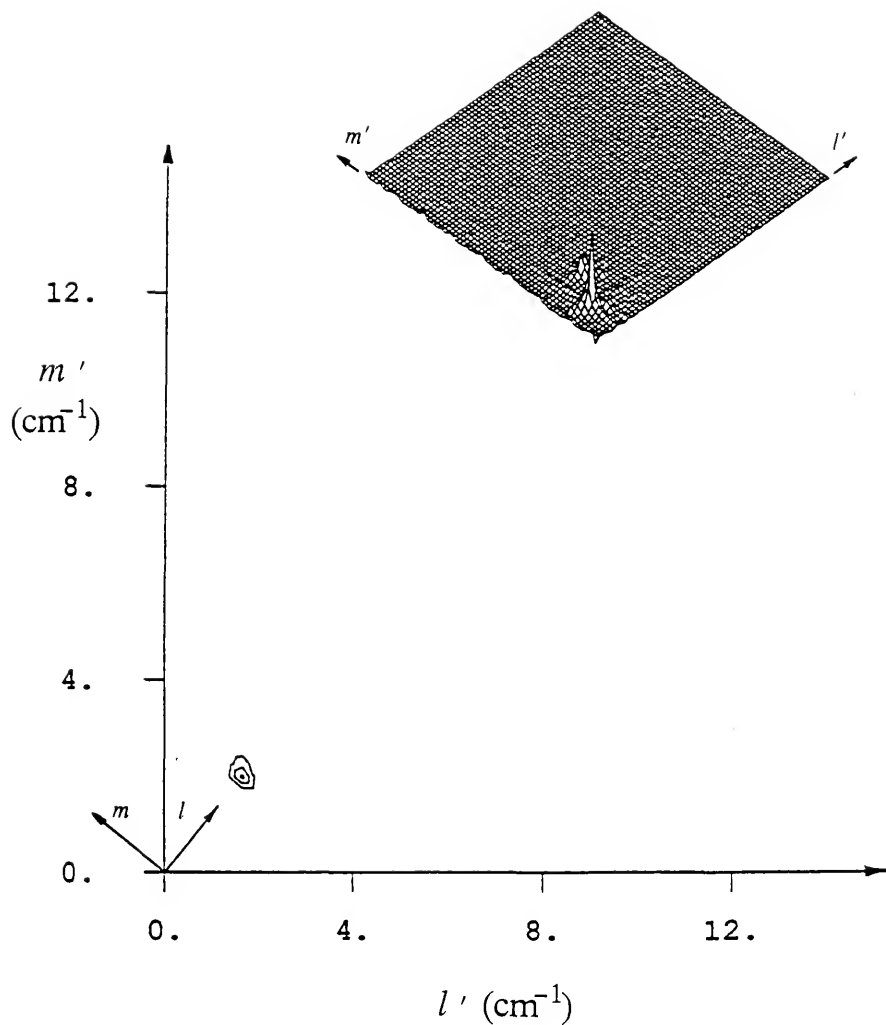


Figure 5.19 Contour map of the amplitude-wavenumber spectrum (see inset for a perspective view) for the 9.8 Hz wavetrain of experiment GC9801.

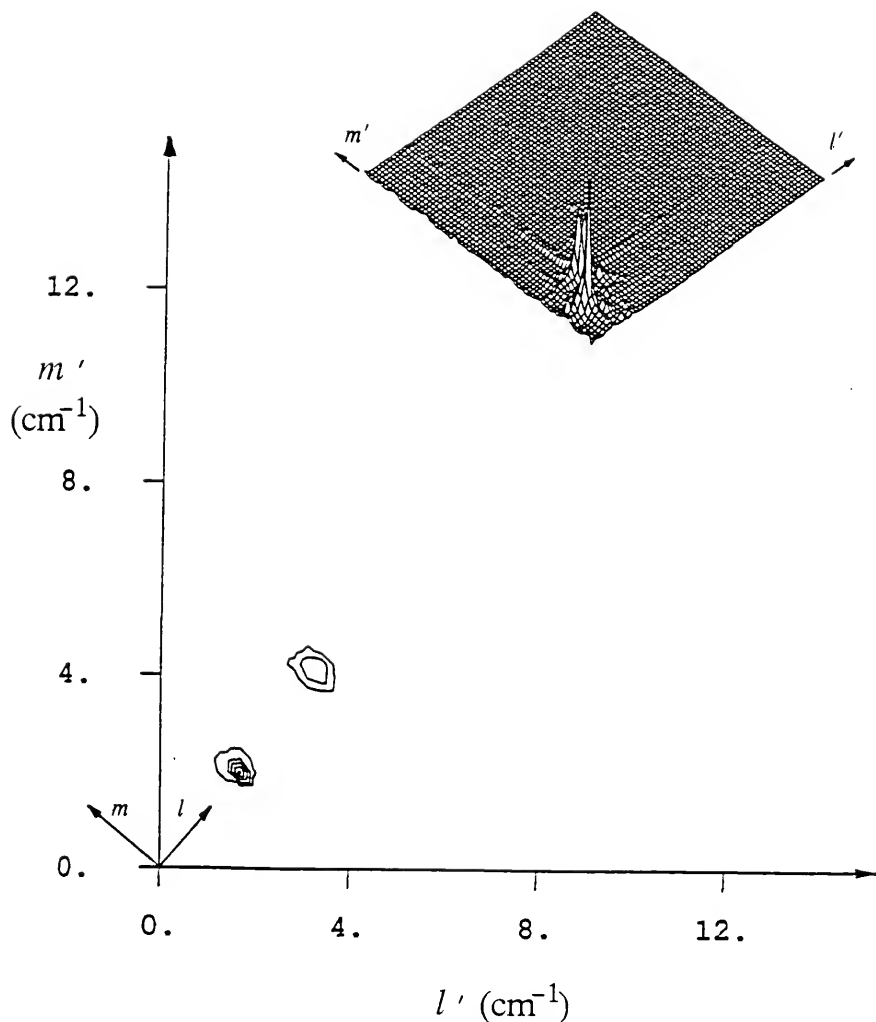


Figure 5.20 Contour map of the amplitude-wavenumber spectrum (see inset for a perspective view) for the 9.8 Hz wavetrain of experiment GC9802.

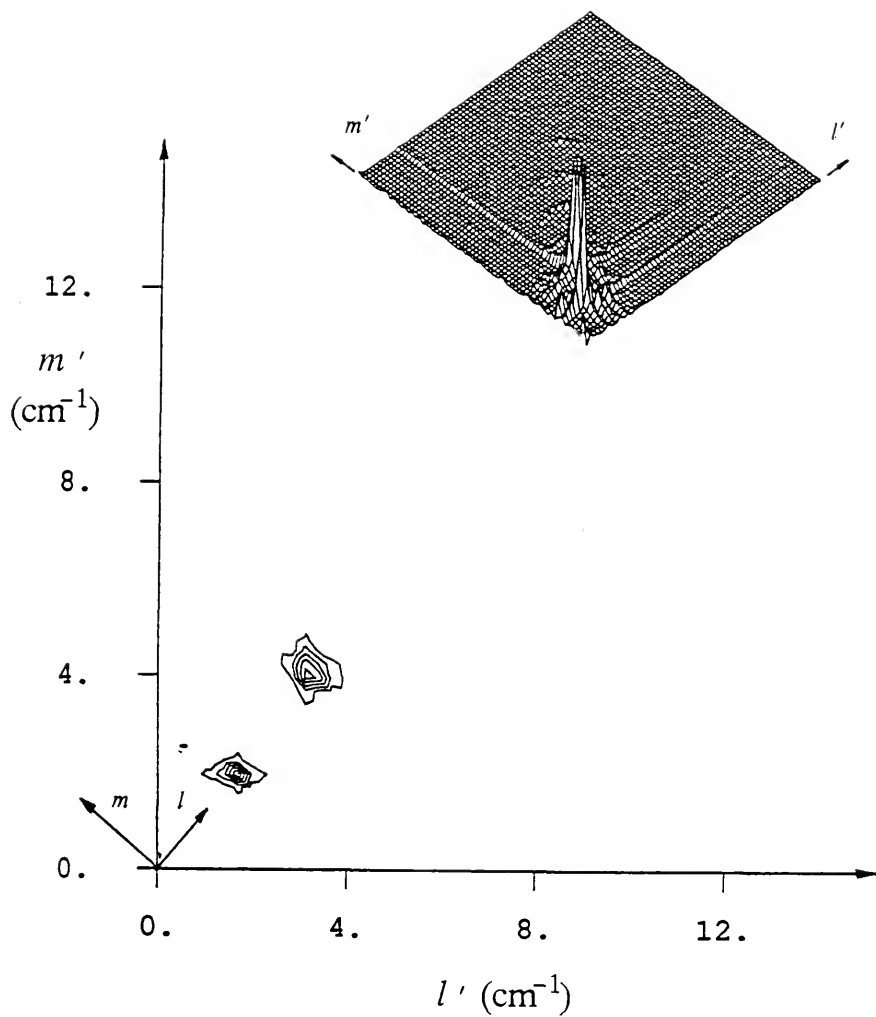


Figure 5.21 Contour map of the amplitude-wavenumber spectrum (see inset for a perspective view) for the 9.8 Hz wavetrain of experiment GC9804.

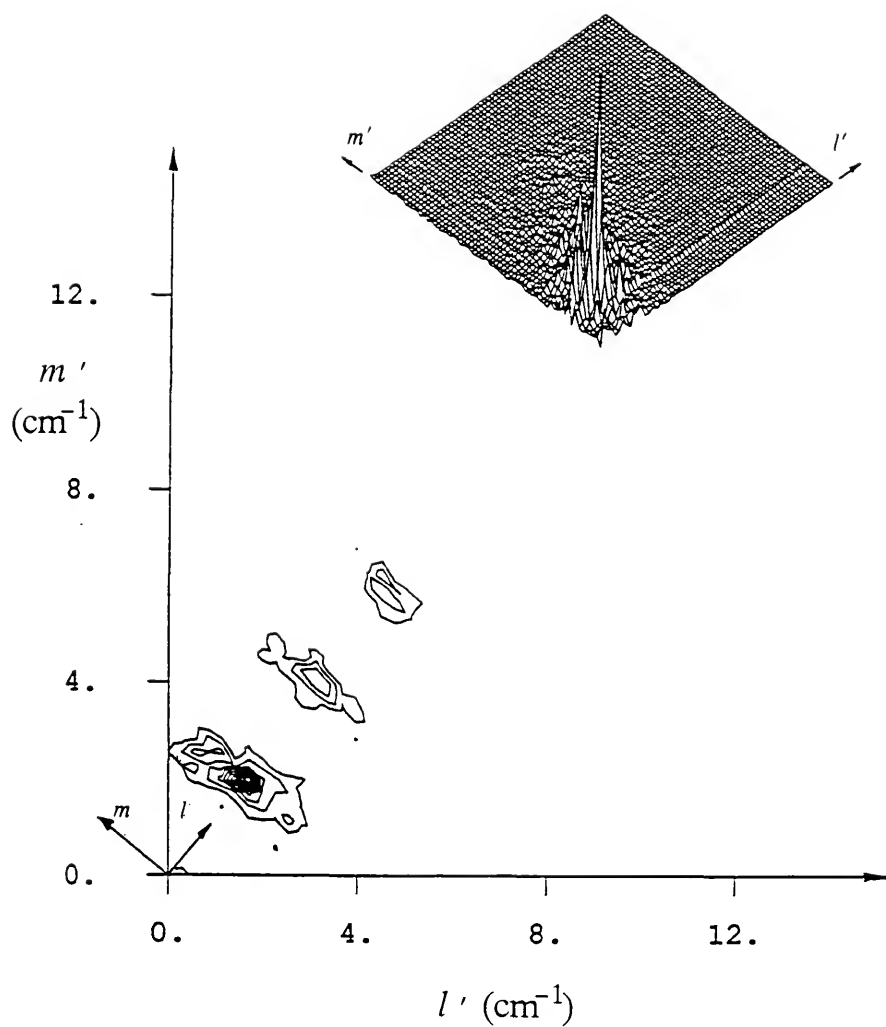


Figure 5.22 Contour map of the amplitude-wavenumber spectrum (see inset for a perspective view) for the 9.8 Hz wavetrain of experiment GC9810.

22 cm by 22 cm beginning at 23 cm downstream. Thus, the frequency spectra do not contain any spatial information, and the wavenumber spectra contain no temporal information. So, it is not surprising that they do not agree in this respect, especially since these wavetrains are evolving in space (and more slowly in time). In figure 5.21, the first and second harmonics are shown to be of comparable magnitude by the wavenumber spectrum. Numerical smearing is present, again, as is seen in figures 5.20 through 5.22. In figure 5.22, the directional spreading has occurred for the first three harmonics along an apparently, almost straight line (perpendicular to the input wavevector).

5.2.5 The 8 Hz Wavetrain

According to the NLS equation, an input frequency of 8 Hz is a stable wavetrain. Note that for clean, deep water, frequencies less than 9.8 Hz through 6.4 Hz are stable. Referring again to figure 3.2, along curve C_1 , λ changes sign, and upon crossing this curve toward lower wavenumbers, the region is again Benjamin-Feir unstable. In figure 5.23, the amplitude-frequency spectra are presented for experiments GC0802, GC0804, and GC0806. In figures 5.23a and 5.23b, the second harmonic and the second, third, and fourth harmonics have distinct, ordered peak-magnitudes, respectively. However, in figure 5.23(c), the magnitude of the third harmonic has surpassed the magnitude of the second harmonic!

In figures 5.24 through 5.26, we present the wavenumber spectra for these three experiments. Notice the presence of a significant “criss-cross” effect reminiscent of the numerical smearing of figure 4.4(d). The 8 Hz wavevectors in figures 5.24 and 5.25 show no other directional spreading of energy in agreement with the theory. However, in figure 5.26, we see the dramatic emergence of a directionally spread third harmonic whose central peak is about one-half the peak of the primary wave. In fact, the spreading is predicted fairly well by the dispersion relation

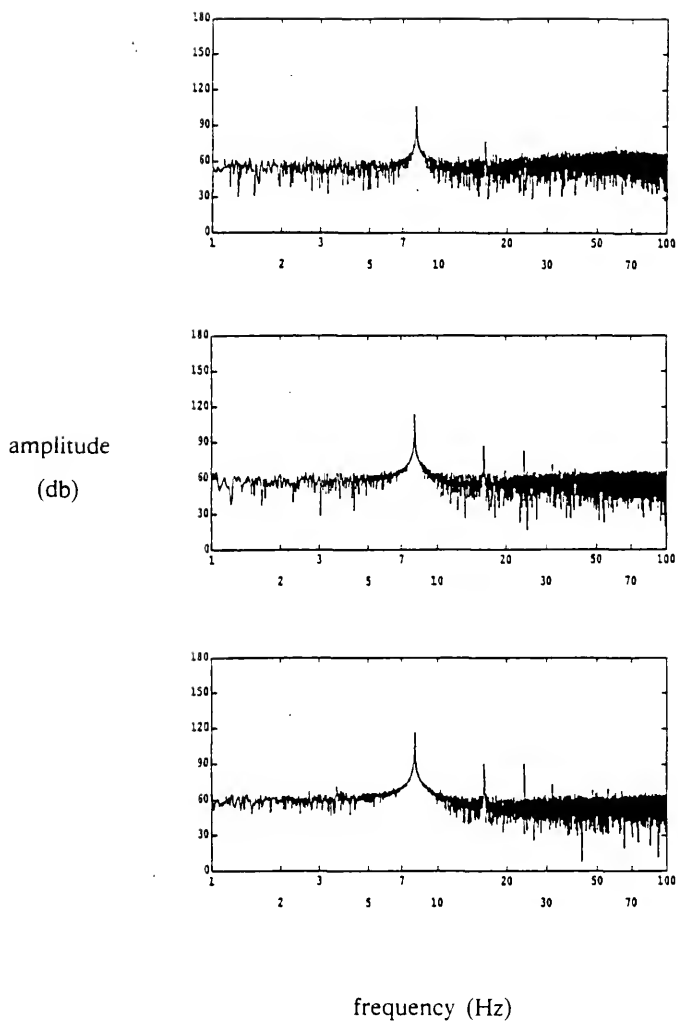


Figure 5.23 The amplitude-frequency spectra for experiments (a) GC0802, (b) GC0804, and (c) GC0806.

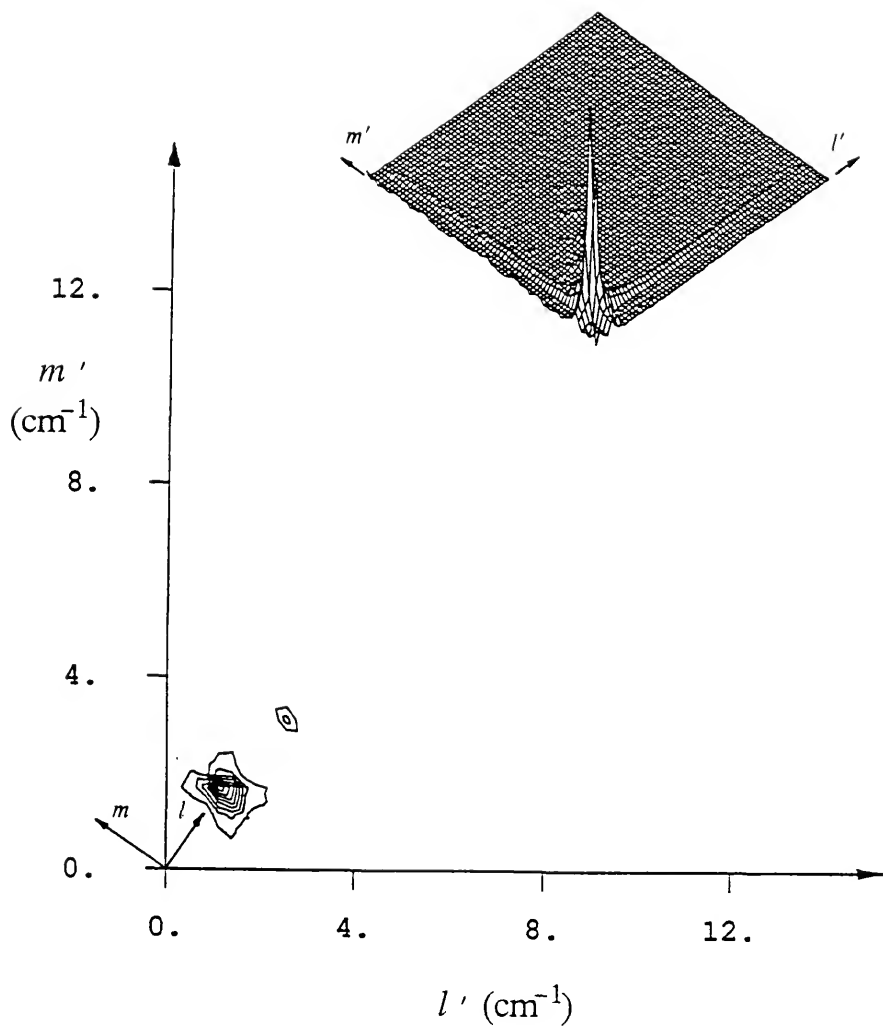


Figure 5.24 Contour map of the amplitude-wavenumber spectrum (see inset for perspective view) for the 8 Hz wavetrain of experiment GC0802.

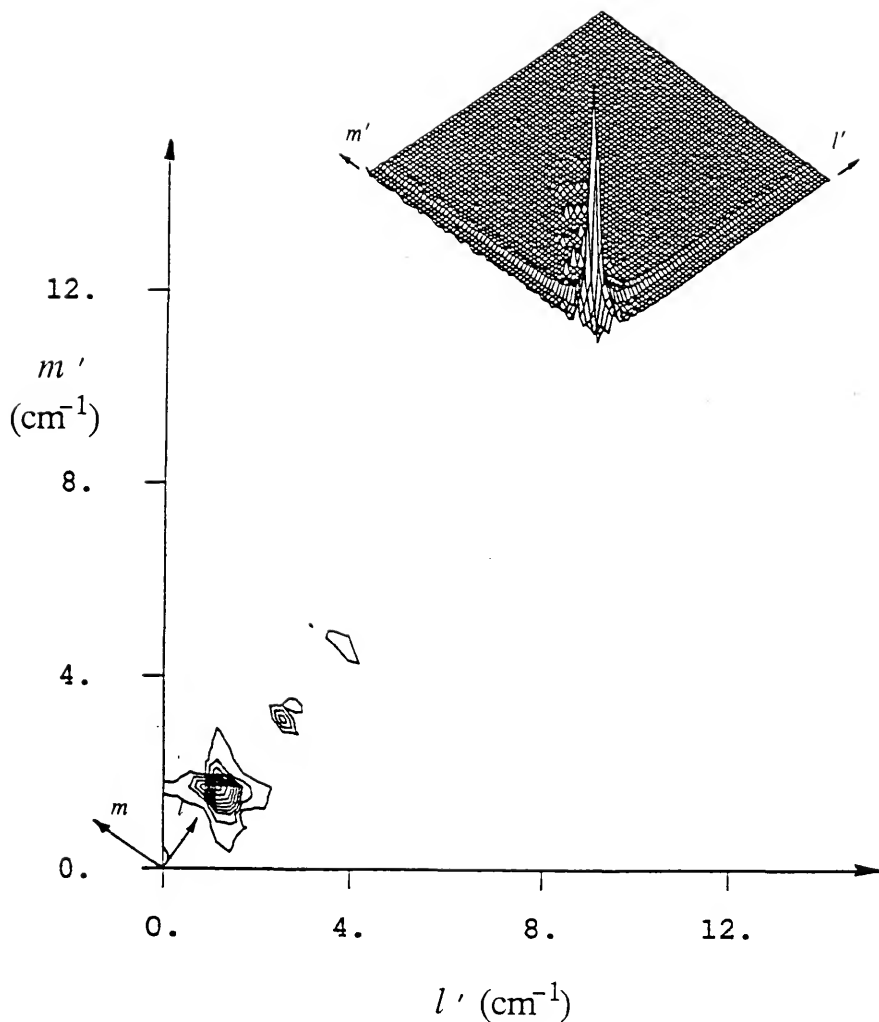


Figure 5.25 Contour map of the amplitude-wavenumber spectrum (see inset for a perspective view) for the 8 Hz wavetrain of experiment GC0804.

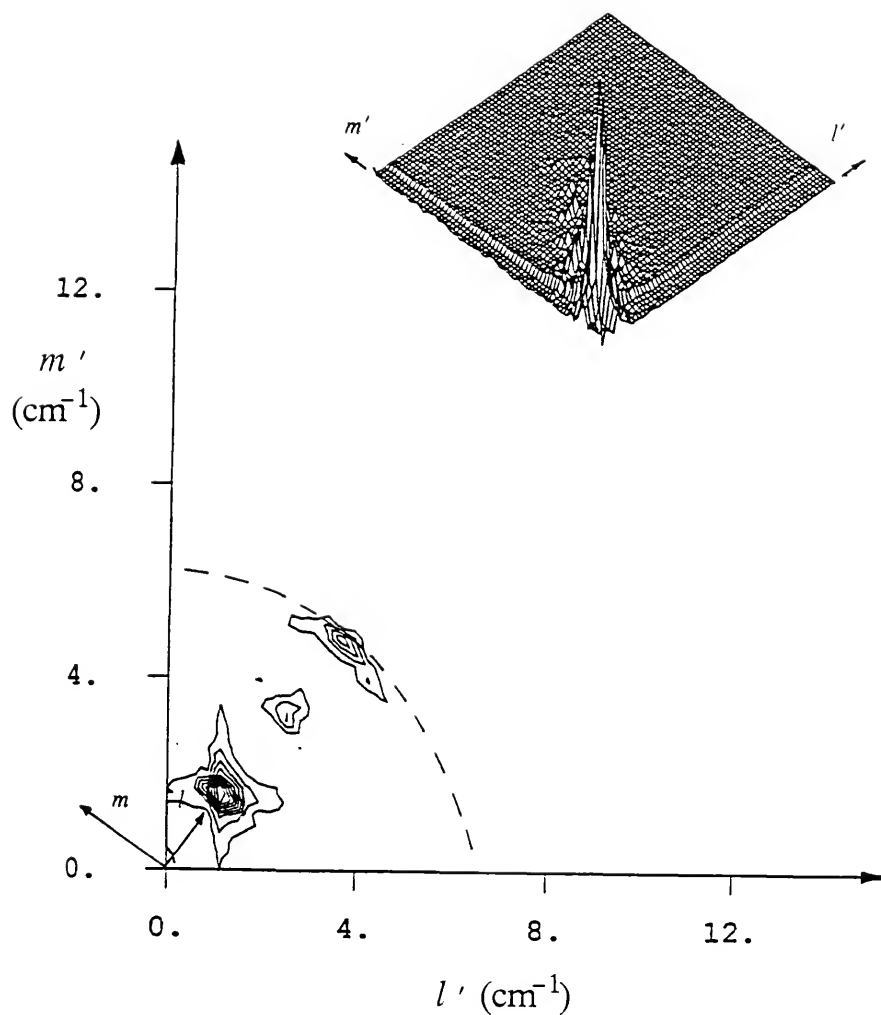


Figure 5.26 Contour map of the amplitude-wavenumber spectrum (see inset for a perspective view) for the 8 Hz wavetrain of experiment GC0806. Theoretical (---) prediction of the sNLS equation for a 24 Hz wavetrain.

of the sNLS equation which has been superposed on the figure. It appears that the 24 Hz (third harmonic) is resonating with the primary wave by third-harmonic resonance. Thus, the explanation of the large third harmonic frequency peak in figure 5.23c. In fact, the photograph, shown in figure 4.3, clearly shows the presence of the third harmonic. Theoretically, third-harmonic resonance should occur for an 8.38 Hz wavetrain and a 25.14 Hz wavetrain. Apparently, this is a case of detuned, third-harmonic resonance. McGoldrick (1972) presented results which show that the ratio of an 8 Hz response to an 8.55 Hz response (his peak response) is about 8%. His results give a ratio of the 8 Hz response to the 8.38 Hz response (the theoretical third-harmonic resonance) of about 13%. Therefore, it is somewhat surprising that the magnitude of the 24 Hz wavetrain grew so large.

CHAPTER 6

SUMMARY AND CONCLUSIONS OF PART 1

In the preceding sections, we have investigated a previously unexplored instability of G-C waves. It represents a plausible model of the instabilities of ripple wavetrains generated mechanically in a wide, laboratory channel. The stationary, NLS model predicts the directional spreading of amplitude reasonably well. Also, it provides a mechanism by which energy is available at various angles, so that non-collinear triad and quartet resonances can occur.

Three sets of wavetrains with frequencies of 25, 17 and 13.6 Hz, which are in the sNLS unstable regime, are shown to display this instability. Using wavenumber spectra, all of these wavetrains are shown to directionally spread their amplitude along a dispersion curve as predicted by assuming linear modulations of the sNLS equation. Energy appears in the vicinity of the most unstable sidebands. As non-linearity in the wavefield increases, this spreading of energy increases.

Wilton's ripples (9.8 Hz for clean, deep water), for which a degenerate, three-wave (internal) resonance exists, resonates with its second harmonic and both spread their energy directionally; however, the transfer of energy is along a path perpendicular to the input wavevector in the wavenumber plane. Experiments with 8 Hz wavetrains which are theoretically stable according to the NLS equation, are shown to remain stable until third harmonic resonance occurs. Then, the third harmonic, which is now a free wave, exhibits the sNLS instability and spreads its amplitude accordingly. One possible explanation of why the 8 and 24 Hz waves

resonate when the theory predicts 8.38 Hz and 25.14 Hz is that of detuned resonance.

As mentioned earlier, one very important phenomenon neglected entirely by the derivation of the NLS equation is viscosity. Herein, viscous effects preclude any attempt to see whether recurrence is present in our experiments. Also, viscous effects hamper analytic comparisons between experiment and theory.

Further experiments are required in which spatial disorder is investigated in the presence of triads (forced to occur by wave seeding). Other related experiments include modulating the wavemaker in time (problems arise because of the difference waves generated by the wavemaker, especially if two waves are superposed to drive the wavemaker and thus the modulation) and the case in which finite-water depth effects are more significant (i.e. mean, long-wave motion is significant).

Finally, quantitative measurements of the phenomenon for use in comparison to numerical simulations with linear viscosity included, would be useful. However, before quantitative measurements can be made, two improvements would be beneficial. First, the wave gauge probe should be replaced by a nonintrusive, laser gauge (this is currently being developed). Second, a better understanding of the lighting used to remotely sense the wavefield, along with a calibration of the entire method of obtaining the wavenumber spectrum, is required.

CHAPTER 7

INTRODUCTION TO THREE-WAVE RESONANCE: PART 2

(Chapters 7 through 14 are essentially the research paper by Hammack, Perlin, and Henderson (to appear, 1989). This material was prepared prior to the installation of the high-speed imaging system used in the study reported in Chapters 2 through 6.)

Waves for which both gravitation and surface tension are important are ubiquitous on the ocean surface. These gravity-capillary waves (or simply "ripples") have typical frequencies in the range of approximately 5-50 Hz and lengths of approximately 50-5 mm. Relative to longer gravity-induced waves, ripples have received little attention in oceanography. However, recent interest in remote sensing of the sea surface with satellite-based radar has focused new attention on ripples. Ripple wavelengths are comparable to those of high-frequency radar waves, causing them to play a major role in the backscatter of radar waves by the ocean surface. It is somewhat paradoxical that oceanographic measurements on global scales is impacted so fundamentally by surface waves with the smallest of scales.

Ripple dynamics exhibit a variety of interesting phenomena that are generic to many nonlinear dynamical systems. One-dimensional periodic wavetrains are fraught with instabilities which occur quickly when ripples with sensible amplitudes are generated mechanically in a laboratory channel. The one-dimensional wavetrains evolve rapidly into two-dimensional surface patterns which can appear very irregular. (Herein, we refer to waves as one- or two-dimensional according to

whether their surface patterns are one- or two-dimensional. Their corresponding velocity fields are one dimension higher.) In Part 1, we investigated one of these instabilities which had been unexplored previously. These instabilities are examined, herein, experimentally and analytically from the point of view of resonant interaction theory (RIT). Theoretical results indicate that ripple wavetrains with frequencies greater than 19.6 Hz (on a perfectly clean surface) can excite resonant triad interactions; other than the spatial instability discussed in Part 1, quartic resonances are the first indicated for wavetrains with frequencies less than 19.6 Hz. Experiments are presented for wavetrains in the resonant-triad regime since these data are more definitive and analytical results are more readily available. These wavetrains are generated with and without background perturbations, which include smaller waves with distinct frequencies and smaller waves with a broad band of frequencies (random waves). The major conclusions from these experiments are as follows. First, we find that a selection mechanism exists which causes certain triads from a possible continuum to dominate the evolution of a ripple wavetrain. Second, we show that this selection results from a "seeding" of low-frequency wave(s) in the triad continuum by difference interactions between the generated wavetrain and high-frequency perturbations. These perturbations must have distinct frequencies; their amplitudes may be as small as $\frac{1}{250}$ that of the generated wave. Although a theorem by Hasselmann (1967) is not violated, the existence of this selection mechanism is contrary to expectations because the difference interactions occur at higher-order than the triad interactions, and yet, they determine the evolution of the wavefield. Third, we demonstrate a cycling of wave energy among the excited members of a wave triad during their spatial evolution. (Indeed, this is the primary mechanism we use to distinguish resonant from non-resonant interactions.) Finally, when a ripple wavetrain is generated along with a wide spectrum of random-wave perturbations, there is no selection and the entire

continuum of admissible triads is excited in a manner consistent with the form of the interaction coefficients for a single triad.

An outline of the remainder of Part 2 is as follows. In Chapter 8 we present a general summary of RIT, followed in Chapter 9 with its specific application to ripples for resonant triad interactions. In Chapter 10 a brief description of the laboratory facilities is presented. Previous experimental results on triad selection are reviewed in Chapter 11. In Chapter 12 this selection process is explained and the previous experiments are reinterpreted. Finally, in Chapter 13 we demonstrate the evolution of a ripple wavetrain in the presence of white noise.

CHAPTER 8

RESONANT INTERACTION THEORY

The fundamental notion of RIT was formulated by Phillips (1960) for gravity waves on deep water. Benney (1962) *inter alios* realized the general nature of its application to dynamical systems. The basic idea is that the effects of weak nonlinearity may be dominated by certain wave-wave interactions which satisfy “resonance” conditions. A general outline of RIT is as follows (also, see Segur, 1984). Consider a nonlinear energy-conserving dynamical system which we represent by

$$N(\phi) = 0. \quad (8.1)$$

where N is a nonlinear operator, $\phi(\mathbf{x}, t)$ is a solution of (8.1), $\mathbf{x} = (x, y, z)$ is a position vector and t is time. Suppose $\phi = 0$ is an equilibrium solution of (8.1) that is neutrally stable; then infinitesimal deformations from this equilibrium state are found by linearizing (8.1) to find

$$L(\phi_1) = 0. \quad (8.2)$$

We then seek normal mode solutions to the linear operator L of (8.2), and, if L has constant coefficients, this amounts to seeking solutions with the form:

$$\phi_1 = \exp[i(\mathbf{k} \cdot \mathbf{x} - \omega t + \alpha)] \quad (8.3)$$

where \mathbf{k} is a wavevector, ω is the wave frequency, and α is an arbitrary and constant phase angle. Substituting (8.3) into (8.2) yields a dispersion relation for

the linear problem:

$$\omega = W(\mathbf{k}). \quad (8.4)$$

We require that ω exists in the sense that for fixed \mathbf{k} there is a countable set of possible values for ω and that $W(\mathbf{k})$ is real-valued for real-valued \mathbf{k} . Now return to (8.1) and seek small-but-finite deformations from the equilibrium state by means of a formal power series:

$$\phi(\mathbf{x}, t; \epsilon) = \sum_{n=1}^{\infty} \epsilon^n \phi_n(\mathbf{x}, t) \quad 0 < \epsilon \ll 1. \quad (8.5)$$

At leading order in ϵ , ϕ_1 of (8.5) satisfies (8.2), so ϕ_1 can be represented by a superposition of M linear waves, i.e.

$$\phi_1 = \sum_{m=1}^M (A_m e^{i\theta_m} + A_m^* e^{-i\theta_m}) \quad (8.6a)$$

where A_m is the complex wave amplitude, A_m^* is its complex conjugate, and

$$\theta_m = \mathbf{k}_m \cdot \mathbf{x} - \omega_m t. \quad (8.6b)$$

The first nonlinear effects appear at order ϵ^2 where

$$L(\phi_2) = Q(\phi_1). \quad (8.7)$$

and Q is a quadratic operator. Substituting (8.6) into Q produces terms with the form:

$$A_1 A_1^* + A_1^2 e^{i2\theta_1} + A_1^* e^{-i2\theta_1} + A_1 A_2 e^{i(\theta_1+\theta_2)} + A_1 A_2^* e^{i(\theta_1-\theta_2)} + \dots \quad (8.8)$$

on the right-hand side (RHS) of (8.7). The first three terms in (8.8) correspond to self-interactions of wave $m=1$; the first term represents a “mean” flow for ϕ_2 while

the second and third terms correspond to its second harmonic (first superharmonic). The other two terms shown in (8.8), and their complex conjugates, correspond to sum and difference waves between waves $m=1$ and $m=2$. (There are analogous terms for all of the M waves in (8.6).) Supposing these quadratic interactions do not vanish identically, we can examine the terms of (8.8) to see if any of the sum and difference waves also satisfy the dispersion relation of (8.4), i.e. does

$$\theta_1 \pm \theta_2 = (\mathbf{k}_1 \pm \mathbf{k}_2) \cdot \mathbf{x} - (\omega_1 \pm \omega_2)t = \pm \mathbf{k}_3 \cdot \mathbf{x} - (\pm \omega_3)t = \theta_3 ? \quad (8.9)$$

If so, then these waves will lead to secular terms (linear growth) for ϕ_2 , and the “three waves” of (8.9) are said to form a “resonant” triad. Eventually the resonant terms will dominate nonresonant terms due to their secular growth; thus the nonresonant terms are neglected in further considerations of RIT. For water waves $W(\mathbf{k})=W(-\mathbf{k})$, so that without loss of generality we can write the kinematic resonant conditions of (8.9) for a resonant triad as

$$\mathbf{k}_1 = \mathbf{k}_2 \pm \mathbf{k}_3 \quad (8.10a)$$

$$\omega_1 = \omega_2 \pm \omega_3. \quad (8.10b)$$

The existence of triad resonances depends on the specific dynamical system (dispersion relation) being considered. If there are no terms on the RHS of (8.7) which satisfy the resonance conditions of (8.10), then we can proceed to order ϵ^3 where cubic interactions are encountered. Here, resonant quartets occur when the kinematic conditions:

$$\mathbf{k}_1 \pm \mathbf{k}_2 = \mathbf{k}_3 \pm \mathbf{k}_4 \quad (8.11a)$$

$$\omega_1 \pm \omega_2 = \omega_3 \pm \omega_4 \quad (8.11b)$$

are satisfied. Unlike triad resonances, quartic resonances are always possible for

the dynamical systems considered here. For example, a rhombus quartet always exists in which $\omega_1 = \omega_2 = \omega_3 = \omega_4$ and $|\mathbf{k}_1| = |\mathbf{k}_2| = |\mathbf{k}_3| = |\mathbf{k}_4|$. These procedures can be continued to higher-order to find analogous conditions for resonances at every order in ϵ ; though one seldom goes beyond quartic resonances.

When resonance occurs, a separate analysis is required to follow wave evolution since the secular terms will eventually disorder the expansion of (8.5). Typically, the waves in a single triad (i.e. $M = 3$ in (8.6a)) or a single quartet ($M = 4$) are studied. Two common methods of analysis are (i) the method of multiple scales (e.g. McGoldrick, 1972) and (ii) variational techniques (e.g. Simmons, 1969). Both methods lead to a set of coupled nonlinear partial differential equations for the complex wave amplitudes. These equations are similar for all dynamical systems, differing only in real-valued “interaction coefficients” γ_m among the M -waves. For example, the equations for a single resonant triad (3-wave equations) have the form:

$$(\partial_t + \mathbf{U}_m \cdot \nabla) A_m = i\gamma_m A_{m+1}^\dagger A_{m+2}^\dagger. \quad (8.12)$$

where m is interpreted modulo 3 and \mathbf{U}_m are the respective (constant) group velocities. When the nonlinear system is not energy-conserving, the 3-wave equations of (8.12) must be modified. In the case of linear damping, (8.12) takes the form (Craik, 1986):

$$(\partial_t + \mathbf{U}_m \cdot \nabla) A_m + \delta_m A_m = i\gamma_m A_{m+1}^\dagger A_{m+2}^\dagger. \quad (8.13)$$

where δ_m are real-valued decay coefficients whose form depends on the the specific dynamical system under consideration.

CHAPTER 9

RIT AND RIPPLES

The linear dispersion relation for gravity-capillary waves on water of quiescent depth h has been known since Kelvin (e.g. see Rayleigh, 1945, and the reference cited there) and has the (dimensional) form:

$$\omega^2 = (gk + \frac{\tau}{\varrho} k^3) \tanh kh \quad (9.1)$$

where ω is the radian frequency, k is the magnitude of the wavevector, g is the gravitational force per unit mass, τ is the surface tension, h is the quiescent water depth, and ϱ is the mass density of the water. The kinematic possibility of resonance is most easily found by a graphical procedure outlined by Simmons (1969) for ripples. Figure 9.1 (after Simmons, 1969) shows the graphical solution of (8.10) using (9.1) when the wavevector of each triad is collinear. (We will generalize to the non-collinear case from this simpler case.) The figure is constructed and interpreted as follows. First, the dispersion relation of (9.1) is shown in (ω, k) space with an origin at O_1 . In the calculations for figure 9.1 we have taken $h = 4.9$ cm and $\tau = 73$ dyn/cm which corresponds to values in the experiments to be described later, and, for clarity, only one branch of (9.1) is presented. Second, a point on the dispersion curve corresponding to a "test" wave is chosen as the origin O_2 for a graph of all branches of the dispersion relation. (The test wave corresponds to the one generated by the wavemaker in the experiments to follow.) In figure 9.1 a test wave with a cyclic frequency $f = \omega/2\pi = 25$ Hz is chosen

which corresponds to one of our experiments. (Herein, we will identify the test wave as \mathbf{k}_1 and ω_1 .) The intersection points of the two dispersion curves at A , B , and C , represent the collinear, resonant triads that are possible for the particular test wave. The individual members of each triad are found easily as shown for the A -triad.

When the test-wave frequency is lowered in figure 9.1 by sliding O_2 down the dispersion curve, the triads at A and B will eventually coalesce, then disappear, leaving only the triad at C for lower test-wave frequencies. Coalescence occurs at a frequency of $2\omega_* = 19.6$ Hz for a clean water surface. The special role of this wave frequency follows from a theorem by Hasselmann (1967). According to this theorem, if only one member of a resonant triad is present initially with significant energy, then it must have the highest frequency in the triad in order to excite the other two members. Since the test waves in the experiments are input by the wavemaker, and the other triad waves must be excited from (small) background "noise," Hasselmann's theorem requires the test waves to have the highest frequencies so that only the sum triads of (8.6) are possible. Hence, the C -triad of figure 9.1 should not be excited and no triads should be available for test-wave frequencies less than 19.6 Hz.

Figure 9.1 may be generalized to waves with non-collinear wavevectors by rotation of the dispersion curves about the frequency axes. When rotation is performed (see Simmons, 1969), the A - and B -triads are found to lie on a closed curve providing a continuum of possible triads. The minimum frequency of any wave in this continuum is that of the lowest-frequency wave in the collinear A -triad, i.e. ω_3 in figure 9.1; the maximum frequency in the continuum is $(\omega_1 - \omega_3)$. The C -triad in figure 9.1 is found to lie on an open curve whose lowest frequency is $(\omega_1 + \omega_3)$. The conclusions above regarding the 19.6 Hz parametric boundary for collinear

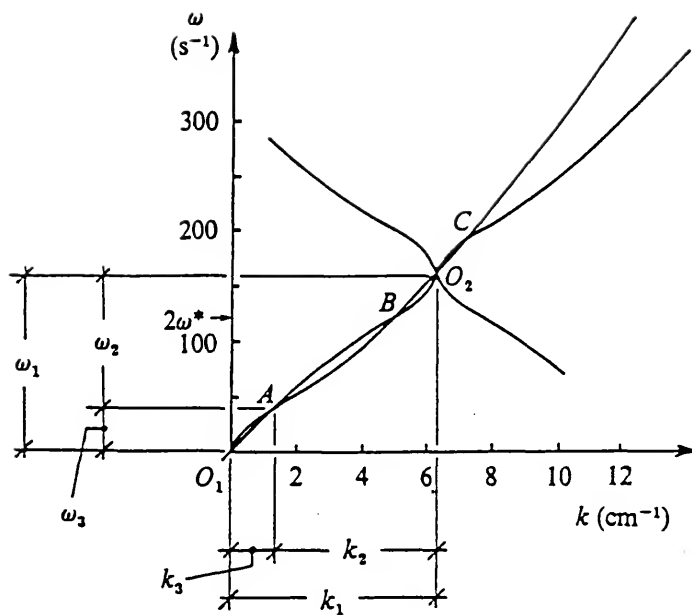


Figure 9.1 Graphical solution of the kinematic resonance conditions (after Simmons, 1969) for collinear triads of a 25 Hz test wave. (Henderson and Hammack, 1987).

triads remain applicable to the noncollinear case. Hence, triads with frequencies above $(\omega_1 + \omega_3)$ should be excluded in the experiments by Hasselmann's theorem. (However, Hasselmann's theorem does not disallow these higher-frequency waves to form sum and difference wave interactions which are non-resonant.)

The distinct frequency boundary of $2\omega_r = 19.6$ Hz for triads also has other special significance; it is the second harmonic of another important and well-known unstable wavetrain first discovered by Harrison (1909) and explained by Wilton (1915). "Wilton's ripples" have a cyclic frequency of $f_r = 9.8$ Hz on a clean surface; they are unstable to their second harmonic, which also satisfies the dispersion relation of (9.1). (This instability may be considered a degenerate resonant triad such that $\mathbf{k}_1 = 2\mathbf{k}_r$, $\mathbf{k}_2 = \mathbf{k}_3 = \mathbf{k}_r$ and $\omega_1 = 2\omega_r$, $\omega_2 = \omega_3 = \omega_r$; Hasselmann's theorem is not applicable to this special case.) In fact, a countable set of unstable ripples exists whose wavenumbers are given by $k_{rn} = \sqrt{g\tau/n\pi}$, $n = 2, 3, \dots$; each is unstable to its n th harmonic.

The triad interaction coefficients for ripples were derived by Simmons (1969), and are given by:

$$\gamma_m = -\frac{k_m}{4\omega_m} \sum_{j=1}^3 \omega_j \omega_{j+1} (1 + \mathbf{e}_j \cdot \mathbf{e}_{j+1}), \quad \mathbf{e}_j = \mathbf{k}_j / k_j, \quad (9.2)$$

where j is interpreted modulo 3. Figure 9.2(a) shows the interaction coefficient γ_2 as a function of the wave frequency f_2 for a series of test waves with frequencies $20 \text{ Hz} \leq f_1 \leq 50 \text{ Hz}$. These results are based on $h = 4.9 \text{ cm}$ (effectively the same as $h \rightarrow \infty$) and $\tau = 73 \text{ dyn/cm}$. The span in frequency of f_2 for each of the test-wave curves represents the band of admissible wave frequencies for resonant triads (e.g. the 25 Hz test wave can excite triads with member frequencies of 6-19 Hz); this band widens rapidly as the test-wave frequencies increase. Note that

γ_2 varies smoothly with the frequency of admissible triads; hence, there is no strong sensitivity to a single frequency. All three interaction coefficients are shown in figure 9.2(b) for a 25 Hz test wave. Each coefficient varies smoothly and has an extremum at a near-subharmonic frequency of 12.5 Hz. This lack of sensitivity to any specific frequency led Simmons (1969) to conjecture that all waves in the band of admissible frequencies would be excited by a test wave.

Since viscous effects are significant for ripples (primarily due to the invariable presence of surface films), it is useful to consider the 3-wave equations in the form of (8.13). In terms of the real-valued wave amplitude a_m and phase θ_m , (8.13) may be written as:

$$\partial_t a_m + \delta_m a_m + \nabla \cdot (\mathbf{U}_m a_m) = a_{m+1} a_{m+2} \gamma_m \sin \Theta. \quad (9.3a)$$

$$\partial_t \theta_m + \nabla \cdot (\mathbf{U}_m \theta_m) = (a_{m+1} \frac{a_{m+2}}{a_m}) \gamma_m \cos \Theta. \quad (9.3b)$$

where $\Theta = \theta_1 + \theta_2 + \theta_3$. In the experiments presented here, one wave is generated, say $a_1 = O(1)$, while the other triad members are small initially, say $a_2 = a_3 = O(\epsilon)$. Making use of these scalings and neglecting spatial variations, (9.3a) can be linearized to find that the temporal evolution of the small waves is approximated initially by

$$\ddot{a}_j + \dot{a}_j(\delta_2 + \delta_3) + a_j(\delta_2 \delta_3 - \gamma_2 \gamma_3 a_1^2 \sin^2 \Theta) = 0. \quad (9.4)$$

where a_1 and Θ remain at their initial values in this approximation and $j = 2, 3$. The exponential solutions of (9.4) have growth-decay rates of

$$\lambda = -\frac{1}{2}(\delta_2 + \delta_3) \pm \sqrt{(\delta_2 + \delta_3)^2 - 4(\delta_2 \delta_3 - \gamma_2 \gamma_3 a_1^2 \sin^2 \Theta)}, \quad (9.5)$$

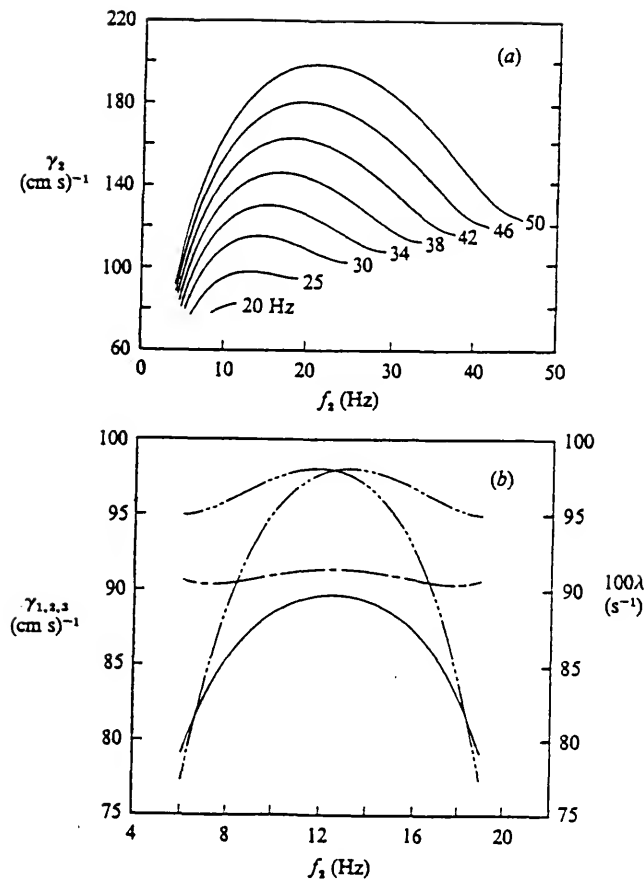


Figure 9.2 Theoretical interaction coefficients for ripple triads. (a) γ_2 vs. f_2 for a series of test waves. (b) Interaction coefficients and initial growth rate for a 25 Hz test wave γ_1 (dashed line), γ_2 (dash-dot line), γ_3 (solid line), and 100λ with $\Theta = \pi/2$, $a_1 = 0.02$ mm. (Henderson and Hammack, 1987).

for each of the background waves. In experiments using the same facilities and procedures as used herein, Henderson and Lee (1986) found that the water surfaces yielded damping characteristics for ripple wavetrains that were modelled well by assuming the surface to be "inextensible" (Lamb, 1932), so that

$$\delta_m = \frac{1}{2} k_m \sqrt{\frac{1}{2} \nu \omega_m}, \quad (9.6)$$

where ν is the kinematic viscosity of water. Using (9.2) and (9.6) it is easily shown that $\gamma_m \gg \delta_m$; hence, according to (9.5), λ is real-valued. Further, a threshold amplitude is required of the generated wave in order for the background waves to grow ($\lambda > 0$). The threshold amplitude is minimum for $\Theta = \pi/2$ and found from (9.5) to be

$$a_{l_{\min}} = \left(\frac{\delta_2 \delta_3}{\gamma_2 \gamma_3} \right)^{1/2}. \quad (9.7)$$

Figure 9.2(b) shows the initial growth rate for a 25 Hz test wave with $a_1 = 0.02$ mm and $\Theta = \pi/2$. Like the interaction coefficients, λ varies smoothly with the admissible triad frequencies, and has a maximum at the subharmonic frequency of the generated wave. Hence, even when viscous effects are considered, there does not appear to be any special sensitivity to a single triad among the continuum available.

CHAPTER 10

EXPERIMENTAL FACILITIES FOR PART 2

The experiments on ripples were performed in a laboratory facility especially designed for their study. These special facilities and procedures were required to study ripples experimentally due to their very small amplitudes and the complicated nature of surface films on a real and straining water surface. Both the procedures and facilities developed to cope with these difficulties have been described in detail by Henderson and Lee (1986) as well as H-H (1987). Hence, here we will focus on only those details not described in the cited references, which were subsequently found to be relevant to ripple experiments. (The relevance of these details may not be apparent till later.)

The ripple laboratory at the University of Florida consists of (i) a wave tank with instrument-positioning system, (ii) wave generator and associated electronics, (iii) water-supply system, (iv) wave gauge transducers with electronic-filtering system, (v) two stand-alone computer systems, (vi) and a high-speed video system with computer interface. Items (i)-(iv) were described in the references cited above. Briefly, the wave basin was constructed of glass and measures 91 cm wide, 183 cm long, and 15 cm deep. The wavemaker paddle consisted of a slender aluminum wedge which was 30.4 cm wide and was located astride the basin's long axis. The paddle was supported above the water so that the quiescent water surface intercepted the wedge near its midpoint. Aluminum sidewalls were placed inside the glass basin, adjacent to the paddle, so as to provide a test-wave channel that

was 30.5 cm wide and 91 cm long. The paddle was oscillated vertically by a Brüel and Kjaer Mini-Shaker (Type 4810) whose motion was servo-controlled with position feedback. (A one-volt amplitude signal caused the shaker to move 1 mm.) The water-supply system provided ionically pure water which was also filtered of organic material and particulate matter with sizes above 0.2 µm. Water surface elevations at fixed spatial locations, $\eta(x_0, y_0, t)$, in the tank were measured as a function of time using *in situ* capacitance gauges. The probe diameter was 1.47 mm in the experiments of H-H and those presented in Chapter 11. In the experiments of Chapters 12 and 13, the probe diameter was reduced to 1.17 mm. The latter probe had a flat response for frequencies up to 30 Hz whereas the 1.47 mm probe's response was flat till about 5 Hz, past which the signal attenuated as the frequency increased (see H-H, 1987). (Wave amplitudes as small as 0.03 mm were resolved by these gauges.) The analog gauge signals were low-pass filtered before processing by the computer systems.

In the experiments of H-H which are reviewed in Chapter 11, all of the sinusoidal command signals to the wave generator were provided by a DEC MicroPDP-11 computer system using a Data Translation analog-output system (DT2771). Wave gauge data were also digitized and analyzed using this computer system and a Data Translation analog-input system (DT2782). Data analysis was somewhat limited in resolution due the 16-bit nature of PDP-11 systems. For example, FFT's of time series from wave gauges in these experiments were obtained with a frequency resolution of 0.39 Hz within a band of 0-100 Hz. More recently, a DEC VAXstation II computer system has been installed in the laboratory, greatly enhancing the data collection and analysis capabilities. This 32-bit system contains a DEC analog-output system (AAV11-DA) and analog-input system (ADV11-DA), and was used for the experiments reported in Chapters 12 and 13. Software control

of these systems as well as data analysis and graphical output were provided by Signal Technology's Interactive Laboratory System. Using this computer system, the FFT's of wave gauge data were resolved to a frequency resolution of 0.0153 Hz over a band of 0-125 Hz.

All of the quantitative data presented previously by H-H are temporal in nature, i.e. time series at fixed spatial locations. From these data we can obtain quantitative information in the frequency domain, and test the kinematic resonance conditions of (8.10b) and (8.11b). We did not record spatial data for the triad experiments, from which a test of the resonance condition on wavevectors given by (8.10a) and (8.11a) could be made because the high-speed imaging system was not yet completely operational at the time of these experiments. Hence, it is difficult to distinguish resonant from nonresonant interactions in the experiments. (We infer resonance from dynamical aspects of wave motion such as the cycling of energy among waves.) Ultimately, this data will provide quantitative information on the wavevector distributions of surface wave patterns, and allow direct tests on the resonance conditions of (8.10a) and (8.11a).

CHAPTER 11

REVIEW OF PREVIOUS EXPERIMENTS ON RIPPLE TRIADS

H-H (1987) presented a series of experiments on ripple triads using test waves with frequencies of 9.8 Hz (Wilton's ripples), 19.6 Hz, and higher; their results and conclusions are reviewed here. (More recent interpretations of their results will be discussed in Chapter 12.) First, qualitative spatial data are presented which consist of photographs showing the wave patterns for a 25 Hz test wave as its initial amplitude is varied from below the viscous threshold of (9.3) till subharmonic cross waves form at the wavemaker paddle. Second, time series of wave gauge data are presented along with their periodograms. The analog gauge signals were low-pass filtered with a 100 Hz cut-off for record lengths of 2.56 s, and then digitized at a rate of 200 Hz. The periodograms, which show the energy density, R^2 , as a function of frequency in the band 1-100 Hz, were computed using FFT's, and have a resolution of 0.39 Hz.

11.1 The 25 Hz Wavetrain: Spatial Data

In order to show qualitatively the spatial evolution of ripple wavetrains from generation to near extinction by viscous damping, spatial views of six different 25 Hz test waves are shown in figure 11.1. (According to (9.1), $k_1 = 6.325 \text{ cm}^{-1}$ or the wavelength $L_1 = 2\pi/k_1 = 0.99 \text{ cm}$ for this wavetrain.) Each photograph presents an overhead view looking up the test channel toward the wavemaker. The vertical stroke amplitude, s of the wavemaker is varied from $ks_1 = 0.04$ in figure 11.1(a) to $ks_1 = 1.08$ in figure 11.1(f). (The parameter ks_1 is related to the strength of non-

linearity in wave generation, which is also related to the nonlinearity, $k_1 a_1$, or steepness in the progressing test wave.)

The wave pattern in figure 11.1(a) remains one-dimensional from generation to extinction by viscosity; there is no visible evidence of instabilities. As the amplitude of the test wave is increased in figure 11.1(b) through figure 11.1(e), two-dimensional instabilities appear till the wave pattern becomes quite irregular in figures 11.1(d) and 11.1(e). The irregular region is finite in extent, beginning a few wavelengths from the wavemaker paddle and declining after about twenty wavelengths. Henceforth, the wave pattern is more regular but two-dimensionality persists in the form of short-crested waves until they are extinguished by viscosity. These short-crested waves appear as a pattern of offset light and dark bands in the photographs. Finally, nonlinearity in wave generation is so strong in figure 11.1(f) that cross waves appear at the wavemaker. These cross waves have crests normal to the paddle that visibly extend for at least ten wavelengths down the channel.

The wave evolution pictured in figure 11.1 is typical of all ripple experiments, including test waves with frequencies less than 19.6 Hz. There is a region near the wavemaker where waves are essentially one-dimensional but nascent instabilities are growing. This is followed by a region of two-dimensional waves that become quite irregular as wave nonlinearity is increased. Finally, the wave pattern becomes "weakly" two-dimensional, characterized by short-crested waves, until extinguished by viscosity. The wave measurements presented hereinafter are made in the second region where resonant triads (and/or quartets, quintets, etc?) appear to be occurring.

11.2 The 25 Hz Wavetrain: Temporal Data

H-H show that the wave amplitude in the experiment of figure 11.1(a), $a_1 = 0.03 \text{ mm}$, is below the threshold value of 0.10 mm required by (9.7); hence,

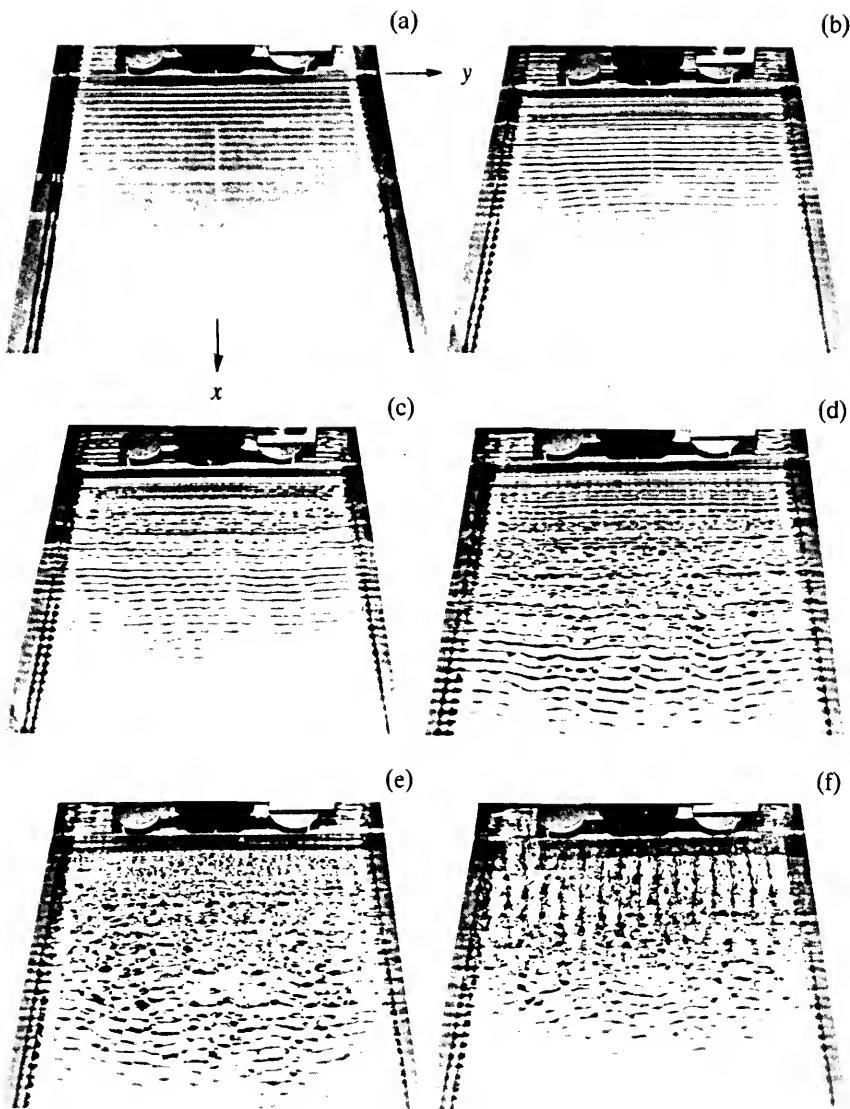


Figure 11.1 Overhead view showing spatial evolution of a 25 Hz wavetrain with increasing ks_1 -values of (a) 0.04, (b) 0.23, (c) 0.29, (d) 0.46, (e) 0.67 and (f) 1.08. (Henderson and Hammack, 1987).

no instabilities should occur, as observed. (We will also omit any data or discussion of the experiment in figure 11.1(f), since cross waves are a strongly nonlinear phenomenon.) Figure 11.2 shows portions of the wave gauge data obtained for each of the experiments pictured in figures 11.1(b) through 11.1(e). Time series of the water surface elevation relative to the quiescent water level, ηk_1 , are presented as a function of time, $t f_1$, for three different locations downstream of the wavemaker paddle. (The coordinate system is shown in figure 11.1(a).) Periodograms for the complete time series at each gauge site are also presented. These energy spectra are scaled the same for each experiment; hence, comparisons between experiments are meaningful.

The time series shown in figure 11.2 show that the wave steepness (nonlinearity) at the first gage site increases from $k_1 a_1 = 0.10$ in figure 11.2(a) to $k_1 a_1 = 0.35$ in figure 11.2(c) before decreasing to $k_1 a_1 = 0.25$ in figure 11.2(d). The decrease of wave steepness in figure 11.2(d) occurs even though the wavemaker stroke is larger there than in the other experiments. Amplitudes of the 25 Hz waves decrease during propagation down the channel in each experiment. This decrease in amplitude is substantially more (see H-H, 1987) than that predicted by the wave-damping model of (9.6). Presumably, the energy loss from the 25 Hz wave, unaccounted for by viscous damping, is the consequence of transfers through nonlinear interactions.

All of the periodograms in figure 11.2 indicate a remarkably simple result: as the 25 Hz wave propagates it excites two waves with frequencies of 10.16 Hz and 14.84 Hz. Both of these waves lie in the band of admissible triads (6-19 Hz), and clearly satisfy the kinematic condition of (8.10b). These three waves persist at all gauge sites in the latter two experiments, and their energy first decreases then *increases* during propagation in figure 11.2(d). The cycling of energy during wave

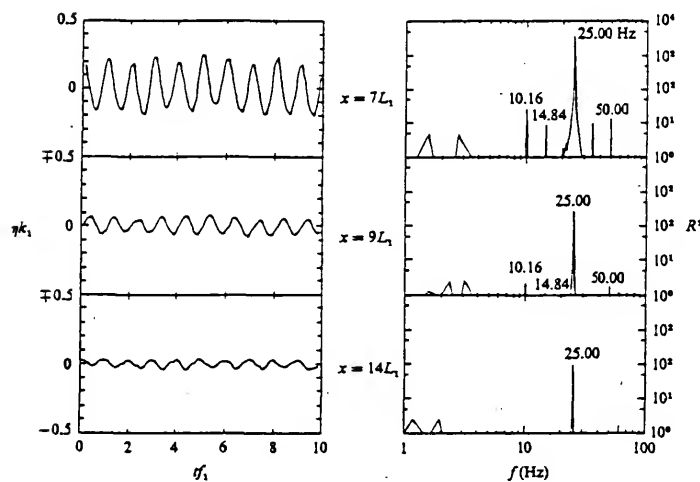
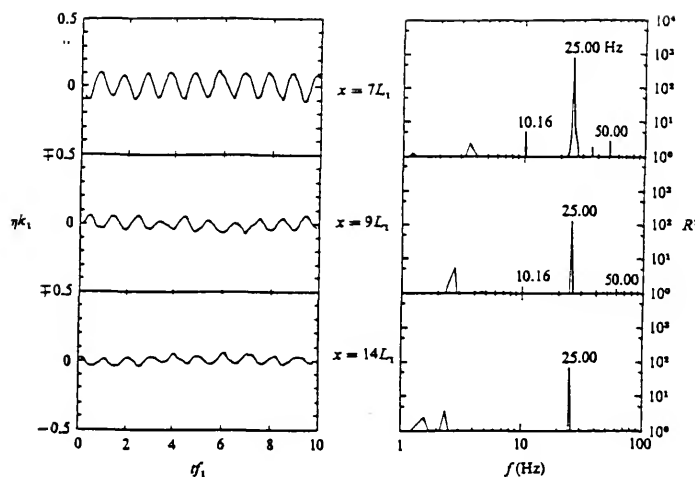


Figure 11.2 Temporal wave profiles and corresponding periodograms for the 25 Hz wavetrains of figures 11.1 (b), (c), (d) and (e), respectively. (Henderson and Hammack, 1987).

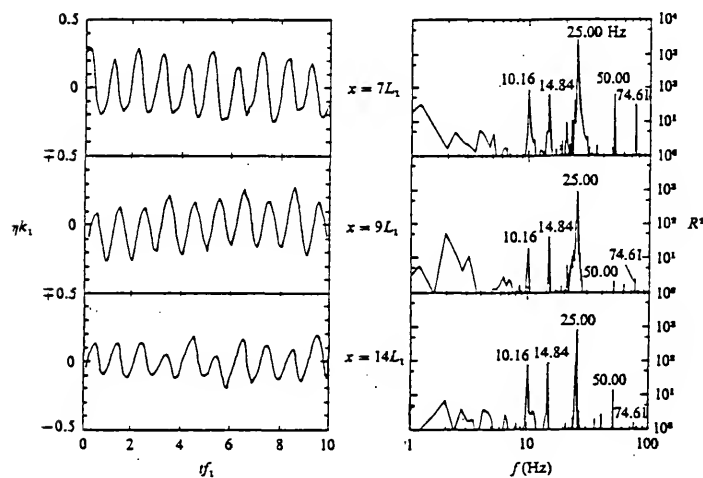
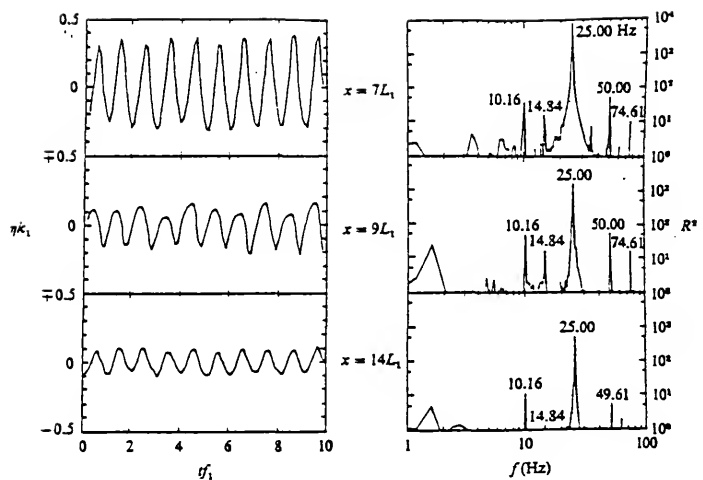


Figure 11.2--continued

propagation is not possible for nonresonant interactions, and we infer that these three waves form a resonant triad. The selection of this (25,10.16,14.84) Hz triad was found to be extremely robust by H-H, occurring repeatably for all 25 Hz test waves when their initial amplitude exceeds the viscous threshold of (9.6).

11.3 Other Wavetrains with Frequencies Exceeding 19.6 Hz.

The triad selection apparent for the 25 Hz wavetrain was also found to exist for other test-waves. This selection is illustrated in figure 11.3 where periodograms for eight other wavetrains in the frequency range of 22-46 Hz are shown. For brevity, only a single periodogram is presented for each test wave. A summary of the dominant triad excited in each experiment is presented in table 11.1, which also lists the wavevector components, $\mathbf{k} = (l, m)$, for each of the triads based on the dispersion relation of (9.1).

In the eight experiments of figure 11.3, a variety of wave triads evolve which satisfy the resonant condition of (8.10b). Both the 22 Hz test wave of figure 11.3(a) and the 27 Hz test wave of figure 11.3(b) excite waves whose frequencies correspond with those of the lowest-frequency collinear triad from the band of admissible resonant waves. (The water-surface pattern in these two experiments still appeared two-dimensional, similar to that of figure 11.1(d).) The 40 Hz test wave of figure 11.3(f) excites its subharmonic triad. (H-H report that careful observations of the wavefield near the paddle found no indication that cross waves were present in this experiment.) The other test waves exhibit no apparent pattern in the excited waves; however, the triad of evolving waves always satisfies the resonance condition of (8.10b).

In each of the eight experiments of figure 11.3 and for the test wave in the experiments of figure 11.2, a single triad of waves dominated temporal evolution. The selected triad always had frequencies in the admissible band for resonant

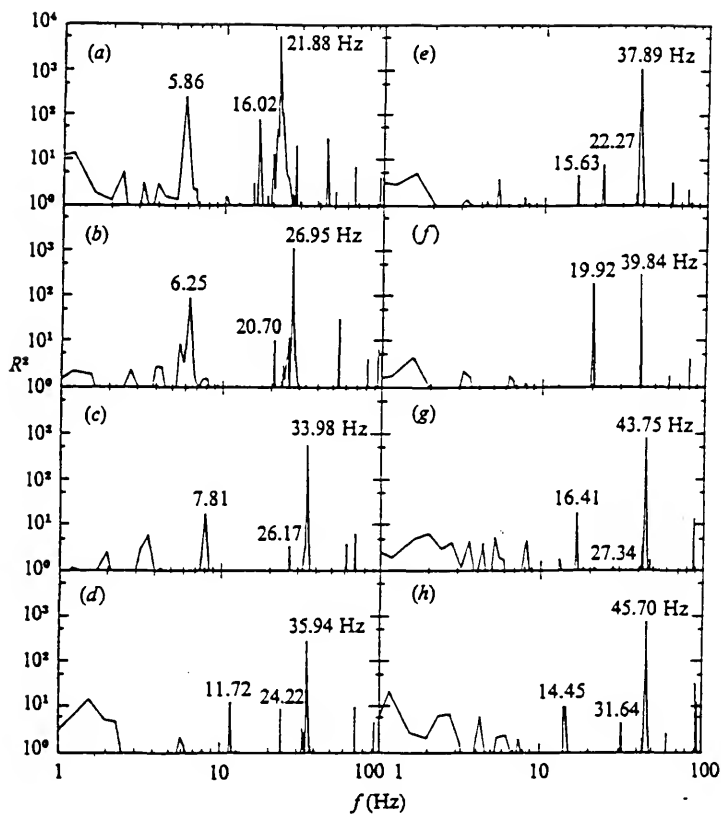


Figure 11.3 Periodograms for 8 wavetrains. Generation parameters and results are presented in Table 11.1. (Henderson and Hammack, 1987).

triads and satisfied the resonance condition of (8.10b). In contradiction of these results, H-H found that test waves with frequencies of 30 Hz and 32 Hz did not excite triads. In these experiments, energy peaks occurred only at the frequencies of the test wave and at its second and third superharmonics. This behavior persisted regardless of the initial amplitude of the test wave or the location of wave measurement. Even when no selection was apparent, the surface pattern of the wavefield remained two-dimensional.

H-H offered no explanation for the presence of a selection process in some experiments and its absence in other experiments. Certainly, based on the form of the interaction coefficients for ripples, given by (9.2) and shown in figure 9.2, RIT does not indicate that such a selection process should be present. This conclusion regarding RIT has been confirmed by Henderson (private communication, 1988) who solved the 3-wave equations of (8.12) for ripples numerically, and found no evidence of selection. Instead, all of the possible triads were excited as conjectured by Simmons (1969).

Table 11.1 Summary of experimental parameters and results for eleven experiments in the triad frequency range. Frequencies f_1 are measured from periodograms in the indicated figures; wavevectors $\mathbf{k}=(l,m)$ are calculated from the linear dispersion relation.
 (Henderson and Hammack, 1987)

Wavemaker frequency	Test wave						Excited triad waves			
	f_1 (Hz)	L_1 (Hz)	k_1 (cm $^{-1}$)	ks_1	x/L_1	y/L_1	f (Hz)	k (cm $^{-1}$)	l (cm $^{-1}$)	m (cm $^{-1}$)
22.00	21.88	1.11	5.67	0.61	14.0	0	5.86	1.24	1.24	0
							16.02	4.32	4.32	0
25.00	25.00	0.99	6.33	0.57	14.0	-4.8	10.16	2.70	2.46	1.11
							14.84	4.02	3.87	-1.11
27.00	26.95	0.94	6.71	0.59	14.0	0	6.25	1.38	1.31	0.42
							20.70	5.42	5.40	-0.42
30.00	30.08	0.86	7.31	0.58	10.0	-5.5	none	-	-	-
32.00	32.03	0.82	7.67	0.56	10.0	-5.8	none	-	-	-
34.00	33.98	0.78	8.02	0.68	8.7	-6.1	7.81	1.93	1.56	1.13
							26.17	6.56	6.46	-1.13
36.00	35.94	0.75	8.37	0.77	14.0	0	11.72	3.17	2.51	1.93
							24.22	6.17	5.86	-1.93
37.99	37.89	0.72	8.70	0.78	9.4	-6.6	15.63	4.23	3.47	2.41
							22.27	5.76	5.23	-2.41
40.00	39.84	0.70	9.03	0.74	9.9	-6.9	19.92	5.24	4.52	2.66
							19.92	5.24	4.52	-2.66
44.00	43.75	0.65	9.67	0.61	10.5	0	16.41	4.42	3.46	2.75
							27.34	6.79	6.21	-2.75
46.01	45.70	0.63	9.99	0.54	10.8	-7.6	14.45	3.92	2.87	2.67
							31.64	7.60	7.12	-2.67

CHAPTER 12

RESONANT TRIAD SELECTION

The discovery of the selection mechanism responsible for the triads in Chapter 11 resulted from the installation of the VAXstation II computer system. Once installation was complete, attempts were made to repeat earlier experiments. The results were surprising and unsettling: no selection occurred using the VAXstation II. Instead, only the test waves and their superharmonics evolved. (The surface patterns, however, remained two-dimensional like those in figure 11.1.) Immediately, the earlier experiments were repeated with the MicroPDP-11, and selection returned. Clearly, the selection mechanism was related to difference(s) in computer systems; after some effort the important difference was isolated.

The triad selection mechanism in the experiments of H-H resulted from *wave seeding* by nonlinear interaction between the test wave and an exceedingly small and short-lived 60 Hz wave. The 60 Hz water wave was the consequence of small differences in the low levels of 60 Hz electronic noise in the command signals from the computer systems to the wave generator. Electronic noise at 60 Hz is ubiquitous in nearly all electrical systems in the U.S. For example, the periodogram of any (unfiltered) electrical signal will show a distinct energy peak at 60 Hz, as can be seen in nearly all of the periodograms of Chapter 11. (Even when the wave gauge is powered but not immersed in water, its output signal still has an energy peak at 60 Hz.) The 12-bit analog-output system of the VAXstation II contained *slightly less* energy in the 60 Hz peak than that of the MicroPDP-11. It should

be emphasized that both 12-bit analog-output systems are high-quality units, and these systems were grounded according to manufacturers' specifications. All cabling between the computers and equipment used twisted wires with shielding, and was connected in the most noise-free configuration.

A comparison of the *amplitude* spectra (not energy as in previous periodograms in Part 2) for 25 Hz command signals with amplitudes of 1.2 v from each of these computer systems is presented in figure 12.1. (This is the same voltage used in the command signal of the experiment shown in figure 11.2(d). Recall that a 1 v signal causes the wavemaker paddle to displace 1 mm.) These amplitude spectra were obtained using a FFT of 2^{14} data points from a 65.532 s record of each command signal; hence, the frequency resolution in these spectra is 0.0153 Hz. (The analog command signals were first low-pass filtered at a cut-off of 100 Hz and then digitized at a rate of 250 Hz.) The amplitude at each frequency in the band of 1-100 Hz is shown in arbitrarily scaled units of db (20 db corresponds to a factor of 10 in amplitude); the scale is the same for both spectra. Both signals contain distinct 60 Hz peaks; however, that of the MicroPDP-11 is about 14 db (a factor of 5) larger than that of the VAXstation II. It turns out that the amplitude of the 60 Hz peak in the output of the VAXstation II is just below the threshold required to precipitate triad selection. If a 60 Hz command signal with an amplitude of only 0.0049 v is added to the 25 Hz command of the VAXstation II, the (10,15,25) Hz triad is selected. (A 0.0049 v signal is the smallest output our 12-bit analog-output systems can produce; hence, a square, rather than sinusoidal, wave is generated.)

Although it is difficult to pinpoint the actual sequence of events leading to triad selection from our frequency-domain data, one scenario for selecting the (10,15,25) Hz triad in the experiment of figure 11.2(d) is as follows. A quadratic

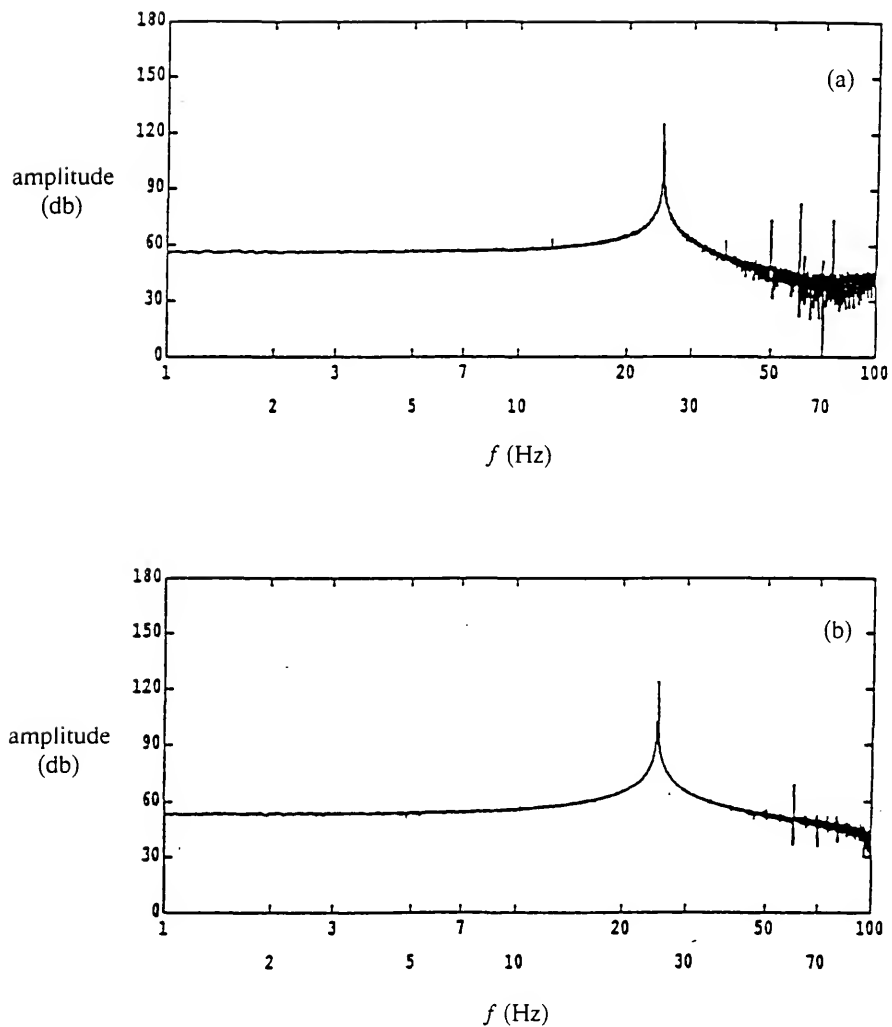


Figure 12.1 Amplitude spectra of computer generated command signals for a 25 Hz sine wave with an amplitude of 1.2 v. (a) DEC MicroPDP-11
(b) DEC VAXstation II.

interaction between (large) 25 Hz waves and (small) 60 Hz waves forms a difference wave of 35 Hz. This wave appears in the periodograms at the first and last measurement sites in figure 11.2(d), and was erroneously attributed to spurious mechanical vibrations of the paddle assembly by H-H. If this quadratic interaction is nonresonant, then the ka of the 35 Hz wave should not be larger than either parent wave, and its wavevector should be collinear with them. If the interaction is resonant, then the steepness of the 35 Hz may be larger than that of its smaller parent wave (it is larger than the 60 Hz wave at both the first and last measurement sites), but its wavevector cannot be collinear with either parent (we don't know). The 35 Hz wave then forms difference waves with the 25 Hz wave and its 50 Hz superharmonic to seed the 10 Hz and 15 Hz waves in the proper directions to precipitate the (25,15,10) Hz resonant triad.

There are some surprising aspects to the scenario described above. First, all of the events occur within seven (25 Hz) wavelengths of the wavemaker paddle. Second, the quadratic interaction between the 25 Hz and 60 Hz waves must be resonant in order to produce such a large 35 Hz wave. Yet, Hasselmann's theorem would seem to preclude interaction due to the small size (steepness) of the 60 Hz wave. Even if we assume that all the energy at the 60 Hz peak of the periodogram at $x = 7L_1$ in figure 11.2(d) belongs to a water wave, its amplitude is only 2% of that for the 25 Hz wave. In terms of wave steepness, ka , the 60 Hz wave is about 4% of that for the 25 Hz wave. If the 60 Hz wave is too large for Hasselmann's theorem to be applicable, then three resonant triads are possible in the experiment of figure 11.2(d); they are (25,15,10) Hz, (25,35,60) Hz, (25,50,75) Hz. While the latter triad also corresponds to the test wave and its superharmonics, there is evidence in the periodograms of figure 11.2(d) that other phenomena are occurring at these frequencies. For example, the 75 Hz peak is larger than the 50 Hz peak at

$x = 9L_1$, and the 50 Hz peak grows significantly by $x = 14L_1$. Third, if the (25,35,60) Hz and (25,15,10) Hz triads are resonant, then the directions of energy flux must differ from those of corresponding nonresonant waves. Hence, the 60 Hz wave input at the wavemaker must rapidly excite a 60 Hz wave in a different direction; the 35 Hz nonresonant wave (collinear with the input waves) must rapidly excite a 35 Hz wave in a different direction; and so on. (This directional spreading of amplitude can be explained by the results of Part 1.) Further, once such a proliferation of events is accepted, it is easy to conjecture that some of the energies at the (25,50,15,10) Hz peaks in figure 11.2 are due to a resonant quartet.

Confirmation of the selection process described above was established by adding a second test wave to the wavemaker command signal generated by the VAXstation II. Both the frequencies and amplitudes of these second waves were varied relative to those of the primary test waves. Before presenting an example of these data, a cautionary note should be mentioned regarding the simultaneous generation of two waves by a single wavemaker. Wavemakers are inherently nonlinear devices, though, with proper design, they are weakly nonlinear. (The B & K Mini-Shaker used in these experiments is weakly nonlinear, and strong resonances in its dynamics do not appear at the frequencies and strokes we use.) Hence, when commanded with a single sinusoidal signal, they respond by oscillating at its frequency as well as at the frequencies of its superharmonics. These superharmonic motions generate "free" water waves which satisfy the dispersion relation while the "bound" superharmonics, resulting from nonlinearity of the water-wave motion, do not. Of course, neither periodograms nor amplitude spectra from wave gauge records can distinguish between bound and free waves with the same frequency. When a weakly nonlinear wavemaker is commanded to generate two sinusoidal waves simultaneously, it also generates free water waves at the sum and difference

frequencies of the two test waves (e.g. see Flick and Guza, 1980). These waves cannot be distinguished in the data analysis either, but they can contribute to the resonant and nonresonant interactions between all the component waves in the system. This behavior should be remembered in interpreting the experiments of H-H where the second wave (60 Hz) was added inadvertently, and in the experiments to follow where second waves are added deliberately. It should also be noted that we monitor the command signal, the motion feedback of the wavemaker paddle, as well as the wave motion in these experiments. Here, only the wave gauge data and their amplitude spectra are presented.

In order to demonstrate the selection process with other than 60 Hz noise, figure 12.2 shows a sequence of periodograms computed at various downstream positions when a 25 Hz wavetrain with a command voltage of 1.2 v is superposed with a 57 Hz wavetrain whose command amplitude is 0.12 v. The amplitudes of the generated waves are proportional to the command voltage, and $k_1 a_1 = 0.20$ for the 25 Hz wavetrain at $x = 7L_1$ as in figure 11.2(d). The command signal is generated by the VAXstation II so that 60 Hz noise will no longer precipitate triads.

Just as in all previous experiments, there is a proliferation of sum and difference waves in the amplitude spectrum at the first measurement site. A rank ordering of waves by amplitude at $x = 7L_1$ is as follows: 25, 18, 32, 7, 43, 50, 14, 11, 4, 68, 5, and 22 Hz followed by 29, 36, 39, 57, 75, and 82 Hz waves which are about equal in amplitude. The 25 Hz test wave either decays slightly between gauge sites or stays the same during the 24-wavelengths of measurement. Further examination of the downstream amplitude spectra shows that the following waves exhibit resonant-like decay-growth cycle(s) of varying amounts: 4, 7, 11, 14, 18, 43, and 50 Hz. Both the 14 Hz and 11 Hz waves nearly disappear before regaining strength during propagation. The growth-decay cycle for the amplitude of the 7 Hz wave is

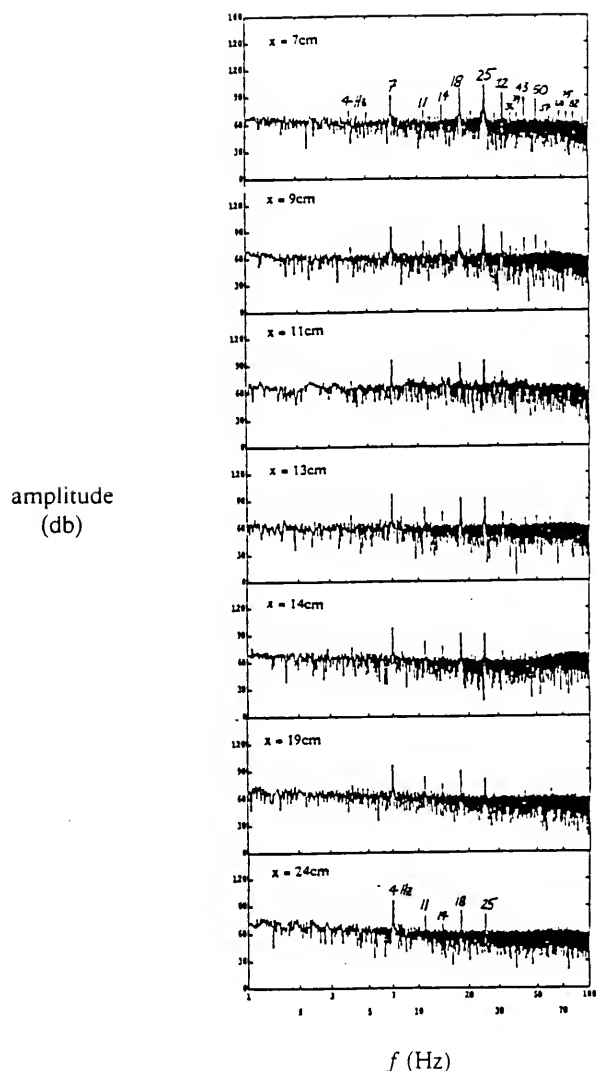


Figure 12.2 Amplitude spectral evolution for a 25 Hz wavetrain seeded with a 5 Hz wavetrain with 1/10 of its amplitude at the wavemaker.

very small. The 7 Hz wave has the largest amplitude at the last measurement site where most waves have disappeared (presumably due to viscous damping) except for two resonant triads: (25,18,7) Hz and (25,14,11) Hz. Both of these triads were selected by the small 57 Hz wave input at the wavemaker, which essentially disappeared from the wavefield by $x = 9L_1$.

In all of the experiments we have performed, we were able to seed resonant triads in a predictable manner by inputting a small wave whose frequency was higher than that of the test wave. (Of course, this frequency must lie in the band of admissible triads above the C-triad shown in Chapter 9.) We have excited triads when the amplitude of the high-frequency perturbation was only $\frac{1}{250}$ that of the test wave. (In the range of our experiments, the change in wave steepness is comparable to the change in amplitude since wavevector magnitudes change little.) Even though some of the details of the selection process are obscured by our lack of wavevector data, it is clear that exceedingly small, high-frequency perturbations with distinct frequencies can select the resonant triad(s) which ultimately dominate wave evolution.

CHAPTER 13

EVOLUTION OF A RIPPLE WAVETRAIN IN THE PRESENCE OF RANDOM WAVES

When background noise was minimum in experiments and no perturbations with distinct frequencies were added intentionally, the test waves did not excite any dominant triads. (Still, the surface patterns remained two-dimensional for all sensible test-wave amplitudes.) Instead, no significant nonlinear interactions appeared (other than superharmonics) during wavetrain evolution. In this section we present data for experiments in which the background energy at all frequencies was increased intentionally. This was accomplished by programming the wavemaker to generate a test wave and psuedo-random waves simultaneously. (Of course, the wavevectors for all the random waves and the test wave were collinear at the wavemaker.) The amplitudes of the random waves were fairly uniform over all frequencies, i.e. the background waves corresponded to "white" noise. The signal-to-noise ratio (S/N) based on root-mean-square measures of signal amplitudes, was decreased (holding the test-wave signal constant) until nonlinear interactions between the test wave and background waves were observed.

An experiment was conducted in the following manner. First, 16 time series of wave gauge data were obtained for the natural background noise in the tank when the wavemaker was powered but not moving; each time series was 65.532 sec in duration. These time series were digitized at a rate of 250 Hz and amplitude spectra were computed using 2^{14} data points for each spectrum. (All analog gauge

signals were low-pass filtered with a cutoff frequency of 100 Hz prior to digitizing.) These 16 amplitude spectra were then averaged at each frequency to obtain an average amplitude spectrum for the natural background noise, $\{\mathfrak{B}\}$, in the tank. Then 16 experiments were conducted using 16 different white-noise command signals to the wavemaker. These 16 time histories of wave gauge data were analyzed as before to find an average amplitude spectrum for the random waves in the presence of the tank's natural background noise, $\{\mathfrak{R}+\mathfrak{B}\}$. Then 16 experiments were performed with only the test wave to yield an average amplitude spectrum for the test wave with the tank's background noise, $\{\mathcal{T}+\mathfrak{B}\}$. The test-wave signal was then added to the 16 command signals of white noise and 16 more experiments were conducted and analyzed to find an average amplitude spectrum for the test wave with random waves and the tank's background noise, $\{\mathcal{T}+\mathfrak{R}+\mathfrak{B}\}$. These four average spectra can then be combined to find the signature of the random waves alone, i.e. $\{\mathfrak{N}\} = \{\mathfrak{R}+\mathfrak{B}\} - \{\mathfrak{B}\}$, the test wave alone, i.e. $\{\mathcal{T}\} = \{\mathcal{T}+\mathfrak{B}\} - \{\mathfrak{B}\}$, as well as to display effects resulting from nonlinear interactions. The latter result was found by computing

$$\{\mathfrak{N}\} = \{\mathcal{T}+\mathfrak{R}+\mathfrak{B}\} - \{\mathcal{T}\} - \{\mathfrak{R}\} - \{\mathfrak{B}\}: \quad (13.1)$$

hence, $\{\mathfrak{N}\}$ is null if there are no significant nonlinear interactions. This procedure assumes that the natural background noise in the tank is sufficiently small so as not to interact significantly with either the random wave or the test waves. These assumptions are consistent with our experimental observations. The entire series of experiments and calculations outlined above were performed at three gauge sites downstream of the wavemaker. (In addition to wave gauge data, we also analyzed the time series for the command signals and the actual paddle motion during each experiment. All measurements resulted in the collection and analysis of 50-mega-bytes of data at each gauge site!)

An example of our experimental results is shown in figures 13.1 and 13.2 for a 25 Hz test wave and random waves with S/N = 20. (This test wave is identical to that in figure 11.2(c) where its initial nonlinearity was measured to be about $k_1 a_1 = 0.35$.) Figure 13.1(a) shows the average amplitude spectrum for the natural background noise $\{\mathfrak{B}\}$ in the tank at $x = 7$ cm, which is equal to seven test wavelengths for the 25 Hz wavetrain. (This result is typical of all background noise measurements.) The amplitudes of background noise are smoothly distributed over the frequency band 1-100 Hz, and decrease uniformly with increasing frequency. (The distinct peak at 60 Hz is due to electronic noise.) Figure 13.1(b) shows the average amplitude spectrum at $x = 7$ cm for the random wavefield $\{\mathfrak{R}\}$. Amplitudes are nearly zero at frequencies below 2 Hz after which the amplitudes increase slowly reaching a maximum level of about 20 db around 80 Hz. Even though the spectrum of the random waves is not completely "white," it is indeed broad-banded.

The main results of this experiment are presented in figure 13.2. Unfortunately, the data used to calculate the average amplitude spectrum of the test wave with background noise, $\{\mathcal{T}+\mathfrak{B}\}$, were not recorded separately. Hence, figure 13.2 shows

$$\{\mathcal{N}\} + \{\mathcal{T}\} = \{\mathcal{T} + \mathfrak{R} + \mathfrak{B}\} - \{\mathfrak{R}\} - \{\mathfrak{B}\}$$

rather than $\{\mathcal{N}\}$ alone, i.e. the test wave signal is still present among the measure of nonlinear interactions. (Later measurements of the test wave evolution show that only the primary wave and its first two superharmonics were present.) Clearly, significant nonlinear interactions are occurring in figure 13.2. The random waves in the frequency band of about 6-19 Hz have interacted (grown) most significantly: this is the band of admissible resonant triads for a 25 Hz wave as discussed in

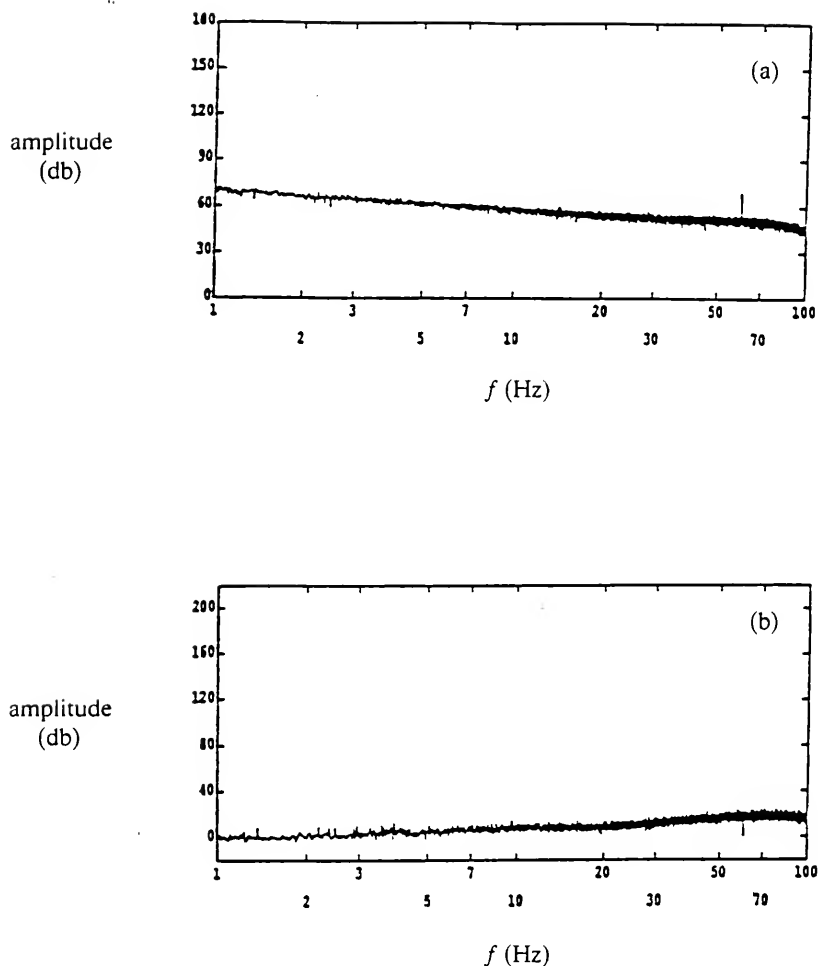


Figure 13.1 Average amplitude spectra at $x = 7$ cm for (a) natural background noise in the wave tank and (b) random waves generated by the wavemaker.

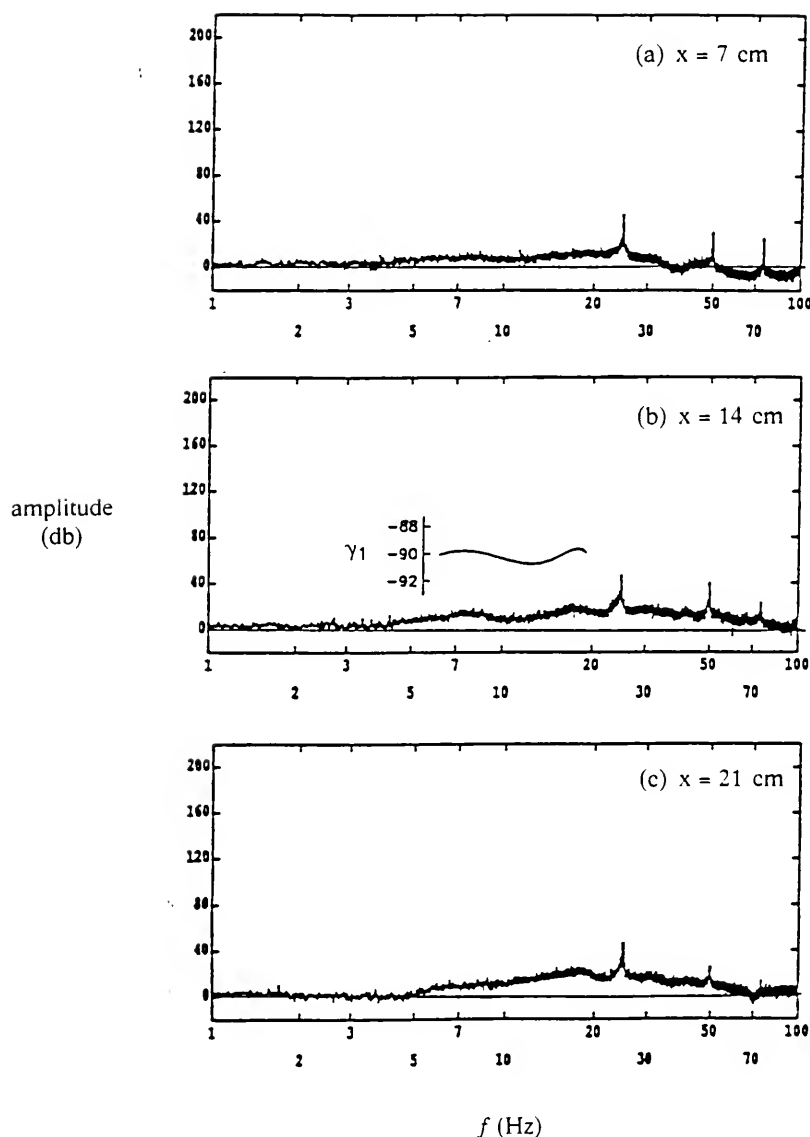


Figure 13.2 Average amplitude spectra showing the transfer of energy by non-linear interactions between a 25 Hz test wave and random waves (white noise) generated with a $S/N = 10$.

Chapter 9. The amplitudes of the waves in this resonant band continue to grow in the downstream direction, in spite of viscous effects. In fact, the band of growing triads appears to excite superharmonic bands behind the superharmonics of the test wave. Furthermore, the distribution of amplitudes in the triad band of 6-19 Hz is bimodal at all three gauge sites with maxima occurring at frequencies of about 7 Hz and 17 Hz and a minimum at about 12 Hz. This measured amplitude distribution in the resonant triad band is remarkably similar in extrema frequencies to those of the interaction coefficient γ_1 of (9.2), which is also shown in figure 9.2(b). In order to emphasize this similarity we have superposed a plot of γ_1 onto the amplitude spectrum of $\{N\} + \{T\}$ in figure 13.2(b). γ_1 can be interpreted as a measure of the amount of amplitude (energy) exchanged from the test wave to other members of admissible triads. Hence, the similarity is not fortuitous; it should be expected. It is clear in figure 13.2 that resonant interactions with background noise of sufficient size allow a ripple wavetrain to distribute its energy to a wide band of lower-frequency waves.

CHAPTER 14

SUMMARY AND CONCLUSIONS OF PART 2

The simple-periodic one-dimensional wavetrain is the cornerstone of wave mechanics, having served since Airy (1845) and Stokes (1847) as the fundamental building block for studying the effects of weak nonlinearity. Herein, we have used these wavetrains in the theoretical and experimental study of the dynamics of gravity-capillary waves. Theoretical considerations were based on RIT (resonant interaction theory) while in the experiments we generated ripple wavetrains mechanically in a wide channel of uniform breadth and depth. The experiments used test waves with frequencies greater than 19.6 Hz, where RIT indicated that triad resonances were the first to occur, and a continuum of resonant triads was available. Rather extreme precautions were taken in the experiments to maintain the purity of the water surface, to keep the natural background noise in the laboratory at a minimum level, and to generate the wavetrains as cleanly as possible. In spite of these precautions, the experimental wavetrains rapidly became unstable; retaining their one-dimensional surface pattern for a distance of only a few wavelengths before disintegrating into two-dimensional patterns. This spatial behavior persisted for all wavetrains with sensible amplitudes, i.e. $ka > 0.1$. Temporal data in the two-dimensional region showed that resonant triads did occur, in agreement with RIT. However, we also found that one or more resonant triads could be excited by a high-frequency seed wave of exceedingly small amplitude (steepness). When specific triads were selected by a seed wave, they dominated evolution of the

wavefield. When no seed waves were present and the background noise in an experiment was increased intentionally by generating a broad spectrum of random waves, a test wave excited the entire continuum of admissible triads in a manner consistent with RIT for a single triad. These results clearly showed that a single ripple wavetrain can distribute its energy to a wide band of lower frequency waves through resonant interactions.

The complexity of ripple dynamics we have observed in the pristine and controlled environment of a laboratory is likely to be a small subset of the complexity which occurs on the ocean's surface where straining by larger gravity waves and surface films are ubiquitous.

CHAPTER 15

GENERAL SUMMARY AND CONCLUSIONS

Wavetrains with frequencies greater than 9.8 Hz are spatially unstable and spread their energy according to the sNLS equation with local energy maxima appearing in the region of the most unstable sidebands and spreading throughout the admissible region of instability as predicted by linear stability theory. Wilton's ripples, as expected, is shown to be unstable to its second harmonic (well-known second harmonic resonance), and shown to spread its energy significantly in wavenumber space. An experiment for an 8 Hz wavetrain is presented in which the first and second superharmonics appear, and then the second superharmonic is shown to resonate with the primary wave (third harmonic resonance), and once it attains significant free wave energy, it spreads its energy according to the sNLS equation.

In the second part of the study, wavetrains are studied theoretically, using resonant interaction theory, and experimentally, by the mechanical generation of ripple wavetrains in a channel of uniform depth (essentially deep water for these high frequency waves) and breadth. The frequencies of these wavetrains were all greater than 19.6 Hz. Theory predicts that triad resonances are the first to occur for these frequencies. It was found that exceedingly small seed waves can cause triads to occur. Also, the selection process unexplained by H-H has now been attributed to the presence of 60 Hz electronic noise which acted as a high-frequency seed wave. When specific triads were selected by a seed wave, they domi-

nated the temporal evolution of the wavefield. The fact that a very small seed wave, whose difference waves with the primary wave seed the low-frequency waves in the admissible triad regime, and thus trigger triad generation, was totally unexpected. It was also demonstrated that a broad background of white noise could be introduced, and when the level of this background noise was increased to a particular signal-to-noise ratio, a continuum of admissible triads was excited in a manner consistent with resonant interaction theory's prediction for a single triad.

In the future, experiments must be performed in which triads are seeded and spatial data is obtained. Only then will the relative ordering of spatial disintegration and triad generation be disentangled. Can we produce triads with essentially no energy spreading present? In fact, it may be the energy spreading due to the sNLS equation which produces wave oriented in the proper direction to allow the non-collinear triads to occur.

REFERENCES

ABLOWITZ, M. J. & SEGUR, H. 1979 On the evolution of packets of water waves. *J. Fluid Mech.* **92**, 691-715.

AIRY, G. B. 1845 Tides and Waves. *Encyclopaedia Metropolitana* **5**, 241-396.

BANNERJEE, P. P. & KORPEL, A. 1982 Subharmonic generation by resonant three-wave interaction of deep-water capillary waves. *Phys. Fluids* **25**, 1938-1943.

BENJAMIN, T. B. & FEIR, J. E. 1967 The disintegration of wavetrains on deep water. Part 1. Theory. *J. Fluid Mech.* **27**, 417-430.

BENNEY, D. J. 1962 Nonlinear gravity wave interactions. *J. Fluid Mech.* **14**, 577-584.

BENNEY, D. J. & NEWELL, A. C. 1967 The propagation of nonlinear wave envelopes. *J. Math. and Phys.* **46**, 133-139.

BENNEY, D. J. & ROSKES, G. 1969 Wave instabilities. *Stud. Appl. Math.* **48**, 377-385.

CHEN, B. & SAFFMAN, P. G. 1985 Three-dimensional stability and bifurcation of capillary and gravity waves on deep water. *Stud. Appl. Math.* **72**, 125-147.

CRAIK, A. D. D. 1986 Exact solutions of non-conservative equations for three-wave and second-harmonic resonance. *Proc. R. Soc. Lond.*, **A406**, 1-12.

DAVEY, A. & STEWARTSON, K. 1974 On three-dimensional packets of surface waves. *Proc. Roy. Soc. Lond.* **A338**, 101-110.

DJORDJEVIC, V. D. & REDEKOPP, L. G. 1977 On two-dimensional packets of capillary gravity waves. *J. Fluid Mech.*, **79**, 703-714.

FARADAY, M. 1883 On the Crispations of Fluid resting upon a Vibrating Support. *Phil. Mag.* **xvi**, 50.

FLICK, R. E. & GUZA, R. T. 1980 Paddle generated waves in laboratory channels. *J. Waterway, Port, Coastal, Ocean Eng. ASCE*, **106**, 79-97.

HAMMACK, J. L., PERLIN, M., & HENDERSON, D. M. (to appear) 1989 Lecture presented at the International School of Physics "Enrico Fermi," Course CIX.

HAMMACK, J. L. & SEGUR, H. 1974 The Korteweg-de Vries equation and water waves. Part 2. Comparison with experiments. *J. Fluid Mech.* **65**, 289-314.

HAMMACK, J. L. & SEGUR, H. 1978 The Korteweg-de Vries equation and water waves. Part 3. Oscillatory waves. *J. Fluid Mech.* **84**, 337-358.

HARRISON, W. J. 1909 The influence of viscosity and capillarity on waves of finite amplitude. *Proc. London Math. Soc.* (2) **7**, 107-121.

HASIMOTO, H. & ONO, H. 1972 Nonlinear modulation of gravity waves. *J. Phys. Soc. Japan* **33**, 805-811.

HASSELMANN, K. 1967 A criterion for nonlinear wave stability. *J. Fluid Mech.* **30**, 737-739.

HENDERSON, D. M. 1986 Resonant Interactions Among Ripples. Master of Science Thesis, Engr. Sci. Dept., Univ. of Florida.

HENDERSON, D. M. & HAMMACK, J. L. 1987 Experiments on ripple instabilities. Part 1. Resonant triads. *J. Fluid Mech.* **184**, 15-41.

HENDERSON, D. M. & LEE, R. C. 1986 Laboratory generation and propagation of ripples. *Phys Fluids* **29** (3), 619-624.

KELVIN, LORD 1871 Hydrokinetic Solutions and Observations. *Phil. Mag.* **xlii** (4), 375.

LAKE, B. M., YUEN, H. C., RUNGALDIER, H. & FERGUSON, W. E. 1977 Nonlinear deep-water waves: theory and experiment. Part 2. Evolution of a continuous wavetrain. *J. Fluid Mech.* **83**, 49-74.

LAMB, H. 1932 *Hydrodynamics*. New York, N.Y., Dover, 631-632.

LIGHTHILL, M. J. 1965 Contributions to the theory of waves in nonlinear dispersive systems. *J. Inst. Math. Applies.* **1**, 269-306.

LONGUET-HIGGINS, M. S. 1976 On the nonlinear transfer of energy in the peak of a gravity-wave spectrum: a simplified model. *Proc. R. Soc. Lond. A.* **347**, 311-328.

MA, Y.-C., 1979 The perturbed plane-wave solutions of the cubic Schroedinger Equation. *Studies Appl. Math.* **60**, 43-58.

MA, Y.-C., 1982 Weakly nonlinear steady gravity-capillary waves. *Phys. Fluids* **25**(6), 945-948.

McGOLDRICK, L. F. 1965 Resonant interactions among gravity-capillary waves. *J. Fluid Mech.* **21**, 305-331.

McGOLDRICK, L. G. 1970 An experiment on second-order capillary-gravity resonant wave interactions. *J. Fluid Mech.* **40**, 251-271.

McGOLDRICK, L. F. 1972 On the rippling of small waves: a harmonic nonlinear nearly resonant interaction. *J. Fluid Mech.* **52**, 725-751.

PEREGRINE, D. H. 1983 Water waves, nonlinear Schroedinger equations and their solutions. *J. Austral. Math Soc. Ser. B* **25**, 16-43.

PHILLIPS, O. M. 1960 On the dynamics of unsteady gravity waves of finite amplitude. Part 1. The elementary interactions. *J. Fluid Mech.* **9**, 193-217.

PHILLIPS, O. M. 1977 *The Dynamics of the Upper Ocean*. London, England. Cambridge University Press.

RAYLEIGH, J. W. S. 1890 On the tension of water surfaces, clean and contaminated. *Phil. Mag.* **xxx**, 386.

RAYLEIGH, J. W. S. 1945 *The Theory of Sound*. New York, N.Y., Dover, 344.

SEGUR, H. 1984 Toward a New Kinetic Theory for Resonant Triads. *Contemporary Math.* **28**, 281-313.

SIMMONS, W. F. 1969 A variational method for weak resonant wave interactions. *Proc. R. Soc. Lond.*, A**309**, 551-575.

SOBEY, R. J. & COLMAN, E. J. 1982 Natural Wave Trains and Scattering Transform. *J. Waterway, Port, Coastal and Ocean Div., ASCE*, **108**, No. WW3, 272-290.

STOKES, G. G. 1847 On the theory of oscillatory waves. *Trans. Camb. Phil. Soc.* **8**, 441-455.

WHITHAM, G. B. 1967 Nonlinear dispersion of water waves. *J. Fluid Mech.* **27**, 399-412.

WILTON, J. R. 1915 On ripples. *Phil. Mag.* (6) **29**, 688-700.

YUEN, H. C. & LAKE, B. M. 1975 Nonlinear deep water waves: theory and experiment. *Phys. Fluids* **18**, 956-960.

ZAKHAROV, V. E. 1968 Stability of periodic waves of finite amplitude on the surface of a deep fluid. *J. Appl. Mech. Tech. Phys.* **2**, 190-194.

ZAKHAROV, V. E. AND SHABAT, A.B. 1972 Exact theory of two-dimensional self-focussing and one-dimensional self-modulation of waves in nonlinear media. *Soviet Phys. JETP* **34**, 62-69.

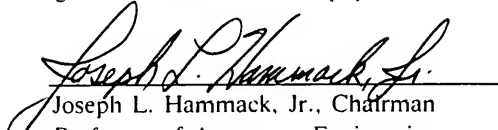
ZHANG, J. & MELVILLE, W. K. 1986 On the stability of weakly-nonlinear gravity-capillary waves. *Wave Motion* **8**, 439-454.

ZHANG, J. & MELVILLE, W. K. 1987 Three-dimensional instabilities of nonlinear gravity-capillary waves. *J. Fluid Mech.* **174**, 187-208.

BIOGRAPHICAL SKETCH

Marc Perlin was born to Milton and Lorraine Perlin on May 29, 1951 in Lakewood, New Jersey. After graduating Lakewood High School in June, 1969, he attended Drexel University, graduating with a B. S. in civil engineering with honors in June 1974. At this time he began working as a field engineer in private industry. After only 1.5 years in industry, he returned to the University of Delaware, completed his masters' degree work in October 1977 and thus received his degree in June 1978. For a year he worked at the Coastal Engineering Research Center which he then left to join a large consulting engineering firm where he was able to travel extensively. After tiring of travel, he joined a small, high tech consulting firm, where he remained for three years. At this point, Marc accepted the position as Director of the University of Florida's Coastal and Oceanographic Engineering Laboratory with the idea that he could pursue his PhD. concurrently. After four years of directing the laboratory and attending graduate school, he decided, once he had passed the qualifying exam in April 1987, to resign his position and dedicate his time exclusively toward his doctoral research.

I certify that I have read this study and that in my opinion it conforms to acceptable standards of scholarly presentation and is fully adequate, in scope and quality, as a dissertation for the degree of Doctor of Philosophy.


Joseph L. Hammack, Jr.
Professor of Aerospace Engineering,
Mechanics, and Engineering Science

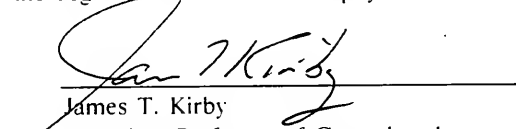
I certify that I have read this study and that in my opinion it conforms to acceptable standards of scholarly presentation and is fully adequate, in scope and quality, as a dissertation for the degree of Doctor of Philosophy.


Robert G. Dean
Graduate Research Professor of Coastal
and Oceanographic Engineering

I certify that I have read this study and that in my opinion it conforms to acceptable standards of scholarly presentation and is fully adequate, in scope and quality, as a dissertation for the degree of Doctor of Philosophy.


Ulrich H. Kurzweg
Professor of Aerospace Engineering,
Mechanics, and Engineering Science

I certify that I have read this study and that in my opinion it conforms to acceptable standards of scholarly presentation and is fully adequate, in scope and quality, as a dissertation for the degree of Doctor of Philosophy.


James T. Kirby
Associate Professor of Coastal and
Oceanographic Engineering

This dissertation was submitted to the Graduate Faculty of the College of Engineering and to the Graduate School and was accepted as partial fulfillment of the requirements for the degree of Doctor of Philosophy.

August, 1989



Dean, College of Engineering

Dean, Graduate School

UNIVERSITY OF FLORIDA



3 1262 08553 6463